



TECHNISCHE  
UNIVERSITÄT  
WIEN



DISSERTATION

# Spin Physics and Cavity-QED with Nitrogen Vacancy Centres in Diamond

ausgeführt zum Zwecke der Erlangung des akademischen Grades eines

**Doktors der technischen Wissenschaften**

unter der Leitung von

**Univ. Ass. Dr. Johannes Majer**

E141 Atominstitut

und

**Univ. Prof. Dipl.-Ing. Dr. techn. Hannes-Jörg Schmiedmayer**

E141 Atominstitut

eingereicht an der

Technischen Universität Wien

Fakultät für Physik

von

**Dipl.-Ing. Thomas Astner**

Matrikelnummer: 0828052

Schäffergasse 21/8

1040 Wien

Wien, am 27.05.2019

.....  
Thomas Astner

Gutachter:

.....  
Univ. Ass. Dr. J. Majer

.....  
Prof. Dr. F. Jelezko

.....  
Prof. Dr. J. Meijer



*“Never forget what you are, for surely the world will not. Make it your strength. Then it can never be your weakness. Armour yourself in it, and it will never be used to hurt you.”*

GEORGE R. R. MARTIN, A GAME OF THRONES



# Abstract

Over the last decade the negatively charged nitrogen vacancy (NV) centre in diamond has attracted significant attention for a vast variety of applications ranging from high precision sensing to quantum information tasks. Properties like long phase coherence and spin life-times together with optical addressability have put this solid state spin in the focus of many different types of research. To further exploit all its features it is necessary to understand fundamental physical properties like the interaction of the spin degree of freedom with the diamond lattice phonons.

In the solid state environment, the most fundamental process by which an excited spin transfers energy to its surrounding is governed by longitudinal relaxation processes. These processes are usually driven by spin-phonon interaction. This work presents an experimental study of phonon induced longitudinal spin relaxation in the low temperature limit, where quantum effects become relevant. The experiment is based on cavity quantum electrodynamics in the strong dispersive limit. A quantum non-demolition detection scheme is used to read out the inversion state of up to  $1 \times 10^{16}$  NV spins.

Remarkably, the main experimental findings show that the low phononic density of states at the NV transition energy enables a non-equilibrium inversion to survive over macroscopic time-scales of up to 8h. Additionally, with an *ab initio* calculation based on density functional theory it is possible to identify a single phonon process as the main mechanism of spin lattice relaxation in this type of system in the low temperature limit.

In a second experiment the possibility to use the NV centre as a building block for quantum information tasks is demonstrated. There, two spatially separated ensembles are coupled to a common bosonic resonator mode. This presents a step towards entanglement of macroscopic spin ensembles and the study of unusual dynamics like negative temperature relaxation. Again, the dispersive regime of cavity QED is utilized and a transverse coupling of the spin ensembles via virtual photons in the resonator is shown. Although it is a fundamental necessity to have coherent coupling between the ensembles, it still remains challenging to experimentally show entanglement in such a system of two distinct spin domains.



# Zusammenfassung

In den letzten Jahren konnte das negativ geladene Stickstoff-Fehlstellen-Zentrum (NV) in Diamant aufgrund seiner vielzähligen Anwendungsmöglichkeiten große Aufmerksamkeit auf sich ziehen. So zum Beispiel reichen die Möglichkeiten von hoch präzisen Sensoren bis hin zu Quanten Informationsprotokollen. Eigenschaften wie lange Spin-Phasen Kohärenz und Lebenszeit stellen das NV Zentrum auch in den Fokus aktueller Forschung. Um all diese Eigenschaften noch besser nutzen zu können, ist es wichtig die zugrundeliegenden physikalischen Phänomene dieses Systems zu verstehen. Ein wichtiger Punkt dabei ist die Wechselwirkung des Spin Freiheitsgrades mit den Phononen des Diamantgitters.

In einem Festkörpers sind longitudinale Relaxationsprozesse bei denen der Spin Energie an die Phononen abgibt dominant. Diese Arbeit beschäftigt sich mit der experimentellen Bestimmung der longitudinalen Spin-Gitter Relaxationszeit im Limit von niedrigen Temperaturen. Das Experiment basiert auf Cavity-Quantenelektrodynamik im starken dispersiven Limit. Dort ist es möglich den Spin-Inversionszustand von bis zu  $1 \times 10^{16}$  NV Spins zu bestimmen.

Bemerkenswert, die niedrige phononische Zustandsdichte erlaubt der Spininversion über lange Zeitskalen von bis zu 8 h zu bestehen. Dieses experimentelle Ergebnis wird zusätzlich durch eine *ab initio* Simulation basierend auf der Dichtefunktionaltheorie (DFT) gestützt. Es zeigt sich, dass im Niedrigtemperaturlimit ein Einzel-Phononen Prozess den dominanten Relaxationsmechanismus darstellt.

In einem weiteren Experiment im dispersiven Limit wird die Eignung von NV Zentren für Quanten Informationsaufgaben gezeigt. Zwei räumlich getrennte Spin Ensembles werden an eine gemeinsame bosonische Resonanzmode gekoppelt. Diese kohärente Kopplung ist ein erster Schritt in Richtung Verschränkung makroskopischer Ensembles und eröffnet Möglichkeiten ungewöhnliche Dynamik wie zum Beispiel die Relaxation zu negativen Temperaturen zu studieren. Die Kopplung der entfernten Ensembles entsteht durch virtuelle Photonen in der Resonanzmode. Kohärente Kopplung ist eine notwendige jedoch nicht hinreichende Bedingung für Quantenverschränkung - ein Phänomen welches experimenteller Nachweis immer noch eine große experimentelle Herausforderung darstellt.





# Contents

<b>Abstract</b>	<b>ii</b>
<b>Zusammenfassung</b>	<b>iii</b>
<b>List of Publications</b>	<b>vii</b>
<b>Introduction</b>	<b>viii</b>
<b>I. Theoretical Concepts</b>	<b>1</b>
<b>1. The Nitrogen Vacancy Colour Centre in Diamond</b>	<b>2</b>
1.1. Ground State Level Structure . . . . .	3
1.2. Statistical Mechanics of a NV Ensemble . . . . .	4
1.2.1. Internal Energy and Heat Capacity . . . . .	6
1.3. Spin Lattice Relaxation . . . . .	7
1.3.1. Single Phonon Processes . . . . .	9
1.3.2. Single Phonon Relaxation Dynamics . . . . .	13
<b>2. Light Matter Interaction</b>	<b>18</b>
2.1. Jaynes-Cummings Model . . . . .	19
2.1.1. Generalized 3-level Jaynes-Cummings Model . . . . .	22
2.2. Tavis-Cummings Model . . . . .	25
<b>3. Confined Electromagnetic Fields - Cavities and Resonators</b>	<b>28</b>
3.1. Cavity Input-Output Formalism . . . . .	29
3.2. LC Oscillator - Classical to Quantum . . . . .	31
<b>II. Experimental Implementation and Techniques</b>	<b>34</b>
<b>4. Microwave Resonators</b>	<b>35</b>
4.1. Coplanar Waveguide Resonator . . . . .	35
4.2. 3D Lumped Element Resonator . . . . .	40

<b>5. NV Spins in Diamond - Samples</b>	<b>47</b>
<b>6. Hybrid Quantum System</b>	<b>49</b>
6.1. Experimental Set-up . . . . .	51
6.1.1. Spectroscopy Set-up . . . . .	54
<b>III. Scientific Results</b>	<b>56</b>
<b>7. Strong Coupling: 3D Lumped Element Mode and Spin Ensemble</b>	<b>57</b>
<b>8. Spin Lifetime of a Nitrogen Vacancy Centre</b>	<b>60</b>
8.1. The Lifetime Problem . . . . .	60
8.2. Experimental Verification . . . . .	61
8.3. Temperature Dependence of the Relaxation Rate . . . . .	69
8.4. <i>Ab initio</i> Calculation of $\Gamma_0$ . . . . .	73
8.5. Conclusion and Outlook . . . . .	75
<b>9. Coupling of Remote Spin Ensembles</b>	<b>77</b>
9.1. Two Ensembles in a Cavity . . . . .	78
9.2. Two Ensembles Coherently Interacting with a Cavity Mode . . . . .	81
9.2.1. System Hamiltonian . . . . .	81
9.2.2. Transmission Spectroscopy . . . . .	83
9.3. Transverse Coupling of Two Ensembles . . . . .	88
9.3.1. System Hamiltonian . . . . .	88
9.3.2. Dispersive Spectroscopy . . . . .	89
9.4. Conclusion and Outlook . . . . .	93
<b>Outlook and Prospects</b>	<b>95</b>
<b>Appendix</b>	<b>99</b>
A. Single Phonon Relaxation Dynamics for Small Magnetic Fields . . . . .	99
B. Entropy of a Spin Ensemble . . . . .	100
C. Spin operators . . . . .	100
D. Maxwell-Bloch Equations . . . . .	100
E. Lorentzian Line Fit . . . . .	102
F. Loop-Gap Resonator . . . . .	104
<b>List of Figures</b>	<b>108</b>
<b>List of Tables</b>	<b>110</b>

<b>References</b>	<b>111</b>
<b>Acknowledgements</b>	<b>122</b>
<b>Curriculum Vitae</b>	<b>124</b>

# List of Publications

The main results presented within this thesis are based on the following peer reviewed journal articles:

- **Solid-state electron spin lifetime limited by phononic vacuum modes**  
T. Astner, J. Gugler, A. Angerer, S. Wald, S. Putz, N. J. Mauser, M. Trupke, H. Sumiya, S. Onoda, J. Isoya, J. Schmiedmayer, P. Mohn, and J. Majer  
*Nature Materials* **17**, 313-317 (2018)
- **Ab initio calculation of the spin lattice relaxation time  $T_1$  for nitrogen-vacancy centers in diamond**  
J. Gugler, T. Astner, A. Angerer, J. Schmiedmayer, J. Majer, and P. Mohn  
*Phys. Rev. B.* **98**, 214442 (2018)
- **Collective strong coupling with homogeneous Rabi frequencies using a 3D lumped element microwave resonator**  
A. Angerer, T. Astner, D. Wirtitsch, H. Sumiya, S. Onoda, J. Isoya, S. Putz, and J. Majer  
*Applied Physics Letters* **109**, 033508 (2016)
- **Coherent Coupling of Remote Spin Ensembles via a Cavity Bus**  
T. Astner, S. Nevlacsil, N. Peterschofsky, A. Angerer, S. Rotter, S. Putz, J. Schmiedmayer, and J. Majer  
*Phys. Rev. Lett.* **118**, 140502 - Published 5 April 2017

Additionally, further contributions have been made to other work:

- **Ultralong relaxation times in bistable hybrid quantum systems**  
A. Angerer, S. Putz, D. O. Krimer, T. Astner, M. Zens, R. Glattauer, K. Streltsov, W. J. Munro, K. Nemoto, S. Rotter, J. Schmiedmayer, and J. Majer  
*Science Advances*, 08 Dec. 2017, E1701626
- **Superradiant emission from colour centres in diamond**  
A. Angerer, K. Streltsov, T. Astner, S. Putz, H. Sumiya, S. Onoda, J. Isoya, W. J. Munro, K. Nemoto, J. Schmiedmayer, and J. Majer  
*Nature Physics*, **14**, 1168-1172 (2018)

# Introduction

Fluorescent colour centres are lattice defects that consist of one or several impurity atoms or vacant lattice sites. A vast variety of several hundreds of these colour centres have already been studied for decades, as they are responsible for the colour of diamond gemstones [1].

But now diamond colour centres have also entered the field of (quantum) physics and even biology for several very different applications. Studies showed that diamond nano-particles don't present any toxic effects and, therefore, can be functionalized and internalized by cells. There, these nano particles are promising candidates for exceptionally robust fluorescent dyes, with applications in bio-labelling [2] and even neuron imaging [3].

In contrast to that, physicists are working on understanding and controlling the electronic properties of single and large ensembles of these lattice impurities. A system with outstanding properties is the nitrogen-vacancy defect (NV) [1, 4, 5]. Well isolated in the diamond lattice, it presents quantum properties even at room temperature. Back in 1997 the detection of electron paramagnetic resonance (EPR) stimulated and triggered a widespread research effort in the context of quantum information science with NV centres [6, 7]. Even now the NV centre presents itself as an important system for quantum simulation [8] and finds many applications as very robust and high precision (quantum) sensor [9–11] for magnetic fields [12–15].

Recently, the field of cavity quantum electrodynamics, awarded with a Nobel prize in 2012 [16, 17], has become very prominent. The controlled and coherent energy exchange between atomic systems [18] and a bosonic cavity mode has led to a cascade of research in the realm of quantum computation, simulation and communication.

The aim of this thesis is to combine the field of strong light matter interaction with the NV defect centre in diamond. Coupling a large ensemble of NV centres to a bosonic cavity mode [19–21] generates a unique hybrid system [22, 23] that enables one to address questions concerning the fundamental properties of the NV system like the spin lattice relaxation at low temperatures. Acquiring a profound understanding of the most fundamental properties of the NV system is beneficial for developing new technologies and engineering systems with desired properties.

The thesis at hand, therefore, is divided into a 'Theoretical Concepts' part where the individual constituents, namely the NV centre and the superconducting cavities together with general concepts of cavity QED are introduced. In the subsequent 'Scientific Results' part, the combined hybrid system is used to address the following fundamental questions: What process governs the longitudinal relaxation of the NV spin in diamond in the low temperature regime? How long is the typical spin life time?

In the final part, the coupling of two remote spin ensembles via a common bosonic mode is presented and analysed. This experiment demonstrates the capabilities and robustness of large ensembles of NV centres for quantum information tasks and is a step towards studying physical properties in two domain systems.

**Part I.**  
**Theoretical Concepts**

# 1. The Nitrogen Vacancy Colour Centre in Diamond

Diamond is a material known for its outstanding properties, such as extreme hardness, the highest thermal conductivity of any natural occurring materials, transparency to ultraviolet light and its chemical resistance. In comparison to other materials, diamond shows extreme values for almost all different properties. This has led to a wide range of industrial applications such as diamond drill bits for oil wells, diamond enhanced concrete saws, windows for x-ray tubes, heat sinks, micro bearings, and many more [24].

In the recent past, diamond has also entered the quantum information and spintronics world as a useful (host) material - heralding the so-called diamond age of spintronics [25]. A reason for that is the well protected environment provided by the diamond lattice. One can characterize this property by means of a low coupling between the electrons and phonons - a consequence of the low phonon density of states (high Debye temperature) [26] in diamond.

Among the vast variety of over 100 different colour centres that exist in diamond, many have been studied to find their charge and spin state to harness these systems for new quantum technologies [27].

However, one of the most prominent ones is the negatively charged nitrogen vacancy centre (NV). Over the last years it has emerged as a promising platform for a huge variety of different applications. For example, quantum sensing with high spatial resolutions [28, 29], bio-compatible fluorescence markers [2, 30], quantum information processing tasks [6], single photon sources [10] and quantum communication applications [31].

The NV centre itself can be seen as a point-like defect that is formed by a nitrogen atom that substitutes a carbon atom and a neighbouring vacancy in the diamond lattice [32, 33]. Nitrogen has five valence electrons, where three of them covalently bind to the nearest neighbouring carbon atoms. At the vacancy three electrons are unpaired. Two of them will form a quasi covalent bond, whereas one will remain unpaired. If in addition an electron is captured from the surrounding lattice, the total charge state is



negative and two electrons remain unpaired<sup>1</sup>. This leads to a paramagnetic ground state with the spin triplet state  $S = 1$  ( ${}^3A_2$ ).

The system further exhibits an optical transition to an excited state with a zero phonon line (ZPL) at 637 nm [34]. This property makes this system attractive for realization of an addressable spins in the solid state for quantum computing and other studies [35–38].

## 1.1. Ground State Level Structure

Spin-spin interaction between the two unpaired electrons of the NV centre lifts the degeneracy of the triplet states ( $m_s = (0, \pm 1)$ ) without any external DC magnetic field and determines its quantization axis.

In the reference frame of the defect centre, the Hamiltonian with the magnetic Zeeman interaction reads

$$\hat{H}_{\text{NV}} = \hbar D \hat{S}_z^2 + \hbar E (\hat{S}_x^2 - \hat{S}_y^2) + \hbar \mu_{\text{NV}} \mathbf{B}_{\text{ext}} \hat{\mathbf{S}}, \quad (1.1)$$

where  $\hat{\mathbf{S}} = (\hat{S}_x, \hat{S}_y, \hat{S}_z)$  are the Pauli matrices for a  $S = 1$  system. The two parameters  $D \approx 2.88$  GHz and  $E \approx 8$  MHz [5, 39, 40] are the fine structure constants that arise due to the spin-spin interaction. The interaction with an external magnetic field is given via the magnetic moment  $\mu_{\text{NV}} = 28$  MHz/mT - which allows tuning of the spin transitions.

In Figure 1.1 the structure of the NV centre in the diamond lattice together with the level scheme of the ground state triplet is presented.

---

<sup>1</sup>To simplify the notation and readability, the usually used symbol  $\text{NV}^-$  for the negative charge state is replaced by the abbreviation NV.

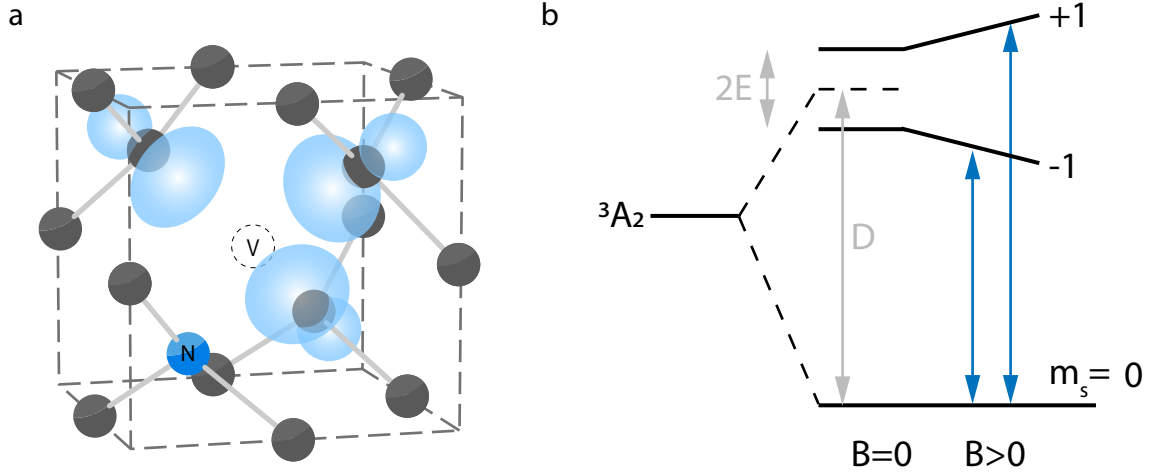


**Figure 1.1.: NV level structure.** **a**, Diamond unit cell with a single nitrogen vacancy centre. A nitrogen atom (dark blue) substitutes a carbon atom (black). Adjacent to the nitrogen a lattice site is empty (dashed circle). The blue shaded orbitals illustrate an iso-surface of the spin density around the lattice vacancy. **b**, Level structure of the  ${}^3A_2$  ground state triplet. The zero field splitting parameter lifts the degeneracy between the  $m_s = 0$  and  $m_s = \pm 1$  states. An additional lattice strain mixes the  $m_s = \pm 1$  states and splits them by  $2E$ . Applying a DC bias field, the  $m_s = \pm 1$  states can be tuned according to the Zeeman effect. Images similar to [41, 42].

Interactions of the NV centre with the omnipresent  ${}^{14}N$  and the natural occurrence of  ${}^{13}C$  in the diamond lattice can be implemented with a hyperfine and a quadrupole tensor [1, 5]. In the Hamiltonian of Equation (1.1) these parts have been omitted, since they do not play any major role in the physical effects presented in this thesis.

## 1.2. Statistical Mechanics of a NV Ensemble

Here a statistical mechanics description of a large ensemble of nitrogen vacancy spins is given. The treatment takes the three-level nature of the ground state triplet into account, which will be important for some experimental observations. Starting from the partition function, the thermal occupation of the levels and quantities like internal energy and heat capacity can be derived.

First, let us consider a generic ensemble of distinguishable three-level systems with  $\varepsilon_0$  as the lowest energy level and two degenerate excited states  $\varepsilon_{\pm}$ . The term 'distinguishable' is justified as each of these systems is positioned at a unique location in the lattice, but all have identical properties. It is straightforward to write down the

partition function [43] for that system in the form

$$Z(T) = e^{-\varepsilon_0/k_B T} + 2e^{-\varepsilon_{\pm}/k_B T} = e^{-\varepsilon_0/k_B T} (1 + 2e^{-\varepsilon/k_B T}) = Z_0 \cdot Z_{\text{therm}}, \quad (1.2)$$

with  $\varepsilon$  as the energy difference between the ground and excited states ( $\varepsilon = \varepsilon_{\pm} - \varepsilon_0 \equiv \hbar\omega$ ). In Equation (1.2) the partition function can be factorized into a zero-point and thermal factor. This comes in handy for calculating physical quantities that require the logarithm of the partition function. They then become a sum of the zero point and a thermal contribution. Since the partition function resembles a sum over all possible states of the system, the degeneracy of the upper levels has to be taken into account by summing them as many times as the multiplicity of the degeneracy. From the partition function the occupation numbers of the ground state,  $n_0$ , and the excited states,  $n_+$ ,  $n_-$ , can be calculated:

$$n_0(T) = \frac{N}{Z} e^{-\varepsilon_0/k_B T} = \frac{N}{1 + 2e^{-\varepsilon/k_B T}}, \quad \text{and} \quad (1.3a)$$

$$n_- + n_+ \equiv n_{\pm}(T) = \frac{N}{Z} 2e^{-\varepsilon_{\pm}/k_B T} = \frac{2Ne^{-\varepsilon/k_B T}}{1 + 2e^{-\varepsilon/k_B T}}. \quad (1.3b)$$

By looking at Equation (1.3), it can be seen that in the low temperature limit,  $n_0(T = 0) = N$  and  $n_{\pm}(T = 0) = 0$ , all systems occupy the ground state. Whereas in the high temperature limit ( $T \rightarrow \infty$ ) they evenly occupy all three levels ( $n_+$ ,  $n_- = N/3$  and  $n_0 = N/3$ ).

The characteristic temperature where the transition from the low to the high temperature regime happens is determined by the energy separation between the levels. The exponent determines the so-called scale temperature  $\vartheta = \varepsilon/k_B$ . In the case of the NV centre, the excited  $m_s = \pm 1$  levels are now assumed to be degenerate. For centres with small strain components  $E$ , this presents a good approximation. This leads to a scale temperature of  $\hbar\omega_{0 \rightarrow \pm}/k_B \approx \hbar(2\pi \cdot 2.88 \text{ GHz})/k_B \approx 0.1382 \text{ K}$ . In Figure 1.2 the normalized level population of the ground state and the degenerate excited states are plotted as function of temperature.

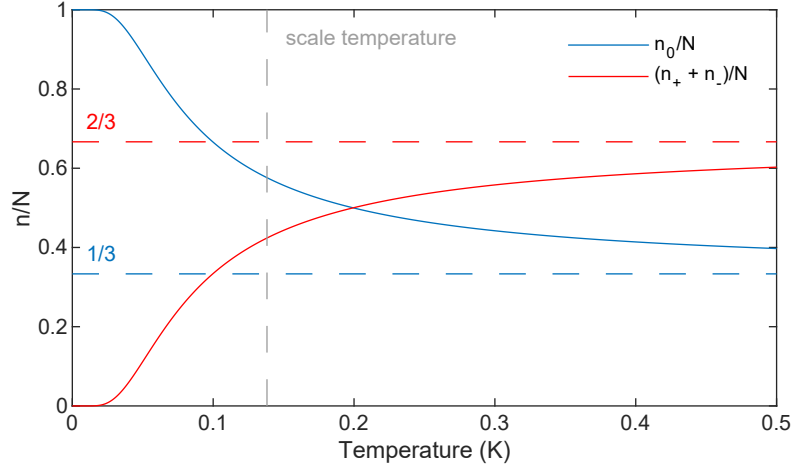


**Figure 1.2.: Temperature-dependent level occupation.** Cooling the ensemble well below the scale temperature allows to thermally polarize it into the ground state. Whereas for temperatures much higher than the scale temperature the energy splitting is negligible and the population in all levels is the same.

### 1.2.1. Internal Energy and Heat Capacity

The internal energy of the ensemble can be now computed with

$$E = -N \frac{\partial \ln Z}{\partial \beta} = N\varepsilon_0 + \frac{2N\varepsilon e^{-\vartheta/T}}{1 + 2e^{-\vartheta/T}}, \quad (1.4)$$

where the definition  $\beta = 1/k_B T$  was used. Again, in the low temperature limit the energy is given as  $E(0) = N\varepsilon_0$  and approaches  $E(T \rightarrow \infty) = E(T = 0) + 2N\varepsilon/3$  asymptotically for high temperatures. As the internal energy of the system is known, the heat capacity of the spin system can be derived by

$$c = \frac{\partial E}{\partial T} = Nk_B \left( \frac{\vartheta}{T} \right)^2 \frac{2e^{-\vartheta/T}}{(2e^{-\vartheta/T} + 1)^2}, \quad (1.5)$$

with the corresponding plot in Figure 1.3.

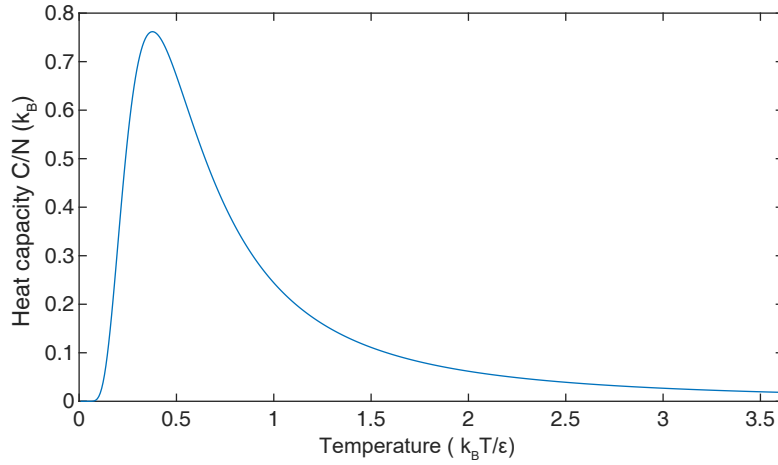


**Figure 1.3.: Schottky anomaly of the heat capacity.** With increasing temperature the energy separation between ground and the doubly excited state matches the thermal energy. Spins can easily be thermally excited and, therefore, the heat capacity has a peak close to the scale temperature. With increasing temperature the total spin population is equally distributed over all levels and the system does not gain energy with rising temperature.

The line shape of the heat capacity of this system shows a peak at a temperature that corresponds roughly to the energy separation between the ground and the excited states. This phenomenon is called Schottky anomaly and typically occurs for systems with limited amount of available energy levels. At low temperatures, the distance between the ground and the excited states is so large that the thermal energy is not sufficient to excite spins from the ground state. Approaching the scale temperature it is easy to excite spins and the heat capacity reaches a peak.

In the high temperature limit the situation changes: The number of particles occupying the lower and the upper energy state are the same. Hence, the overall energy can not increase anymore with rising temperature. For completeness, the expression for the system entropy is displayed in Appendix B.

### 1.3. Spin Lattice Relaxation

Since one of the main results of this thesis is the spin lattice relaxation at low temperatures, the different processes that lead to energy relaxation are introduced here. The spin lattice relaxation describes the energy relaxation along the longitudinal axis of the defect. By considering an excited spin, longitudinal relaxation is the process that drives the system back into thermal equilibrium with the environment.

Embedded in a solid, one concludes that coupling to the electromagnetic vacuum plays

a negligible role in the spin relaxation compared to the interaction with lattice phonons [44–47]. Phonons are collective quantum vibrational excitations which propagate through the diamond crystal. Their interaction intensity with the orbital states of the NV centre depends on the coupling between the defect and all existing phonon modes (acoustic, optical and quasi-localized) [48–50].

In the following part, a theoretical microscopic model of spin lattice relaxation associated with an ensemble of NV centres in diamond will be introduced. The reader is advised to consult reference [51], since the detailed derivations are all covered there and this part is based on this specific research paper.

A suitable description of a NV spin embedded in the solid state is given by the following Hamiltonian

$$\hat{H} = \hat{H}_{\text{NV}} + \hat{H}_{\text{s-ph}} + \hat{H}_{\text{ph}}, \quad (1.6)$$

where the first part is the ground state Hamiltonian of the NV centre (Equation (1.1)), the second describes the interaction of the spin state with phonons and the third term represents the phonon bath. The NV centre is part of the  $C_{3v}$  symmetry group and can be modelled as a two electron-hole system. The wave functions, therefore, can be expanded as linear combinations of two electron wave functions. The single electron orbitals consist of the carbon and nitrogen dangling bonds. For the sake of simplicity, the lattice strain parameter  $E$  is set to zero, which results in degenerate  $m_s = \pm 1$  states in the the orbital ground state  $|A_2\rangle$ . Adjusting the Hamiltonian in Equation (1.1) accordingly leads to

$$H_{\text{NV}} = \hbar D \hat{S}_z^2 + \hbar \mu_{\text{NV}} B_0 \hat{S}_z, \quad (1.7)$$

with the assumption that an external magnetic field is aligned along the NV principal axis. The spin-phonon interaction term of the Hamiltonian in Equation (1.6) consists of operators proportional to displacements of the nuclei. In that framework, they can be quantized as phonon modes, fulfilling the bosonic commutation relations  $[\hat{b}_k, \hat{b}_{k'}^\dagger] = \delta_{k,k'}$  for the creation and annihilation operators. The phonon modes are then expressed as linear combinations of lattice phonons that are classified by the symmetry of the NV centre. One then derives a general interaction Hamiltonian in the form

$$\hat{H}_{\text{s-ph}} = \sum_i \left[ \sum_{k \in \Gamma_i} \lambda_{k,i} \hat{x}_k + \sum_{k \otimes k' \in \Gamma_i} \lambda_{kk',i} \hat{x}_k \hat{x}_{k'} \right] \hat{F}_i(\mathbf{S}). \quad (1.8)$$

Here  $i = x, y, x', y', z$  labels the spin,  $\Gamma_{x,y,x',y'} = E$  and  $\Gamma_z = A_1$ .  $E$  and  $A_1$  are the irreducible representations of the  $C_{3v}$  point group. The linear and quadratic spin-phonon coupling constants are given with  $\lambda_{k,i}$  and  $\lambda_{kk',i}$ , respectively. The operator  $\hat{x}_k$  can be written as  $\hat{x}_k = \hat{b} + \hat{b}_k^\dagger$ .

Suitable spin functions can be constructed from the basis states  $|m_s = 1\rangle = (1, 0, 0)$ ,

$|m_s = 0\rangle = (0, 1, 0)$  and  $|m_s = -1\rangle = (0, 0, 1)$ , that diagonalize the spin Hamiltonian Equation (1.7). These functions are  $\hat{F}_x(\mathbf{S}) = \hat{S}_x^2 - \hat{S}_y^2$ ,  $\hat{F}_y(\mathbf{S}) = \hat{S}_x\hat{S}_y + \hat{S}_y\hat{S}_x$ ,  $\hat{F}_{x'}(\mathbf{S}) = \hat{S}_x\hat{S}_z + \hat{S}_z\hat{S}_x$ ,  $\hat{F}_{y'}(\mathbf{S}) = \hat{S}_y\hat{S}_z + \hat{S}_z\hat{S}_y$ , and  $\hat{F}_z(\mathbf{S}) = \hat{S}_z^2$ . The explicit matrix representation is presented in Appendix C.

The states  $m_s = +1$  and  $m_s = -1$  are coupled via the operators  $\hat{F}_x(\mathbf{S})$  and  $\hat{F}_y(\mathbf{S})$  with the selection rule  $\Delta m_s = \pm 2$ . The transitions between the  $m_s = 0$  and  $m_s = \pm 1$  with selection rule  $\Delta m_s = \pm 1$  is induced by the operators  $\hat{F}_{x'}(\mathbf{S})$  and  $\hat{F}_{y'}(\mathbf{S})$ . The last part of the Hamiltonian can be written as the sum over all phonon energies in  $k$  modes. The summation over all  $\omega_k$  includes all vibrational modes of the lattice and the NV centre. With the defined bosonic creation and annihilation operators this term reads

$$\hat{H}_{\text{ph}} = \sum_k \hbar\omega_k \hat{b}_k^\dagger \hat{b}_k. \quad (1.9)$$

### 1.3.1. Single Phonon Processes

Having set up a suitable Hamiltonian for spin-phonon interaction, it can now be used in Fermis golden rule to calculate the transition rates and hence the spin lattice relaxation rate. A perturbation theory treatment of the problem will lead to a Raman-like or a single phonon process. Here the discussion will be limited to the single phonon process (first order perturbation), whereas all other processes will be neglected. This is justified, since all higher order processes are frozen out in the low temperature limit.

In the ground state triplet,  $\omega_1 = 2\mu_{\text{NV}}B_0$ ,  $\omega_2 = D + \mu_{\text{NV}}B_0$  and  $\omega_3 = D - \mu_{\text{NV}}B_0$  are the possible transition frequencies. In a typical experimental setup, fields up to 200 mT result in transition frequencies below 10 GHz. For diamond these energies belong to the acoustic branch of phonons in the linear regime of the dispersion relation. Single phonon processes imply that the phonon energy must match the transition energy of the NV centre. The number of phonons satisfying this condition can be calculated by the Bose-Einstein distribution with the mean number of phonons  $n(\omega_k) = [\exp(\hbar\omega_k/k_{\text{B}}T) - 1]^{-1}$  with  $\langle \hat{b}_k^\dagger \hat{b}_k \rangle = n(\omega_k)$  and  $\langle \hat{b}_k \hat{b}_k^\dagger \rangle = 1 + n(\omega_k)$ .

### Fermi's Golden Rule

In the case of a single phonon process the transition rate between two spin levels is given by the Fermi's golden rule in first order corrections for emission and absorption

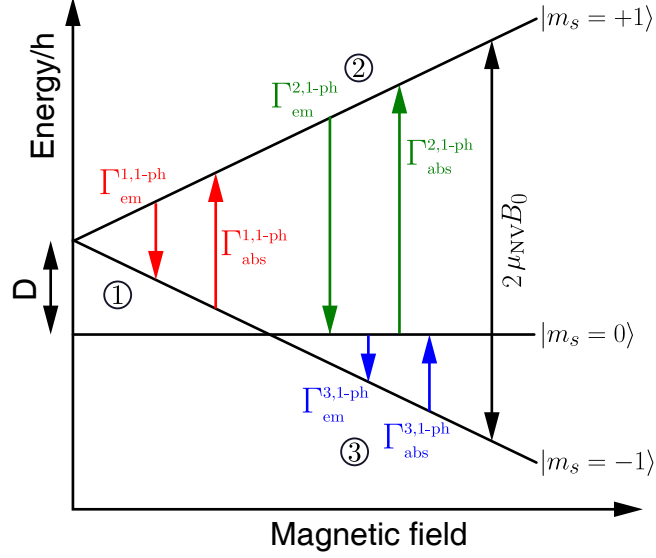


**Figure 1.4.: Relaxation rates between the spin states.** By applying an external DC magnetic field along the NV principal axis the energy difference between the  $m_s$  states can be changed. Three different regimes of spin relaxation can be identified and shown here with colour coded arrows and numbers in circles. The arrow direction differentiates between phonon emission ( $\Gamma_{\text{em}}$ ) and absorption ( $\Gamma_{\text{abs}}$ ) processes. Illustration similar to [51].

in the form

$$\Gamma_{\text{abs}}^{m_s \rightarrow m'_s} = \frac{2\pi}{\hbar^2} \sum_k \left| \langle m'_s, n_k - 1 | \hat{H}_{\text{s-ph}} | m_s, n_k \rangle \right|^2 \times \delta(\omega_{m'_s, m_s} - \omega_k), \quad (1.10a)$$

$$\Gamma_{\text{em}}^{m_s \rightarrow m'_s} = \frac{2\pi}{\hbar^2} \sum_k \left| \langle m'_s, n_k + 1 | \hat{H}_{\text{s-ph}} | m_s, n_k \rangle \right|^2 \times \delta(\omega_{m'_s, m_s} - \omega_k). \quad (1.10b)$$

Here the energy difference between two spin levels is given by  $\omega_{m'_s, m_s} = \omega_{m'_s} - \omega_{m_s}$  and  $|n_k\rangle$  denotes the number of phonons in the mode  $k$ . With the interaction part of the Hamiltonian Equation (1.8) the emission and absorption rates between the spin states  $|m_s = -1\rangle \leftrightarrow |m_s = +1\rangle$  (label  $\Gamma^1$ ) and  $|m_s = 0\rangle \leftrightarrow |m_s = +1\rangle$  (label  $\Gamma^2$ ) are illustrated in Figure 1.4 and given by

$$\Gamma_{\text{abs}}^{1,1-\text{ph}} = \frac{2\pi}{\hbar^2} n(\omega_1) J_1(\omega_1), \quad \Gamma_{\text{em}}^{1,1-\text{ph}} = \frac{2\pi}{\hbar^2} (n(\omega_1) + 1) J_1(\omega_1), \quad (1.11a)$$

$$\Gamma_{\text{abs}}^{2,1-\text{ph}} = \frac{\pi}{\hbar^2} n(\omega_2) J_2(\omega_2), \quad \Gamma_{\text{em}}^{2,1-\text{ph}} = \frac{\pi}{\hbar^2} (n(\omega_2) + 1) J_2(\omega_2). \quad (1.11b)$$



The terms  $J_1(\omega)$  and  $J_2(\omega)$  are the spectral density functions in the form

$$J_1(\omega) = \sum_{k \in E} (\lambda_{k,x}^2 + \lambda_{k,y}^2) \delta(\omega - \omega_k) \quad (1.12a)$$

$$J_2(\omega) = \sum_{k \in E} (\lambda_{k,x'}^2 + \lambda_{k,y'}^2) \delta(\omega - \omega_k) \quad (1.12b)$$

In the case of transition rates between the  $|m_s = 0\rangle \leftrightarrow |m_s = -1\rangle$  the strength of the external magnetic field has to be considered. It defines the sign of the transition frequency  $\omega_3 = D - \mu_{\text{NV}}B_0$ . For the case  $\omega_3 > 0$ , where  $|m_s = 0\rangle$  is the ground state, emission and absorption have the form

$$\Gamma_{\text{abs}}^{3,1\text{-ph}} = \frac{\pi}{\hbar^2} n(\omega_3) J_2(\omega_3), \quad (1.13a)$$

$$\Gamma_{\text{em}}^{3,1\text{-ph}} = \frac{\pi}{\hbar^2} (n(\omega_3) + 1) J_2(\omega_3). \quad (1.13b)$$

In the  $\omega_3 < 0$  case, emission and absorption are swapped and the rates can be written as

$$\Gamma_{\text{abs}}^{3,1\text{-ph}} = \frac{\pi}{\hbar^2} n(|\omega_3|) J_2(|\omega_3|), \quad (1.14a)$$

$$\Gamma_{\text{em}}^{3,1\text{-ph}} = \frac{\pi}{\hbar^2} (n(|\omega_3|) + 1) J_2(|\omega_3|). \quad (1.14b)$$

The total transition rate involving all possible single phonon absorption and emission processes can be written as a sum over all individual rates

$$\Gamma_{1\text{-ph}} = \sum_{i=1}^3 (\Gamma_{\text{abs}}^{i,1\text{-ph}} + \Gamma_{\text{em}}^{i,1\text{-ph}}) = \sum_{i=1}^3 A_i \coth\left(\frac{\hbar\omega_i}{2k_B T}\right) \quad (1.15)$$

The prefactors  $A_i$  in Equation (1.15) represent the spectral density function at the given frequency,  $A_1 = 2\pi J_1(\omega_1)$ ,  $A_2 = \pi J_2(\omega_2)$ , and  $A_3 = \pi J_2(|\omega_3|)$ .

### Continuous Frequency Limit

As the parameters  $A_1$  to  $A_3$  determine how strongly each part contributes to the overall spin lattice relaxation rate, they can be calculated looking at the limit of continuous frequencies for phonons,  $\omega_k \rightarrow \omega$ . The linear coupling constants scale as [52]:

$$\lambda_{k,i} \rightarrow \lambda_i(\omega) = \lambda_{0i} \left(\frac{\omega}{\omega_D}\right)^\nu, \quad 0 \leq \omega \leq \omega_D. \quad (1.16)$$

This transforms the discrete linear single phonon coupling constant to  $\lambda_i(\omega)$  with the phenomenological parameter  $\nu$ , which models the coupling strength of acoustic phonons. Since the NV centre breaks the symmetry of the whole system, the parameter  $\nu$  has the value 1/2. The Debye frequency of diamond is given by  $\omega_D = (3/(4\pi n))^{1/3}v_s$ , where  $n$  denotes the atom density and  $v_s$  the speed of sound in diamond. The constant  $\lambda_{0i}$  is the magnitude of the coupling constant at the Debye frequency.

In the Debye approximation ( $\omega \leq \omega_D = v_s k_D$ ) with the dispersion relation  $\omega_k = v_s |\mathbf{k}|$  the density of states for acoustic phonons has the form:

$$\begin{aligned} \mathcal{D}^{(d)}(\omega) &= \Omega \int \frac{d^d k}{(2\pi)^d} \delta(\omega - v_s |\mathbf{k}|) \\ &= \frac{\Omega}{(2\pi)^d} \int d\hat{\Omega}_d \int_0^{k_D} dk k^{d-1} \delta(\omega - v_s k) \\ &= D_0 \left( \frac{\omega}{\omega_D} \right)^{d-1} \Theta(\omega_D - \omega), \end{aligned} \quad (1.17)$$

where d-dimensional spherical coordinates with  $d^d k = d\hat{\Omega}_d dk k^{d-1}$  have been used and  $\hat{\Omega}_d$  is the solid angle in d-dimensions.  $D_0 = \Omega \hat{\Omega}_d \omega_D^{d-1} / ((2\pi)^d v_s^d) > 0$  is a positive normalization constant for the lattice dimensions  $d = 1, 2, 3$  and  $\Omega$  the unit cell volume. The Debye frequency defines the upper limit frequency cut-off by the Heaviside functional  $\Theta(\omega_D - \omega)$ . Using  $D_0 = \Omega \omega^2 / (2\pi^2 v_s^3)$  for the three-dimensional lattice, the following expressions for the spectral density functions is obtained

$$\begin{aligned} J_1(\omega) &= \sum_{k \in E} [\lambda_x^2(\omega_k) + \lambda_y^2(\omega_k)] \delta(\omega - \omega_k) \\ &\rightarrow \Omega \int \frac{d^3 k}{(2\pi)^3} [\lambda_x^2(\omega_k) + \lambda_y^2(\omega_k)] \delta(\omega - \omega_k) \\ &= [\lambda_x^2(\omega) + \lambda_y^2(\omega)] \Omega \int \frac{d^3 k}{(2\pi)^3} \delta(\omega - \omega_k) \\ &= [\lambda_x^2(\omega) + \lambda_y^2(\omega)] \mathcal{D}^{(3)}(\omega), \quad \text{and} \end{aligned} \quad (1.18)$$

$$J_2(\omega) = [\lambda_{x'}^2(\omega) + \lambda_{y'}^2(\omega)] \mathcal{D}^{(3)}. \quad (1.19)$$

As a final result the pre-factors  $A_i$  of the total relaxation rate Equation (1.15) can

be expressed as

$$A_1 = \frac{\Omega (\lambda_{0x}^2 + \lambda_{0y}^2)}{\pi v_s^3 \omega_D} (2\gamma_s B_0)^3, \quad (1.20a)$$

$$A_2 = \frac{\Omega (\lambda_{0x'}^2 + \lambda_{0y'}^2)}{2\pi v_s^3 \omega_D} (D + \gamma_s B_0)^3, \quad (1.20b)$$

$$A_3 = \frac{\Omega (\lambda_{0x'}^2 + \lambda_{0y'}^2)}{2\pi v_s^3 \omega_D} (D - \gamma_s B_0)^3. \quad (1.20c)$$

By looking at Equation (1.15), the individual parts of the total transition rate between the different states depend on the total number of phonons present in the lattice and the density of states at a certain phonon frequency. In the experimental results part of this thesis, the spin lattice relaxation in large ensembles of NV spins in diamond is presented. There, the case of zero magnetic field is treated, which results in  $A_1 = 0$  and  $A_2 = A_3$ . Furthermore, for temperatures larger than the transition frequency,  $k_B T \gg \hbar \omega_i$ , the total relaxation rate has a linear scaling with increasing temperature,  $\Gamma^{i,1-ph} \propto T$ . In the opposite case,  $k_B \ll \hbar \omega_i$  the relaxation rate loses its temperature dependence and has a constant value.

For second-order corrections in Fermi's golden rule, the work by A. Norambuena [51] is recommended. From there, all the previous derivations and descriptions have been taken and more details can be found.

### 1.3.2. Single Phonon Relaxation Dynamics

The starting point here is a general solution in the low temperature regime. From that the limit of zero magnetic field is derived for the single phonon-spin interaction dynamics. The approach is to set up a Markovian quantum master equation that includes the reduced density operator  $\hat{\rho}(t) = \text{Tr}(\hat{\rho}_{NV+ph})$ . In a Born approximation the initial uncorrelated state at time  $t_0$  of the spin and phonon bath can be written as  $\hat{\rho}_{NV+ph}(t_0) = \hat{\rho}_{NV}(t_0) \otimes \hat{\rho}_{ph}(t_0)$ . Together with the interaction Hamiltonian in Equation (1.8) the equation is given by

$$\dot{\hat{\rho}} = \frac{1}{i\hbar} [\hat{H}_{NV}, \hat{\rho}] + \mathcal{L}_{1-ph} \hat{\rho}. \quad (1.21)$$

The Lindblad term that describes the non-unitary (dissipative spin lattice relaxation) evolution of the density matrix for the single phonon process reads

$$\mathcal{L}_{1\text{-ph}}\hat{\rho} = \sum_{i=1}^3 \left[ \Gamma_{\text{abs}}^{i,1\text{-ph}} \mathcal{L} [L_+^i] \hat{\rho} + \Gamma_{\text{em}}^{i,1\text{-ph}} \mathcal{L} [L_-^i] \hat{\rho} \right]. \quad (1.22)$$

The index  $i$  runs over the different spin transitions available in the ground state triplet. The Lindblad superoperators are defined with the spin operators

$$L_+^1 = |m_s = +1\rangle \langle m_s = -1| = (L_-^1)^\dagger, \quad (1.23)$$

$$L_+^2 = |m_s = +1\rangle \langle m_s = 0| = (L_-^2)^\dagger, \quad (1.24)$$

$$L_+^3 = |m_s = -1\rangle \langle m_s = 0| = (L_-^3)^\dagger. \quad (1.25)$$

The discussion here is limited to relaxation processes at low temperatures ( $k_B T \ll \hbar\omega$ ) and considers only single phonon processes, hence Equation (1.22) does not include any Lindblad terms for two phonon processes. Effects of isotropic field noise that could lead to a magnetic relaxation rate [53] have been neglected in the Lindblad operators.

### Low Temperature Limit

Part of the thesis will deal with the experimental measurement of the low temperature spin lattice relaxation limit of the NV centre. The dynamics is covered by the introduced quantum master equation. The observables associated with the experiment are the relative spin populations,  $p_1 = \langle m_s = 1 | \hat{\rho} | m_s = 1 \rangle$ ,  $p_2 = \langle m_s = 0 | \hat{\rho} | m_s = 0 \rangle$  and  $p_3 = \langle m_s = -1 | \hat{\rho} | m_s = -1 \rangle$ .

In Figure 1.5 the different rates by which spin population is changed are illustrated. The differential equations that describe the dynamics of the population have the form

$$\frac{dp_1}{dt} = -(\gamma_{+-} + \Omega_{+0}) p_1 + \Omega_{0+} p_2 + \gamma_{-+} p_3, \quad (1.26a)$$

$$\frac{dp_2}{dt} = -(\Omega_{0+} + \Omega_{0-}) p_2 + \Omega_{+0} p_1 + \Omega_{-0} p_3, \quad (1.26b)$$

$$\frac{dp_3}{dt} = -(\Omega_{0-} + \gamma_{-+}) p_3 + \gamma_{+-} p_1 + \Omega_{0-} p_2. \quad (1.26c)$$

The different relaxation rates in Equation (1.26) can be expressed by using the param-

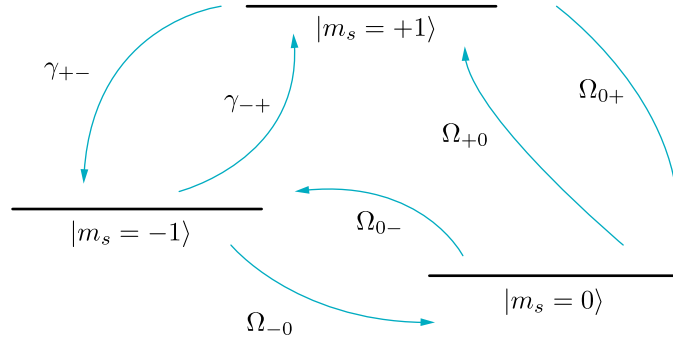


**Figure 1.5.: Relaxation processes mediated by a single phonon.** The absorption ( $\gamma_{-+}, \Omega_{0-}, \Omega_{0+}$ ) and emission ( $\gamma_{+-}, \Omega_{-0}, \Omega_{+0}$ ) processes change the spin population of the different states. Depending on the strength of an external magnetic field the  $|m_s = 0\rangle$  and  $|m_s = -1\rangle$  state can exchange their role as the lowest energy level. Illustration similar to [51].

eters in Equation (1.20):

$$\gamma_{+-} = A_1 (1 + n_1) \quad (1.27a)$$

$$\gamma_{-+} = A_1 n_1, \quad (1.27b)$$

$$\Omega_{+0} = A_2 (1 + n_2) \quad (1.27c)$$

$$\Omega_{0+} = A_2 n_2, \quad (1.27d)$$

$$\Omega_{-0} = A_3 (1 + n_3), \quad (1.27e)$$

$$\Omega_{0-} = A_3 n_3, \quad (1.27f)$$

with  $n_i = [\exp(\hbar\omega_i/k_B T) - 1]^{-1}$  as the thermal equilibrium phonon number.

### Zero Magnetic Field Limit

In the previous part the discussion was limited to the regime where the temperature is lower than the transition energies associated with the NV centre. Here another constraint is introduced - the magnetic field is set to zero. By neglecting any strain in the NV centre the states  $|m_s = +1\rangle$  and  $|m_s = -1\rangle$  are degenerate. If in addition electric field fluctuations are neglected, the transition rates between the  $|m_s = \pm 1\rangle$  vanish [54]. Taking all this into account the resulting emission and absorption rates

have the form

$$\Gamma_{abs} = \Gamma_0 \bar{n} \quad (1.28a)$$

$$\Gamma_{em} = \Gamma_0 (\bar{n} + 1). \quad (1.28b)$$

Here,  $\bar{n}$  denotes the mean number of phonons at the zero-field splitting frequency  $D$ . As mentioned before, the parameters  $A_2$  and  $A_3$  are equal at zero magnetic field and  $A_1 = 0$ , hence  $\Gamma_0$  can be calculated with Equation (1.20) and has the form

$$\Gamma_0 = \frac{\Omega D^3 (\lambda_{0x'}^2 + \lambda_{0y'}^2)}{2\pi v_s^3 \omega_D}. \quad (1.29)$$

The differential rate equations covering the dynamics of the level population then simplify to

$$\frac{dp_1}{dt} = \Gamma_0(1 + \bar{n})p_1 + \Gamma_0 \bar{n} p_2, \quad (1.30a)$$

$$\frac{dp_2}{dt} = -2\Gamma_0 \bar{n} p_2 + \Gamma_0(1 + \bar{n})p_1 + \Gamma_0(1 + \bar{n})p_3, \quad (1.30b)$$

$$\frac{dp_3}{dt} = \Gamma_0(1 + \bar{n})p_1 + \Gamma_0 \bar{n} p_3. \quad (1.30c)$$

As the states  $|m_s = \pm 1\rangle$  are degenerate, they can be treated with the operator  $\langle S_z^2(t) \rangle = p_1(t) + p_2(t)$  and  $p_1(t) + p_2(t) + p_3(t) = 1$ . This simplifies the system of equations to

$$\frac{d\langle S_z^2(t) \rangle}{dt} = -\Gamma_0(1 + 3\bar{n}) \langle S_z^2(t) \rangle + 2\Gamma_0 \bar{n}, \quad (1.31a)$$

$$\frac{dp_2}{dt} = -\Gamma_0(1 + 3\bar{n})p_2(t) + \Gamma_0(1 + \bar{n}). \quad (1.31b)$$

The solution is an exponential function and, therefore, is obtained by taking arbitrary initial level populations  $p_i(0) = p_{i0}$  ( $i = 1, 2, 3$ ),

$$\langle S_z^2(t) \rangle = \langle S_z^2(T) \rangle_{st} - (\langle S_z^2(T) \rangle_{st} - p_{10} - p_{30}) e^{-\Gamma_0(1+3\bar{n})t}, \quad (1.32a)$$

$$p_2(t) = (p_2(T))_{st} - ((p_2(T))_{st} - p_{20}) e^{-\Gamma_0(1+3\bar{n})t} \quad (1.32b)$$

Solving the equations for the steady state ( $t \rightarrow \infty$ ) leads to

$$\langle S_z^2(T) \rangle_{st} = \frac{2}{e^{\hbar D/k_B T} + 2}, \quad (1.33a)$$

$$(p_2(T))_{st} = \frac{e^{\hbar D/k_B T}}{e^{\hbar D/k_B T} + 2}, \quad (1.33b)$$

which is consistent with the derivation of the thermal steady state level populations in Equation (1.3), calculated by means of statistical mechanics. The spin lattice relaxation induced by spin-phonon interaction is proportional to  $\Gamma_0$  and the mean number of phonons  $\bar{n}$ . The associated temperature dependence of the relaxation time  $T_1$  is given by  $\Gamma = 1/T_1 = \Gamma_0(1 + 3\bar{n})$  with limit  $\Gamma(T \rightarrow 0) = \Gamma_0$ , the relaxation rate reaches the constant value  $\Gamma_0$ .

A solution for small magnetic fields is presented in Appendix A.

## 2. Light Matter Interaction

The previous chapter introduced the NV centre, some of its electronic properties together with a theoretical treatment of the spin lattice relaxation mechanism. Here the second topic, light matter interaction, is briefly introduced as it is the second building block for the experiments discussed within this thesis. As this description is suitable for many different systems, the discussion here is given by a generic two or three level system interacting with a harmonic oscillator mode. This model is able to describe a variety of interesting physical systems like atoms or nuclear spins interacting with the electromagnetic field, electron and phonon modes, and superconducting qubits interacting with nano-mechanical or coplanar waveguide resonators. A description of all these systems and their dynamics is given by the Rabi Hamiltonian [55]. The pure quantum mechanical extension of that semi-classical description is the Jaynes-Cummings (JC) [56] model.

In the following description a two-level system (TLS) with its ground state  $|g\rangle$  and excited state  $|e\rangle$ , separated by  $\hbar\omega_{ge}$ , is considered. The interaction with a single mode of radiation is described with the following Hamiltonian,

$$\hat{H}_{\text{JC}} = \overbrace{\hbar\omega_c \hat{a}^\dagger \hat{a} + \hbar\omega_{eg} |e\rangle \langle e|}^{\hat{H}_0} + \overbrace{\hbar g(\hat{a}^\dagger \hat{\sigma}^- + \hat{\sigma}^+ \hat{a})}^{\hat{H}_{\text{int}}}, \quad (2.1)$$

whereas a graphical illustration of the system is given in Figure 2.1. Here the rotating wave approximation (RWA) [57] has been used. All fast rotating and not energy conserving terms have been dropped. The TLS is considered to be close to resonance with the cavity mode ( $\omega_c \approx \omega_{eg}$ ) and the coupling strength fulfils the condition  $g \ll \min\{\omega_c, \omega_{eg}\}$ .

In Equation (2.1)  $\hat{\sigma}_z$  and  $\hat{\sigma}_+ + \hat{\sigma}_- = \hat{\sigma}_x$  are the standard Pauli matrices and  $\hat{a}^\dagger$  and  $\hat{a}$  refer to the bosonic creation and annihilation operators of the harmonic oscillator mode.



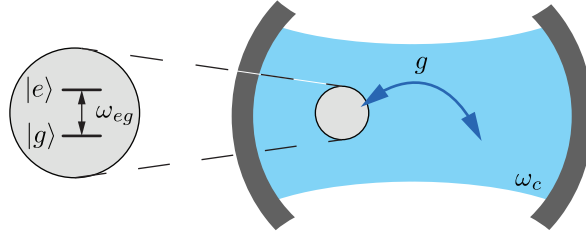


**Figure 2.1.: Jaynes-Cummings system.** Illustration of the Hamiltonian in Equation (2.1). A two-level system with the transition energy  $\hbar\omega_{eg}$  interacts with a cavity mode at energy  $\hbar\omega_c$ . The rate of energy exchange is given by  $g$ .

## 2.1. Jaynes-Cummings Model

The first term in the Hamiltonian of Equation (2.1),  $H_0$ , gives the unperturbed energies of the two level system and the photonic states with energies

$$\hat{H}_0 |g, n\rangle = n\hbar\omega_c |g, n\rangle \quad \text{and} \quad \hat{H}_0 |e, n-1\rangle = (n\hbar\omega_c - \hbar\Delta) |e, n-1\rangle, \quad (2.2)$$

with  $\Delta := \omega_c - \omega_{eg}$ . From the structure of the interaction part  $H_{\text{int}}$  it can be seen that the total photonic and atomic excitation number is conserved. Therefore, only energy levels of  $H_0$  in a two-dimensional subspace  $\{|g, n\rangle, |e, n-1\rangle\}$ , are coupled by  $\hat{H}_{\text{int}}$  with the strength  $g\sqrt{n}$ :

$$\hat{H}_{\text{int}} |g, n\rangle = g\sqrt{n} |e, n-1\rangle, \quad \hat{H}_{\text{int}} |e, n-1\rangle = g\sqrt{n} |g, n\rangle. \quad (2.3)$$

The corresponding energy ladder of the bare states and the coupled levels is displayed in Figure 2.2.

## 2. Light Matter Interaction

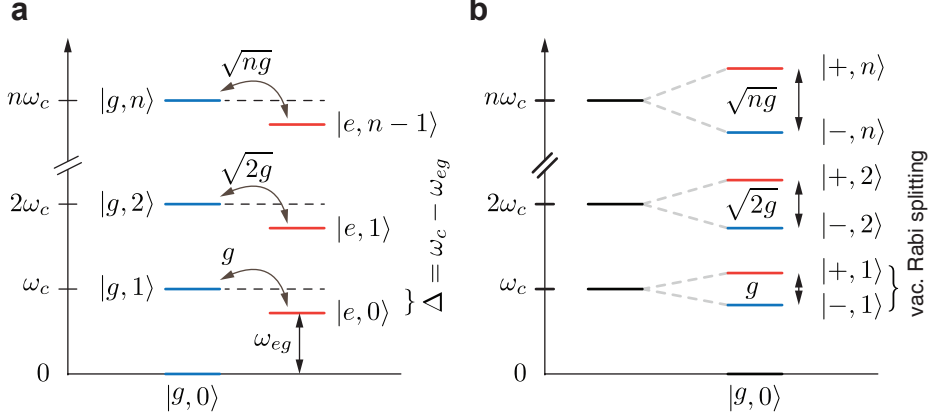


**Figure 2.2.: Energy level diagram.** **a**, Jaynes Cumings energy ladder presenting the bare atomic and field states ( $|g, n\rangle$  and  $|e, n\rangle$ ). **b**, Dressed state picture,  $|\pm, n\rangle$  in the case of atomic transition and field in resonance.

Furthermore, the total Hamiltonian can be partitioned in  $n$ -excitation subspaces with individual Hamiltonians in the form

$$\begin{aligned} \hat{H}_n = & n\hbar\omega_c 1_n - \hbar\Delta |e, n-1\rangle \langle e, n-1| \\ & + \hbar g\sqrt{n} (|g, n\rangle \langle e, n-1| + |e, n-1\rangle \langle g, n|). \end{aligned} \quad (2.4)$$

In the  $n = 0$  excitation regime the eigenstate has the form

$$|0\rangle = |g, 0\rangle \text{ with energy } E_0 = 0. \quad (2.5)$$

For  $n > 0$  the eigenstates are the so-called dressed states of the coupled system. By defining  $\tan \theta = g\sqrt{n}/\Delta$  the states can be parametrized with the mixing angle  $\theta$ :

$$|+, n\rangle = \cos \frac{\theta}{2} |g, n\rangle + \sin \frac{\theta}{2} |e, n-1\rangle \quad (2.6a)$$

$$|-, n\rangle = -\sin \frac{\theta}{2} |g, n\rangle + \cos \frac{\theta}{2} |e, n-1\rangle, \quad (2.6b)$$

with eigenenergies

$$E_{\pm, n} = n\hbar\omega_c - \frac{1}{2}\hbar\Delta \pm \hbar\sqrt{\Delta^2 + g^2n}. \quad (2.7)$$

In the limit where  $|\Delta| \ll g$  the bare states  $|g, n\rangle$  and  $|e, n-1\rangle$  are strongly coupled and split into two normal modes, separated by  $\Omega_n = 2g\sqrt{n}$ . These so-called polariton modes are a superposition of photonic and atomic excitations in the system.

### Dispersive Limit

The regime of large detuning where  $g \ll |\Delta|$  is of special interest because it allows for so called quantum nondemolition measurements [58–62]. The Hamiltonian can be diagonalized approximately by a unitary Schrieffer-Wolff transformation [63–65] in the form

$$\tilde{H} = \hat{D}^\dagger \hat{H}_{JC} \hat{D} \quad (2.8)$$

with the unitary transformation

$$\hat{D} = e^{\lambda \hat{X}_-}. \quad (2.9)$$

Here  $\lambda$  represents a small parameter and hence, Equation (2.8) can be expanded in powers of  $\lambda$  with the Baker-Campbell-Hausdorff formula:

$$\tilde{H} = \hat{H}_{JC} + \lambda [\hat{H}_{JC}, \hat{X}_-] + \frac{1}{2} \lambda^2 [[\hat{H}_{JC}, \hat{X}_-], \hat{X}_-] + \dots \quad (2.10)$$

By demanding that the operator  $\hat{X}_-$  satisfies the condition

$$[\hat{H}_0, \hat{X}_-] = \hat{H}_{int}, \quad (2.11)$$

the coupling term vanishes. As  $\lambda \hat{X}_- \sim \mathcal{O}(g)$  one retrieves the following representation of the Hamiltonian:

$$\tilde{H} = \hat{H}_0 + \frac{\lambda}{2} [\hat{H}_{int}, \hat{X}_-] + \mathcal{O}(g^3). \quad (2.12)$$

For the JC model the suitable choice is  $\lambda = g/\Delta$  with the operator

$$\hat{X}_- = \hat{\sigma}_- \hat{a}^\dagger - \hat{\sigma}_+ \hat{a}. \quad (2.13)$$

Applying the transformation leads to the diagonalized Hamiltonian

$$\tilde{H} = \hbar \left( \omega_c - \frac{g^2}{\Delta} \hat{\sigma}_z \right) \hat{a}^\dagger \hat{a} + \hbar \left( \omega_s - \frac{g^2}{\Delta} \right) |e\rangle \langle e|. \quad (2.14)$$

Here the atomic transition frequency is modified by  $g^2/\Delta$  and the photon number is coupled to the atomic population. Hence, the transition frequency of the atom depends on the number of cavity photons and the cavity resonance experiences a shift of  $\pm g^2/\Delta$ , depending on the state the atom. This implies that it is possible to determine the state of the atom by inferring the resonance of the cavity - a useful tool for quasi non-perturbative measurements.

### 2.1.1. Generalized 3-level Jaynes-Cummings Model

The three-level NV system introduced in Chapter 1 can often be projected into a two-level sub-space. This then enables to use the standard Jaynes-Cummings model as a proper description for the system. This is valid if the energy separation between the  $m_s = \pm 1$  surpasses the coupling strength to the cavity mode by far. However, in the limit of zero field, the upper spin states in the Hamiltonian displayed in Equation (1.7) are degenerate and the JC Hamiltonian has to be modified to provide an accurate description of the system [66].

In the following part, a single three-level system with degenerate excited levels, coupled to a single mode of radiation is considered. The three-level system is illustrated in Figure 2.3 where two transitions from the common ground state  $|g\rangle$  to an intermediate state  $|i\rangle$  and an excited state  $|e\rangle$  are coupled to a single mode of radiation.

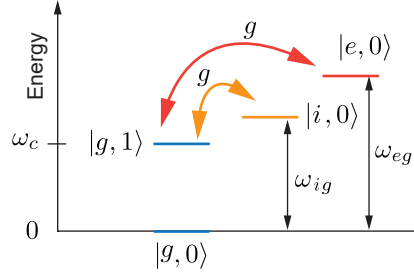


**Figure 2.3.:** Energy level diagram of a generalized three-level JC system. Bare states of a three-level system and the field mode. The intermediate state  $|i\rangle$  and the excited state  $|e\rangle$  are coupled to the field mode with the rate  $g$ . The illustration is limited to the single excitation regime.

A Hamiltonian describing such a system has the form

$$\hat{H}_{3\text{JC}} = \overbrace{\hbar\omega_c a^\dagger a + \hbar\omega_{eg} |e\rangle \langle e| + \hbar\omega_{ig} |i\rangle \langle i|}^{\hat{H}_0} + \overbrace{\hbar g(\hat{a}^\dagger |g\rangle \langle e| + |e\rangle \langle g| \hat{a}) + \hbar g(\hat{a}^\dagger |g\rangle \langle i| + |i\rangle \langle g| \hat{a})}^{\hat{H}_{\text{int}}} \quad (2.15)$$

Here again  $H_0$  gives the unperturbed energies of the atomic and photonic states

$$\begin{aligned} \hat{H}_0 |g, n\rangle &= n\hbar\omega_c |g, n\rangle, \\ \hat{H}_0 |i, n-1\rangle &= (n\hbar\omega_c - \hbar\Delta_1) |i, n-1\rangle, \text{ and} \\ \hat{H}_0 |e, n-1\rangle &= (n\hbar\omega_c - \hbar\Delta_2) |e, n-1\rangle, \end{aligned} \quad (2.16)$$

## 2. Light Matter Interaction

---

where the definitions  $\Delta_1 := \omega_c - \omega_{ig}$  and  $\Delta_2 := \omega_c - \omega_{eg}$  have been used. The energy levels are coupled via the interaction part of the Hamiltonian,

$$\begin{aligned}\hat{H}_{\text{int}} |g, n\rangle &= g\sqrt{n}(|e, n-1\rangle + |i, n-1\rangle), \\ \hat{H}_{\text{int}} |i, n-1\rangle &= g\sqrt{n}|g, n\rangle, \text{ and} \\ \hat{H}_{\text{int}} |e, n-1\rangle &= g\sqrt{n}|g, n\rangle.\end{aligned}\tag{2.17}$$

The Hamiltonian again conserves the number of excitations in the system but now couples the states in the three-dimensional subspace spanned by  $\{|g, n\rangle, |e, n-1\rangle, |i, n-1\rangle\}$  with the strength  $g\sqrt{n}$ . In this  $n$ -excitation subspace the Hamiltonian can be written in the form

$$\begin{aligned}\hat{H}_{n-3JC} &= n\hbar\omega_c 1_n - \hbar\Delta_1 |i, n-1\rangle \langle i, n-1| - \hbar\Delta_2 |e, n-1\rangle \langle e, n-1| \\ &\quad + \hbar g\sqrt{n}(|g, n\rangle \langle i, n-1| + |i, n-1\rangle \langle g, n|) \\ &\quad + \hbar g\sqrt{n}(|g, n\rangle \langle e, n-1| + |e, n-1\rangle \langle g, n|)\end{aligned}\tag{2.18}$$

For  $n = 0$  the eigenstate is  $|0\rangle = |g, 0\rangle$  with  $E_0 = 0$ . With  $n > 0$ , the diagonalization of the Hamiltonian leads to three different eigenenergies. However, in the case of  $\Delta_1 \neq \Delta_2$  the solution is given by the cubic formula to solve the polynomial of degree three. The problem simplifies if the condition  $\Delta_1 = \Delta_2 \equiv \Delta$  (the levels  $|i\rangle$  and  $|e\rangle$  are degenerate) is satisfied and the eigenenergies become:

$$E_{\pm, n} = n\hbar\omega_c - \hbar\frac{1}{2}\Delta \pm \hbar\frac{1}{2}\sqrt{8g^2n + \Delta^2}, \text{ and}\tag{2.19a}$$

$$E_A = n\hbar\omega_c + \hbar\Delta.\tag{2.19b}$$

The corresponding eigenvectors have the form

$$|+, n\rangle = \alpha \left[ \frac{-\Delta + \sqrt{8g^2n + \Delta^2}}{2g\sqrt{n}} |g, n\rangle + |i, n-1\rangle + |e, n-1\rangle \right],\tag{2.20a}$$

$$|A, n\rangle = \frac{1}{\sqrt{2}} [-|i, n-1\rangle + |e, n-1\rangle], \text{ and}\tag{2.20b}$$

$$|-, n\rangle = \alpha \left[ \frac{-\Delta - \sqrt{8g^2n + \Delta^2}}{2g\sqrt{n}} |g, n\rangle + |i, n-1\rangle + |e, n-1\rangle \right],\tag{2.20c}$$

with normalization constant  $1/\alpha = \frac{1}{2}\sqrt{8 + \frac{(\Delta + \sqrt{8g^2n + \Delta^2})^2}{g^2n}}$ .

For  $|\Delta| \ll g$  the system couples strongly with two bright states and one dark state,  $|A, n\rangle$ , emerging. The term 'dark state' refers to the state that forms only by

mixing components from the three-level system but has no component of the field. On resonance the eigenvectors read

$$|+, n\rangle = \frac{1}{2} \left[ \sqrt{2} |g, n\rangle + |i, n-1\rangle + |e, n-1\rangle \right], \quad (2.21a)$$

$$|A, n\rangle = \frac{1}{\sqrt{2}} \left[ -|i, n-1\rangle + |e, n-1\rangle \right], \text{ and} \quad (2.21b)$$

$$|-, n\rangle = \frac{1}{2} \left[ -\sqrt{2} |g, n\rangle + |i, n-1\rangle + |e, n-1\rangle \right], \quad (2.21c)$$

with the corresponding eigenenergies

$$E_{\pm, n} = n\hbar\omega_c \pm \hbar\sqrt{2}g\sqrt{n}, \quad (2.22a)$$

$$E_{i, e} = n\hbar\omega_c. \quad (2.22b)$$

By comparing these results to the ones obtained from the two-level Jaynes-Cummings in the previous section (Equation (2.7) and Equation (2.6a)), one can conjecture the following:

- If the excited levels of the atom are degenerate, the interaction part of the Hamiltonian mixes these levels and the degree of degeneracy is reduced by one.
- Only the symmetric superposition ( $|i, n-1\rangle + |e, n-1\rangle$ ) couples to the radiation field
- The antisymmetric superposition ( $-|i, n-1\rangle + |e, n-1\rangle$ ) forms a dark state  $|A, n\rangle$  which does not couple to the radiation field and experiences no energy shift with respect to the before degenerate states ( $|i, n-1\rangle$  and  $|e, n-1\rangle$ )
- The coupling to the radiation mode is enhanced by a factor  $\sqrt{2}$  because of the additional level of the atom

### Dispersive Limit

As only the symmetric superposition state couples to the radiation field, the problem can be reduced to the approximate diagonalization of an effective Hamiltonian. The energy of the antisymmetric state  $|A, n-1\rangle$  that is formed by the interaction is not changed with respect to the unperturbed states. The effective Hamiltonian can be built with enhanced coupling strength to the field,  $g \mapsto g' = \sqrt{2}g$ , which accounts

for the two degenerate excited states:

$$\begin{aligned} \hat{H} = n\hbar\omega_c 1_n - \hbar\Delta |D, n-1\rangle \langle D, n-1| \\ + \hbar g' \sqrt{n} (|g, n\rangle \langle D, n-1| + |D, n-1\rangle \langle g, n|), \end{aligned} \quad (2.23)$$

with  $|D, n-1\rangle = |i, n-1\rangle + |e, n-1\rangle$ .

The approximate solution can be found by performing a unitary transformation similar to Equation (2.8) and leads to:

$$\hat{H} = n\hbar(\omega_c - \frac{g'^2}{\Delta}) |D, n-1\rangle \langle D, n-1| + \hbar(\Delta + \frac{g'^2}{\Delta}) |D, n-1\rangle \langle D, n-1|. \quad (2.24)$$

## 2.2. Tavis-Cummings Model

A further generalization of the JC model to  $N$  emitters coupled to a radiation mode is the Tavis-Cummings (TC) model. In the context of quantum optics it describes the collective interaction of an ensemble of  $N$  two level emitters with the quantized electromagnetic field [67–69]. The Hamiltonian has the form

$$\hat{H}_{TC} = \hbar\omega_c \hat{a}^\dagger \hat{a} + \frac{1}{2} \hbar\omega_s \sum_{i=1}^N \hat{\sigma}_z^{(i)} - \hbar \sum_{i=1}^N g_{(i)} (\hat{\sigma}_+^{(i)} \hat{a} + \hat{\sigma}_-^{(i)} \hat{a}^\dagger) \quad (2.25)$$

For the physical findings covered in this thesis it is useful to define super-operators for collective excitations in the ensemble with a giant spin  $\hat{\mathbf{S}} = (\hat{S}_x, \hat{S}_y, \hat{S}_z)^T$ :

$$\hat{S}_z = \sum_{i=1}^N \hat{\sigma}_z^{(i)}, \quad \hat{S}^\pm = \sum_{i=1}^N \hat{\sigma}_\pm^{(i)}. \quad (2.26)$$

The operators satisfy the commutation relations:

$$[\hat{S}^\pm, \hat{S}^\mp] = \pm 2\hat{S}_z, \quad [\hat{S}_z, \hat{S}^\pm] = \pm \hat{S}^\pm. \quad (2.27)$$

With this definitions it is possible to rewrite the Hamiltonian with the use of the collective operators in the form

$$\hat{H} = \hbar\omega_c \hat{a}^\dagger \hat{a} + N \frac{\hbar\omega_s \hat{S}_z}{2} - \hbar g_0 (\hat{S}^+ \hat{a} + \hat{S}^- \hat{a}^\dagger) \quad (2.28)$$

if it is assumed that all spins couple with the same coupling rate  $g_0$ , the collective coupling strength is enhanced by the square-root of the number of emitters,  $\Omega = \sqrt{g_1^2 + g_2^2 + \dots} = g_0 \sqrt{N}$  (assuming homogeneous single spin coupling strength). As

the free parts of the Hamiltonian commutes with the interaction part, the eigenstates of the system can be written as an superposition of collective ensemble Dicke states and cavity photon number (Fock) states. For the operators  $\hat{\mathbf{S}}^2$  and  $\hat{S}_z$  the eigenstates are Dicke states in the form  $|j, m\rangle$ .

As the free part of the Hamiltonian and the interaction part are commuting, a suitable basis for the eigenstates of this Hamiltonian consists of cavity photon states  $|n\rangle$  and states  $|j, m\rangle$  of the giant  $N/2$  spin. Therefore, the eigenvalues to the operator eigenstates are given by

$$\hat{S}^2 |j, m\rangle = (j(j+1)) |j, m\rangle, \quad \hat{S}_z |j, m\rangle = 2m |j, m\rangle, \quad \hat{a}^\dagger \hat{a} |n\rangle = n |n\rangle. \quad (2.29)$$

The full eigenstates can be constructed from a superposition of the free part eigenstates weighted with the coefficients  $A_n^{(j,c,i)}$ :

$$|j, c, i\rangle = \sum_{n=c-j}^{c+j} A_n^{(j,c,i)} |n\rangle |j, c-n\rangle. \quad (2.30)$$

The label  $i$  of the states is to distinguish between states that are identical in terms of  $j$  and  $c$ . All eigenstates can be written with  $j$  and  $c = n + m$  where  $n$  is the number of cavity photons and  $m$  corresponds to half of the  $J_z$  operator eigenvalue and  $-j \leq c < \infty$ . The eigenstates are dressed states of a spin  $N/2$  system. Limiting the discussion to the  $n = 1$  single excitation regime,  $c = -j + 1$ , the eigenvectors have the form

$$|j, 1, \pm\rangle = \frac{1}{\sqrt{2}} (|1\rangle |j, m = -j\rangle \pm |0\rangle |j, m = j\rangle) \quad (2.31)$$

with their eigenenergies

$$E_{\pm} = \hbar\omega_c \pm \hbar \overbrace{\sqrt{N}}^{\Omega} g_0. \quad (2.32)$$

Writing the angular momentum eigenstates of Equation (2.31) explicitly in the N emitter basis they read

$$|j, m = -j\rangle = |g, \dots, g\rangle, \quad |j, m = -j + 1\rangle = \frac{1}{\sqrt{N}} \sum_{i=1}^N |g, \dots, e_i, \dots, g\rangle. \quad (2.33)$$

### Dispersive Regime

The dispersive regime is given similarly to the previously discussed JC model: The detuning is much larger than the collective coupling strength  $\Omega \ll |\omega_c - \omega_s|$  [63]. The Hamiltonian in Equation (2.28) can be moved to the dispersive regime by the unitary



## 2. Light Matter Interaction

---

transformation

$$\hat{U} = e^{\lambda \hat{X}_-}. \quad (2.34)$$

In the transformation the operator  $\hat{X}_- = \hat{S}_- \hat{a}^\dagger - \hat{S}_+ \hat{a}$  has been used and  $\lambda = \Omega/\Delta$  presents a small parameter. In terms of the collective operators the result is similar to the JC model in Section 2.1:

$$H_{\text{disp}} = \left( \omega_s + \frac{\Omega^2}{\Delta} \right) \hat{S}_z + \left( \omega_c + \frac{2\Omega^2}{\Delta} \hat{S}_z \right) \hat{a}^\dagger \hat{a}. \quad (2.35)$$

### 3. Confined Electromagnetic Fields - Cavities and Resonators

The previous chapter used the harmonic oscillator mode just within the description in the second quantization of quantum mechanics. In that sense it was a rather generic object. Here the harmonic oscillator mode is introduced as a mode of the electromagnetic field. Therefore, Maxwell's equations act as a starting point from which a wave equation for the electric and magnetic field can be derived:

$$\nabla^2 \mathbf{E} - \frac{1}{c^2} \frac{\partial^2}{\partial t^2} \mathbf{E} = 0, \quad (3.1)$$

$$\nabla^2 \mathbf{B} - \frac{1}{c^2} \frac{\partial^2}{\partial t^2} \mathbf{B} = 0. \quad (3.2)$$

With periodic boundary conditions one finds wave solutions for both fields:

$$\mathbf{B}(\mathbf{r}, t) = -i \sum_m \sqrt{\frac{\mu_0 \hbar \omega_m}{2V_{\text{mode}}}} \mathbf{e}_m \times \mathbf{k}_m \left\{ a_m \exp [i (\mathbf{k}_m \mathbf{r} - \omega_m t)] + a_m^\dagger \exp [-i (\mathbf{k}_m \mathbf{r} - \omega_m t)] \right\} \quad (3.3)$$

$$\mathbf{E}(\mathbf{r}, t) = i \sum_m \sqrt{\frac{\hbar \omega_m}{2\epsilon_0 V_{\text{mode}}}} \mathbf{e}_m \times \mathbf{k}_m \left\{ a_m \exp [i (\mathbf{k}_m \mathbf{r} - \omega_m t)] + a_m^\dagger \exp [-i (\mathbf{k}_m \mathbf{r} - \omega_m t)] \right\}, \quad (3.4)$$

where the index  $m$  sums over all modes and polarization directions. If in addition a coulomb gauge for the vector potential is demanded, the resulting modes for  $\mathbf{B}$  and  $\mathbf{E}$  satisfy the transversality condition  $\mathbf{e}_m \times \mathbf{k}_m = 0$ . This gives two orthogonal polarization directions perpendicular to the direction of propagation  $\mathbf{k}_m$ .

The total energy then is given by an integration over the whole mode volume:

$$\begin{aligned} H &= \frac{1}{2} \int_{V_{\text{mode}}} \left( \epsilon_0 \mathbf{E}^2 + \frac{1}{\mu_0} \mathbf{B}^2 \right) dv \\ &= \sum_m \hbar \omega_m \left( a_m a_m^\dagger + a_m^\dagger a_m \right). \end{aligned} \quad (3.5)$$

The creation and annihilation operators  $a_m$  and  $a_m^\dagger$  satisfy the standard bosonic commutation relations and can be related to the generalized coordinate  $q$  and momentum  $p$ :

$$a_m = \frac{1}{\sqrt{2\hbar\omega_m}}(\omega q + ip), \quad (3.6)$$

$$a_m^\dagger = \frac{1}{\sqrt{2\hbar\omega_m}}(\omega q - ip). \quad (3.7)$$

### 3.1. Cavity Input-Output Formalism

To implement a Jaynes-Cummings or Tavis-Cummings like Hamiltonian, only a single mode of the electromagnetic field is used. Hence the index of the mode  $m$  is dropped and the cavity mode is described with the Hamiltonian of a harmonic oscillator:

$$H = \hbar\omega_c(\hat{a}^\dagger\hat{a} + \frac{1}{2}). \quad (3.8)$$

In Figure 3.1 such a cavity consisting of two mirrors and the associated fields is illustrated. Each mirror can act as an input or an output for electromagnetic radiation. The transparency of the mirrors is given by their loss rate  $\kappa_1$  and  $\kappa_2$  respectively. The rate  $\kappa_I$  accounts for damping by interaction with an internal bath.

In the following part an expression for the transmission through the cavity will be derived within the cavity input-output formalism [70]. The Heisenberg equation of motion for the intra cavity field  $a(t)$  can be written as

$$\frac{d\hat{a}(t)}{dt} = -\frac{i}{\hbar} [\hat{a}(t), \hat{H}] - (\kappa_1 + \kappa_2 + \kappa_I)\hat{a}(t) + \sqrt{2\kappa_1}\hat{a}_{\text{IN}}(t) + \sqrt{2\kappa_2}\hat{b}_{\text{IN}}(t). \quad (3.9)$$

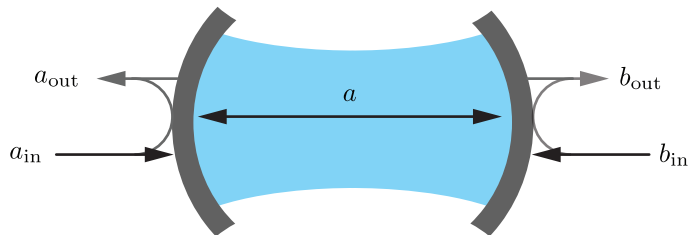


**Figure 3.1.: Schematic representation of the cavity fields.** The illustration shows a two-sided cavity with the input fields  $a_{\text{in}}$  and  $b_{\text{in}}$ . The output fields are denoted by  $a_{\text{out}}$  and  $b_{\text{out}}$ . The intra cavity field has the symbol  $a$ .

The Fourier components of the field in the cavity are defined as

$$\hat{a}(t) = \frac{1}{2\pi} \int_{-\infty}^{\infty} e^{-i\omega(t-t_0)} \hat{a}(\omega) d\omega. \quad (3.10)$$

Hence, with the following expression the input fields can be linked to the intra-cavity field as

$$\hat{\mathbf{a}}(\omega) = \frac{\sqrt{2\kappa_1} \hat{\mathbf{a}}_{\text{IN}}(\omega) + \sqrt{2\kappa_2} \hat{\mathbf{b}}_{\text{IN}}(\omega)}{(\kappa_1 + \kappa_2 + \kappa_I) - i(\omega - \omega_c)}. \quad (3.11)$$

Here the frequency component vector

$$\hat{\mathbf{a}}(\omega) = \begin{bmatrix} \hat{a}(\omega) \\ \hat{a}^\dagger(\omega) \end{bmatrix} \quad (3.12)$$

was used, with  $a^\dagger(\omega)$  as the Fourier transform of  $a^\dagger(t)$ . A relation between the input and output can be found by introducing the following boundary conditions,

$$\hat{a}_{\text{OUT}}(t) + \hat{a}_{\text{IN}}(t) = \sqrt{2\kappa_1} \hat{a}(t), \quad (3.13a)$$

$$\hat{b}_{\text{OUT}}(t) + \hat{b}_{\text{IN}}(t) = \sqrt{2\kappa_2} \hat{a}(t). \quad (3.13b)$$

Next, a solution for the output field is found to be

$$\hat{b}_{\text{OUT}}(\omega) = \frac{2\sqrt{\kappa_1\kappa_2} \hat{a}_{\text{IN}} + [\kappa_2 - \kappa_1 - \kappa_I + i(\omega - \omega_c)] \hat{b}_{\text{IN}}}{\kappa_1 + \kappa_2 + \kappa_I - i(\omega - \omega_c)}. \quad (3.14)$$

The squared magnitude of the transmission through the cavity with an input field  $a_{\text{IN}}$  and  $b_{\text{IN}} = 0$  then has the form

$$|T|^2 = \left| \frac{\hat{b}_{\text{OUT}}}{\hat{a}_{\text{IN}}} \right|^2 = \frac{4\kappa_1\kappa_2}{(\omega - \omega_c)^2 + (\kappa_1 + \kappa_2 + \kappa_I)^2}. \quad (3.15)$$

In the case of equally reflecting mirrors ( $\kappa_1 = \kappa_2 = \kappa_{\text{ext}}/2$  and  $\kappa_{\text{tot}} = \kappa_{\text{ext}} + \kappa_I$ ) this simplifies to

$$|T|^2 = \left| \frac{\hat{b}_{\text{OUT}}}{\hat{a}_{\text{IN}}} \right|^2 = \frac{\kappa_{\text{ext}}^2}{(\omega - \omega_c)^2 + \kappa_{\text{tot}}^2}. \quad (3.16)$$

This expression represents a Lorentzian line shape for the squared cavity transmission. In the presented experiments, probing the cavity is the only way to infer the state of the system and makes the squared cavity transmission amplitude the most important measurable quantity throughout this work.

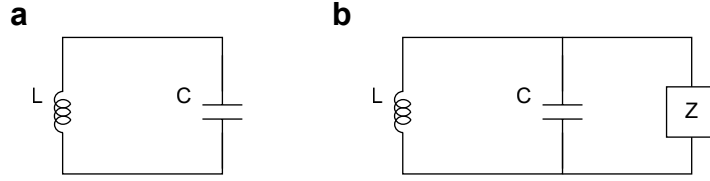


**Figure 3.2.: LC resonant circuit.** **a**, Circuit consisting of an inductor  $L$  and a capacitance  $C$ . **b**, Resonant circuit connected with the environment represented by the external impedance  $Z$  in parallel with the circuit.

## 3.2. LC Oscillator - Classical to Quantum

In the previous section the transmission through a cavity was discussed in terms of the input-output formalism. Here the 'cavity' is given by an LC circuit as a harmonic oscillator. In Figure 3.2 such a circuit consisting of an inductance  $L$  and a capacitance  $C$  is displayed. With the nowadays available nano-fabrication technologies, values for the inductance and capacitance of  $L = 10$  nH and  $C = 1$  pF are easily achievable. The resulting resonance of  $\omega_c/2\pi = 1/2\pi\sqrt{LC} \simeq 1.6$  GHz corresponds to the microwave domain. Devices with these parameters are easily achievable with geometries much smaller than the associated wavelength - the circuit is said to be in the lumped limit.

The flux  $\Phi$  in the inductor can be considered to be the only collective degree of freedom of the system. In comparison to the classical spring-mass oscillator,  $\Phi$  corresponds to the position of mass and the charge  $q$  on the capacitor represents the momentum. Therefore, the variables  $q$  and  $\Phi$  are conjugate variables in the sense of Hamiltonian mechanics.

Operating such a circuit at low temperatures, one can ensure that the thermal fluctuation energy is much smaller than the energy associated with the resonant frequency,  $k_B T \ll \hbar\omega_c$ . Satisfying this condition, however, is not sufficient to justify a treatment of  $\Phi$  as quantum variable. Additionally, the separation of the energy levels must exceed their width.

To perform the transition from a classical LC oscillator to a quantum description the Hamilton function is replaced by operators which fulfil the commutation relation  $[\hat{\Phi}, \hat{q}] = i\hbar$ . The Hamiltonian for the circuit in Figure 3.2 then reads

$$\hat{H} = \frac{\hat{q}^2}{2C} + \frac{\hat{\Phi}^2}{2L}. \quad (3.17)$$

With the use of the usual creation and annihilation operators for bosonic modes the

conjugate variables can be expressed as

$$\hat{\Phi} = \sqrt{\frac{\hbar Z_0}{2}} (\hat{a} + \hat{a}^\dagger), \quad (3.18a)$$

$$\hat{q} = \frac{1}{i} \sqrt{\frac{\hbar}{2Z_0}} (\hat{a} - \hat{a}^\dagger), \text{ and.} \quad (3.18b)$$

In these expressions  $Z_0 = \frac{L}{C}$  as the circuit impedance has been used.

Finally one again retrieves the Hamiltonian of the quantum harmonic oscillator:

$$\hat{H} = \frac{\hbar\omega_c}{2} (\hat{a}^\dagger \hat{a} + \hat{a} \hat{a}^\dagger) = \hbar\omega_c \left( \hat{a}^\dagger \hat{a} + \frac{1}{2} \right) \quad (3.19)$$

### Classical Parallel RLC Rsonant Circuit

The previous discussion treated the LC circuit as a quantum mechanical harmonic oscillator without any dissipation. In real life experimental situations, however, losses are unavoidable and, therefore, a brief review of the classical RLC resonator is given here. RLC circuits can be implemented in various ways, as distributed elements such as transmission or microstrip lines, rectangular and circular shaped waveguides or as dielectric resonators [71]. In Figure 3.3 a parallel RLC resonant circuit is shown with its input impedance

$$Z_{in} = \left( \frac{1}{R} + \frac{1}{j\omega L} + j\omega C \right)^{-1}. \quad (3.20)$$

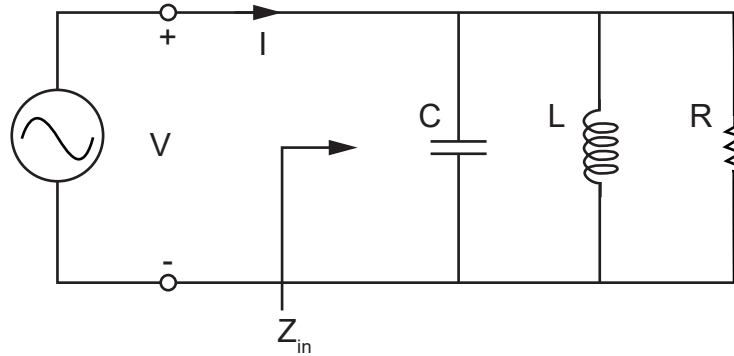


**Figure 3.3.: Parallel RLC resonant circuit.** The figure shows the circuit diagram of a classical RLC parallel resonator with input impedance  $Z_{in}$ .

The average energy stored in the capacitor and inductor is given by  $W_e = \frac{1}{4}|V|^2 C$  and  $W_m = \frac{1}{4}|I_L|^2 L = \frac{1}{4}|V|^2 \frac{1}{\omega_c^2 L}$  respectively. Together with the dissipated power of the

circuit,  $P_{\text{loss}} = \frac{1}{2} \frac{|V|^2}{R}$ , the quality factor  $Q$  of the resonator can be defined as

$$Q = \omega \frac{\text{average energy stored}}{\text{energy loss/second}} = \omega \frac{W_m + W_e}{P_{\text{loss}}}. \quad (3.21)$$

Resonance will occur when the stored magnetic and electric energy are equal,  $W_m = W_e$ , hence, the impedance becomes purely real valued,  $Z_{\text{in}} = \frac{P_{\text{loss}}}{\frac{1}{2}|I|^2} = R$ . From this directly follows that the resonance is given by  $\omega_c = \frac{1}{\sqrt{LC}}$ . The unloaded quality factor then can be expressed as

$$Q_0 = \omega_0 \frac{2W_m}{P_{\text{loss}}} = \frac{R}{\omega_0 L} = \omega_0 RC. \quad (3.22)$$

The unavoidable coupling of the resonator to some external circuitry has the effect of lowering the overall  $Q$  value. An external load can be modelled as a resistor  $R_L$  in parallel to the RLC resonant circuit. As a result, the effective resistance then becomes  $RR_L/(R + R_L)$ . with the definition  $Q_e = \frac{R_L}{\omega_c L}$ , as an external quality factor, the loaded  $Q$  can be expressed as

$$\frac{1}{Q_L} = \frac{1}{Q_e} + \frac{1}{Q_0}. \quad (3.23)$$

A measure for how strongly the resonator is coupled to external circuitry with its impedance  $Z_0$  is given by the coupling coefficient,

$$g = \frac{Q_0}{Q_e} = \frac{\kappa_{\text{ext}}}{\kappa_I}. \quad (3.24)$$

Depending on the coupling coefficient  $g$ , three different regimes can be distinguished:

1.  $g < 1$ : The link to the external circuit is weak - the resonator is said to be *undercoupled*. The overall quality factor is dominated by the internal losses, the squared transmission is given by  $|T|^2 < 1/4$ . (An expression for the transmission through the cavity has been derived already in Section 3.1)
2.  $g = 1$ : The resonator is critically coupled. The internal and coupling losses are equal and  $|T|^2 = 1/4$ .
3.  $g > 1$ : The link to the external circuit is strong - the resonator is said to be *overcoupled*. The overall quality factor is dominated by coupling losses to the external circuitry and the squared transmission approaches unity:  $|T|^2 \rightarrow 1$ .

**Part II.**

**Experimental Implementation and  
Techniques**



## 4. Microwave Resonators

The experiments presented in this thesis use two conceptually different implementations of a microwave resonator. The main purpose of these resonators is to facilitate coupling to ensembles of nitrogen vacancy centres in diamond. Thus, an important aspect is the mode volume of the oscillating magnetic field in the cavity since this determines the coupling strength of a single emitter to the mode. Each of the presented resonators have a distinct geometry and present different strengths and weaknesses. The choice of resonator depends on the conducted experiment.

### 4.1. Coplanar Waveguide Resonator

This type of resonator consists of a piece of planar transmission line made out of a conducting track on a dielectric substrate. Ground planes are on each side of the track and on the back of the substrate. The electromagnetic field along this track is partly travelling in the dielectric substrate and partly above it. This means the field is emerged in an inhomogeneous medium where the propagation velocity has a spatial dependence. Hence, a coplanar waveguide (CPW) does not support a true transverse electromagnetic (TEM) mode as there will be field components along the longitudinal direction.

Resonators based on that CPWs play a major role in coupling solid state spin systems or superconducting qubits to microwave photons [59]. Even the whole research field of circuit quantum electrodynamics (cQED) [63, 72] was initiated by this type of resonator as they allow confinement of the electromagnetic field to a small mode volume (smaller than the wavelength cubed) with low photon losses (quality factors of up to  $1 \times 10^6$  at the single photon level [73]).

In Figure 4.1 the design of a CPW resonator of certain length and the implementation of the coupling capacitance is illustrated. Set by these boundary conditions a standing electromagnetic wave is created along the central transmission line. Hence, this resonator type only supports integer multiples of the fundamental mode  $k = n\pi/l$  with angular frequency  $\omega = kc$ .

The resonators used within this work have been manufactured by means of optical

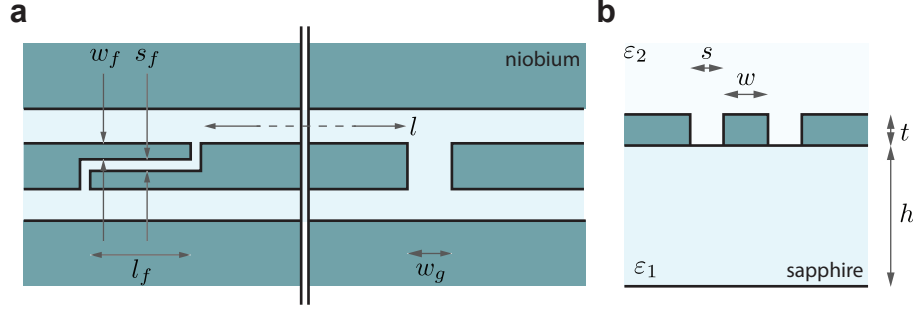


**Figure 4.1.: Coplanar waveguide resonator.** **a**, Top view of the resonator. The coupling of such a cavity can be realized either by so-called finger (left-hand side) or gap capacitors (right-hand side). The niobium metallization is structured by methods of optical lithography onto a sapphire wafer. **b**, Cross section of the resonator. The electromagnetic wave propagating through the resonator is partly emerged in the sapphire substrate (dielectric constant  $\varepsilon_1$ ) and in vacuum ( $\varepsilon_2 \equiv \varepsilon_0$ ). Illustration similar to ref. [74].

lithography. The starting point is a  $300\ \mu\text{m}$  sapphire wafer with a sputtered,  $200\ \text{nm}$  thick thin film of niobium on top. Typical design parameters are  $w = 20\ \mu\text{m}$  for the centre conductor and  $s = 8.3\ \mu\text{m}$  separation to the ground planes. In Figure 4.1 the schematics of the resonator is illustrated with its characteristic design parameters.

The length of the transmission line can be associated with the wavelength of the radiation. Hence, the transmission line resonator is a distributed device, where voltages and currents have varying magnitude and phase throughout its length. Capacitance and inductance of the circuit are defined per unit length and can be derived by conformal mapping techniques [75] or finite element simulations. For the used design, values of  $L_l \sim 0.4\ \mu\text{H}$  and  $C_l \sim 150\ \text{pF}$  are found, which results in a characteristic impedance of  $Z_0 = \sqrt{L_l/C_l} \approx 50\ \Omega$  [76] and a phase velocity  $v_{\text{ph}} = 1/\sqrt{C_l L_l}$ . With the attenuation constant  $\alpha$  and phase constant  $\beta = \omega_n/v_{\text{ph}}$  [74] the frequency-dependent impedance of the transmission line can be expressed as

$$Z_{\text{TL}} \approx \frac{Z_0}{\alpha l + i \frac{\pi}{\omega_0} (\omega - \omega_n)}. \quad (4.1)$$

This approximation is only valid close to resonance of the  $n$ -th mode and for small losses ( $\alpha l \ll 1$ ). The angular frequency then is given by

$$\omega_n = n\omega_0 = \frac{1}{\sqrt{L_n C}}, \quad (4.2)$$

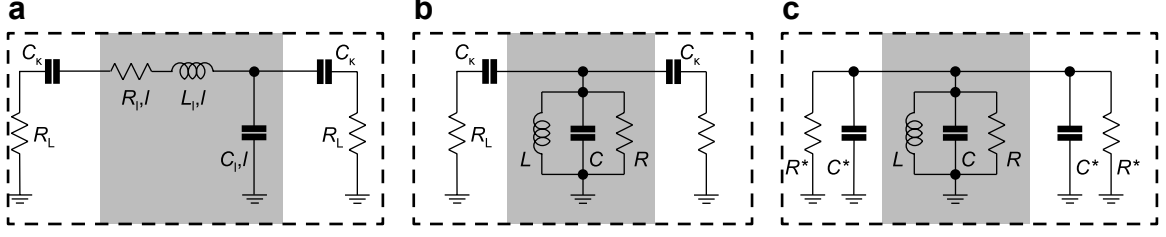


**Figure 4.2.: Circuit diagrams of a coplanar waveguide resonator.** **a**, Transmission line resonator represented with distributed elements. **b**, Transmission line resonator as parallel RLC resonator. **c**, Norton equivalent circuit of the resonator. Illustration similar to ref. [74].

with the characteristic parameters

$$L_n = \frac{2L_l l}{n^2 \pi^2}, \quad C = \frac{C_l l}{2}, \quad \text{and} \quad R = \frac{Z_0}{\alpha l}. \quad (4.3)$$

To have an intuitive approach to the effects of coupling the transmission line resonator to a feed line the impedance can be approximated by those of an equivalent lumped element parallel LCR resonator with

$$Z_{\text{LCR}} = \left( \frac{1}{i\omega L_n} + i\omega C + \frac{1}{R} \right)^{-1} \approx \frac{R}{1 + 2iRC(\omega - \omega_n)}. \quad (4.4)$$

As already discussed in Section 3.2 the overall quality factor  $Q_L$  will be lowered through resistive loading by coupling the resonator to a feed line. Furthermore, the resonator will experience a frequency shift due to an additional capacitive loading.

In Figure 4.2 the transformation of the series connection of the load resistor  $R_l L$  and coupling capacitors  $C_k$  into a parallel Norton equivalent circuit are shown, with

$$R^* = \frac{1 + \omega_n^2 C_\kappa^2 R_L^2}{\omega_n^2 C_\kappa^2 R_L}, \quad \text{and} \quad (4.5a)$$

$$C^* = \frac{C_\kappa}{1 + \omega_n^2 C_\kappa^2 R_L^2}. \quad (4.5b)$$

Through the small coupling capacitances the load resistance  $R_L = 50 \Omega$  transforms to a large impedance  $R^* = R_L/k^2$  with  $k = \omega_n C_k R_L \ll 1$ . In the case of input and output coupling  $C_k$ , the quality factor  $Q_L$  reads

$$Q_L = \omega_n^* \frac{C + 2C^*}{1/R + 2/R^*} \approx \omega_n \frac{C}{1/R + 2/R^*}, \quad (4.6)$$

which represents a parallel combination of  $R$  and  $R^*/2$ . The shift in the resonance frequency is given by the loading due to a parallel combination of the resonator capacitance  $C$  and  $C^*$ . The shifted resonance is then given by

$$\omega_n^* = \frac{1}{\sqrt{L_n(C + 2C^*)}}. \quad (4.7)$$

If the coupling capacitances are rather small,  $C + 2C^* \approx C$ , the quality factor  $Q_L$  can be expressed as given in Equation (3.23) with

$$Q_0 = \omega_n RC = \frac{n\pi}{2\alpha l}, \quad Q_e = \frac{\omega_n R^* C}{2}. \quad (4.8)$$

As already derived in previous chapters, the transmitted intensity  $|A|^2$  has a Lorentzian line shape with the quality factor given by internal and coupling losses. In the experiment these parameters can be determined by transmission spectroscopy in an autodyne detection scheme.

### Electromagnetic Field of a Coplanar Waveguide

The amplitude of the electromagnetic field generated by a resonator together with the dipole moment of an emitter determines their interaction strength. Vacuum fluctuations of the field exist for the electric and magnetic field respectively, with amplitudes given due to half a photon. As an example, the energy stored in the magnetic field is given by [77, 78]

$$\frac{\hbar\omega_c}{4} = \frac{1}{2\mu_0} \int B^2 dV = \frac{B_0^2 V_{\text{mode}}}{2\mu_0}, \quad (4.9)$$

where  $V$  denotes the mode volume and  $\mu_0$  the vacuum permeability. The amplitude of the vacuum field is then given by

$$B_0 = \sqrt{\frac{\mu_0 \hbar \omega_c}{2V_{\text{mode}}}} \quad (4.10)$$

This expression shows that a decrease in the mode volume results in an increase of the magnetic field strength for a photon of angular frequency  $\omega_c$ . A CPW resonator can confine a photon to dimensions much smaller than the wavelength in the transverse direction. In comparison, the mode volume of a three-dimensional box resonator is usually the size of several wavelengths cubed.

The spatial distribution of the electromagnetic field in a CPW resonator has an analytical solution that can be derived from conformal mappings [79]. Another approach

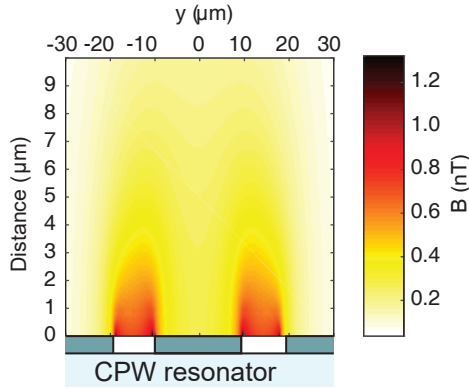


**Figure 4.3.: Spatial dependence of the magnetic field generated by a CPW resonator.** The plot presents the calculated magnetic field amplitude of a coplanar waveguide resonator. The magnetic field is strongest at the gaps and shows a steep gradient in  $z$  direction. This variation in the amplitude results in a broad distribution of coupling rates for an ensemble of emitters placed above the resonator. Image taken from ref. [80].

is a finite element simulation to derive spatial distribution of the field amplitude in the plane perpendicular to the resonator. In Figure 4.3 the magnetic field amplitude is plotted in the plane perpendicular to the resonator. The amplitude has a maximum in the gaps to each of the side ground planes with typical field strengths of 1 nT.

The mode volume can be estimated by taking the variation of the magnetic field amplitude along the longitudinal direction as  $\sim \sin(\frac{\pi y}{L})$ , with  $L$  as the length of the centre conductor. The transverse geometry is roughly given by the width of the gaps ( $\sim 10 \mu\text{m}$  each). With a typical length of 20 mm and a resonance frequency of 3 GHz, this computes to a mode volume of  $V = 1.2 \times 10^{-13} \text{ m}^3$  and a magnetic field amplitude  $B_0 \approx 1 \text{ nT}$ . With the electron magnetic moment  $\mu_e = 14 \text{ MHz/mT}$  to the vacuum Rabi frequency for a single electron spin of  $g_e/2\pi \approx 10 \text{ Hz}$ .

Looking at the spatial distribution of the field one can see that the gradient above the resonator is steep. This implies that the resulting single spin coupling strength has a strong dependence on the position and can vary over orders of magnitude for emitters placed in the field of the resonator.

### Number of Photons in the Resonator

An important parameter for cavity QED experiments is the number of photons circulating in the resonator. It can be determined from the input power applied to the

resonator:

$$n = \frac{P_{\text{res}}}{\hbar\omega_c\kappa}, \quad (4.11)$$

where  $2\kappa = \pi\Delta\nu$  is the full width at half maximum (FWHM) of the resonance. The relation to the quality factor is given through  $2\kappa = \omega_c/Q_L$ . For the case that the input capacitance is different than the output capacitance ( $C_1 \neq C_2$ ), the transmission on resonance  $|S_{21}|^2 \equiv |T|^2$  has to be taken into account:

$$P_{\text{res}} = P_{\text{in}}|S_{21}|^2 = P_{\text{in}} \left( \frac{2}{\frac{C_1}{C_2} + \frac{C_2}{C_1}} \right)^2. \quad (4.12)$$

## 4.2. 3D Lumped Element Resonator

This chapter is dedicated to the design and technical details of the 3D lumped element resonator which is published in the following research work:

- **Collective strong coupling with homogeneous Rabi frequencies using a 3D lumped element microwave resonator**

A. Angerer, **T. Astner**, D. Wirtitsch, H. Sumiya, S. Onoda, J. Isoya, S. Putz, and J. Majer

*Applied Physics Letters* **109**, 033508 (2016)

With the presented single spin coupling rate of a CPW resonator it has been demonstrated that the strong coupling of an ensemble of emitters to the mode is feasible [20, 21, 81–83]. However, the strong spatial dependence of the single spin Rabi frequency makes coherent control and readout of a large ensemble impossible. Diamond samples used in these experiments typically have a size of several cubic millimetres, which exceeds the mode volume of a coplanar waveguide by many orders of magnitude - coupling to all spins in such a sample is impossible. Therefore, a new resonator design was developed based on a lumped element approach that addresses the issue of inhomogeneous single spin Rabi frequencies. There, the magnetic field is focused such that the spatial variance throughout the sample volume has a root mean square deviation of 1.54% [84]. To do so, metallic structures in a closed box were introduced which mimic a discrete capacitance and an inductance. This geometry ensures that the field is confined in a small mode volume and has a homogeneous spatial distribution and, hence, the single spin coupling rate is constant for all emitters. In Figure 4.4 a, a photograph of the resonator with its bow-tie like structures is presented (top cover of

the resonator removed). The total capacitance of the circuit is given by

$$C_{\text{tot}}^{-1} = C_1^{-1} + C_2^{-1} = 2C^{-1} = \frac{2}{\epsilon_0} \frac{d}{A}. \quad (4.13)$$

In this expression,  $A$  denotes the surface area on top of the bow-tie and  $d$  is the distance to the top cover. The inductance is given by the current path that connects the two capacitors and closes the current loop via the top cover. This is further illustrated in Figure 4.4 c, where the charges of the capacitors and the magnetic field generated by the inductance are drawn. The value for the inductance can be approximated by the expression for a flat wire inductance:

$$L = 2 \times 10^2 l \left( \ln \left( \frac{l}{w+t} \right) + 0.5 + 0.2235 \frac{w+t}{l} \right) \text{ [nH]} \quad (4.14)$$

The wire width  $w$  is given by the structure width at the beginning of the sample region,  $t$  denotes the skin depth and  $l$  is the current path length. In Figure 4.4 b the corresponding circuit diagram is shown.

Typical design parameters yield a value for each capacitance of  $C_{1,2} = 5.8$  pF. The inductances are given by  $L_1 = 0.15$  nH and  $L_2 = 0.8$  nH. The total inductance,  $L_{\text{tot}} = L_1 + L_2$ , together with the total capacitance then results in a resonance frequency of  $\omega_c \approx 3$  GHz.

The resonator was designed such that the distance between the bow-tie structures can be changed even after manufacturing. This is done by inserting each bow-tie half into a long hole and securing it with a hex nut from the outside. The coupling to the external circuitry is done by inserting coaxial pin couplers through the two holes below the metal structures. By changing the pin length the coupling capacitances are changed and hence, the cavity can be operated either in the over- or under-coupled regime. All properties of the resonator are only dependent on the geometric values of  $l$ ,  $w$ ,  $A$ ,  $d$  and the coupler pin length, and not on the dimensions of the enclosing copper box. This gives a wide range of tune-ability and adjust-ability for a single manufactured cavity design.

As drawn in Figure 4.4 b, the current is counter propagating in the bow-tie structures, focusing and reinforcing the magnetic field in the sample region. This is not the only supported mode by the structure. Transmission spectroscopy, together with a numerical simulation of eigenmodes revealed a second mode with lower frequency. This LC resonance occurs when the current path is closed via the top cover and side walls, and not via the inner part of the bow-tie structures. As the current path is much longer, the resonance frequency is lower than the other mode (also the mode volume is much larger). Furthermore, the magnetic field is not focused but rather distributed

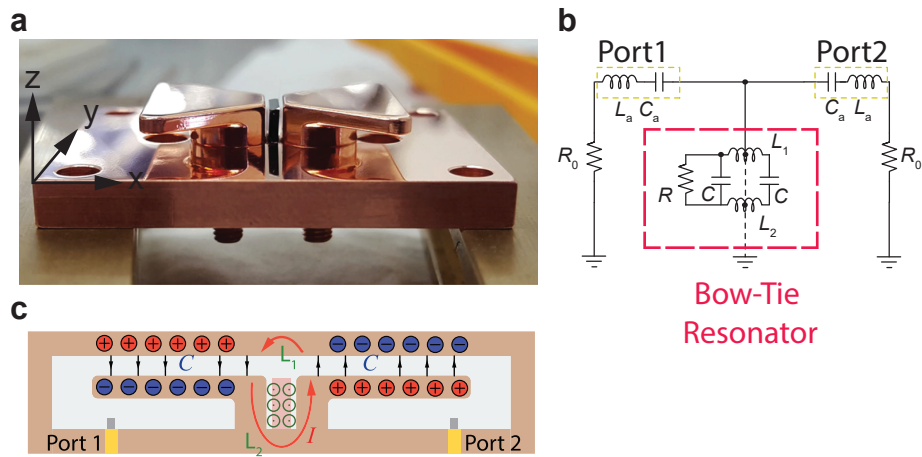


**Figure 4.4.: 3D lumped element resonator.** **a**, Photograph of a bow-tie cavity manufactured out of oxygen-free copper. The top cover and the middle frame are removed for illustration purposes. In the pit between the individual bow-tie halves a diamond sample can be mounted. In the photograph the diamond sample is the black square in the centre. To ensure good contact to the resonator and hold the sample in place, a small amount of vacuum grease is used as adhesive. **b**, Simplified circuit model of the resonator. The resonator is coupled to the external circuitry via two antenna pins. **c**, Illustration of the cross section of the resonator, perpendicular to the mode direction. The bow-tie structures are building capacitors with the top cover. Depending on the top area of the structures and the distance to the top cover, the total capacitance can be changed. The charges are illustrated at the two capacitances  $C_1$  and  $C_2$ . The inductance is given by the pit between the bow-ties and the small part on the top cover. The oscillating magnetic field is focused in the pit with the direction indicated by the arrow heads.



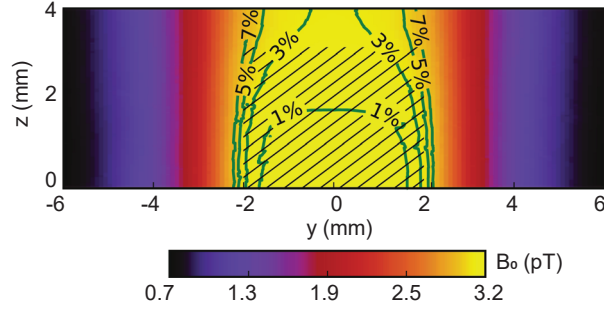


**Figure 4.5.: Magnetic field simulation.** Simulated distribution of the magnetic field amplitude between the bow-tie structures. The dashed lines mark the region where the diamond sample is positioned. There the highest deviation of the magnetic field is 7%, with a RMS deviation of 1.54%.

throughout the box volume and makes this mode unsuitable for coupling to emitters.

### Single Spin Coupling Rate

The numerical simulation of the magnetic field distribution in the sample region has been done with the RF tool of COMSOL Multiphysics©. The results of this study is plotted in Figure 4.5. There one can see that the magnetic field amplitude varies within 7% with a RMS error value of 1.57%. An estimation for the amplitude of the magnetic vacuum field for the mode volume ( $\sim 200 \text{ mm}^3$ ) yields  $B_0 = \sqrt{\mu_0 \hbar \omega_c / (2V)} \approx 3 \text{ pT}$ . Therefore, the mean single electron spin Rabi frequency is  $g_e/2\pi \approx 50 \text{ mHz}$ .

For a single NV centre in a diamond with (001) surface in parallel to the oscillating magnetic field, the single spin coupling rate computes to

$$g_0/2\pi = \sqrt{\frac{2}{3}} \gamma_{\text{NV}} B_0 \approx 70 \text{ mHz}, \quad (4.15)$$

with  $\gamma_{\text{NV}} = 28 \text{ MHz/mT}$ . The pre-factor  $\sqrt{\frac{2}{3}}$  is the projection of the field onto the NV axis.

### Transmission Spectrum

In Figure 4.6 the broadband transmission spectrum of copper bow-tie resonator is presented. By fitting a Lorentzian line shape to the measured transmission data, the resonance frequencies and the damping rates (also Q value) of both bow-tie modes can be extracted. Only the mode around 3 GHz is suitable for coupling to magnetic

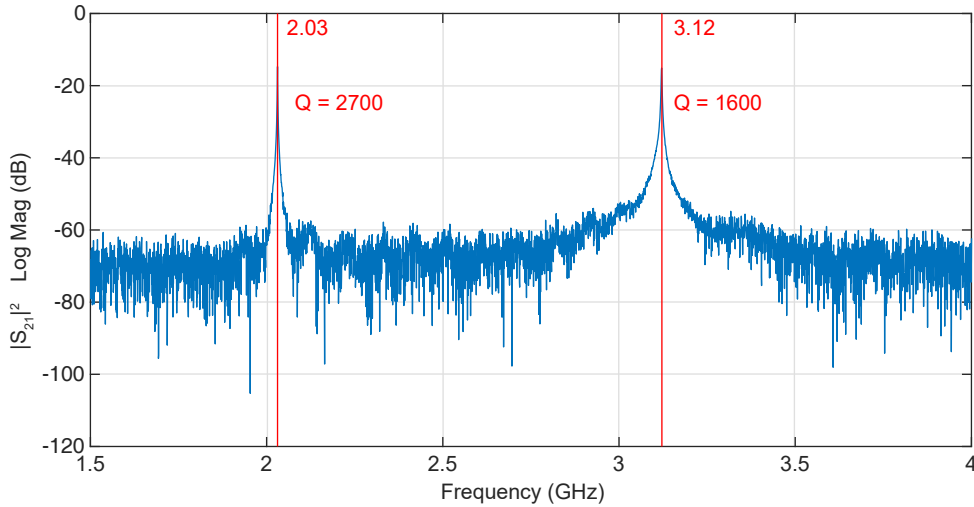


**Figure 4.6.: Broadband transmission spectrum.** The resonator supports two modes which exhibit a resonance at 2.03 GHz and at 3.12 GHz. The figure presents the broadband transmission scattering amplitude  $|S_{21}|^2$  obtained from the vector network analyser. The lower mode occupies a bigger volume and has less ohmic losses compared to the higher mode. Therefore, the lower mode exhibits a larger Q value.

dipoles as it focusses the magnetic field in the region between the bow-tie structures.

### Superconducting Resonator

If an external field is necessary to Zeeman tune spin transitions, the resonator has to be manufactured out of oxygen free copper. On the other hand, if it is desirable to work in the zero field limit or even shield the spin system from any external magnetic fields, a superconducting cavity provides an excellent environment for experiments. Ohmic losses can be reduced tremendously when using a superconducting material. This means that the quality factor becomes much larger and the linewidth very small. A typical cavity transmission spectrum for this type of resonator can be found in Figure 4.7. There the Lorentzian line shape is plotted above and below the superconducting phase transition.

The superconducting material of choice was standard machine grade aluminum (EN AW 6066) as it can be manufactured easily in the in-house workshop. Pure aluminum is a type-I superconductor with a  $T_c$  of 1.2 K [85]. The used machine grade aluminum is an alloy that also contains a small amount of iron which results in a reduction of  $T_c$  to about 0.6 K, whereas the superconducting phase is stable at around 0.4 K.

A plot that shows the resonance frequency and the cavity line-width for the super-

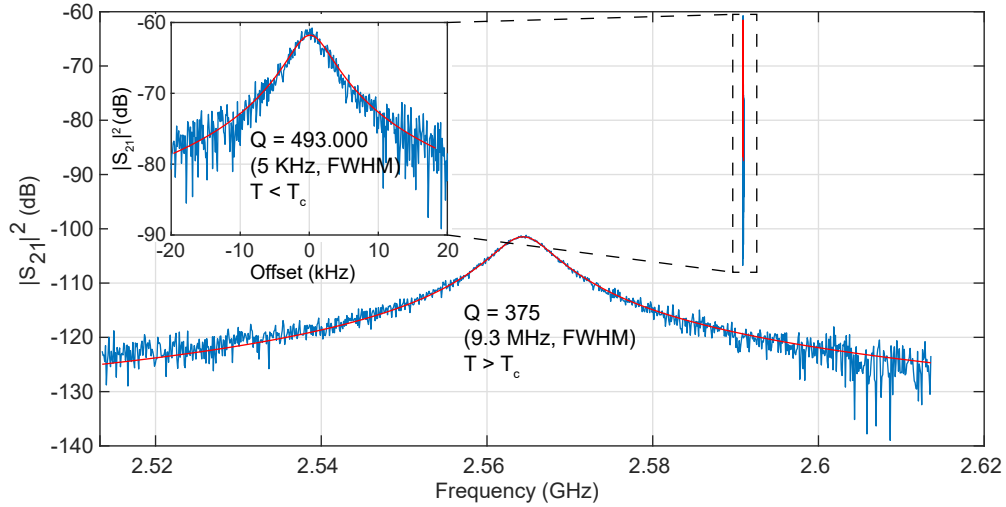


**Figure 4.7.: Comparison of the transmission amplitude.** Measured transmission scattering amplitude above  $T_c$ : The resonance frequency is at 2.566 GHz and has a quality factor of  $Q = 275$ . Below  $T_c$  a resonance frequency of 2.591 GHz with a quality factor  $Q = 493 \times 10^3$  is found.

conducting resonator can be found in Figure 4.8 panel a.

After cooling the resonator below its  $T_c$  and stabilizing the cryostat at a certain temperature, the resonance and the line-width show a relaxation over a timescale of up to 15 min until a steady state is reached. Although rather small, the frequency and line-width shift have to be taken into account if the resonator is used for frequency measurements in the time domain.

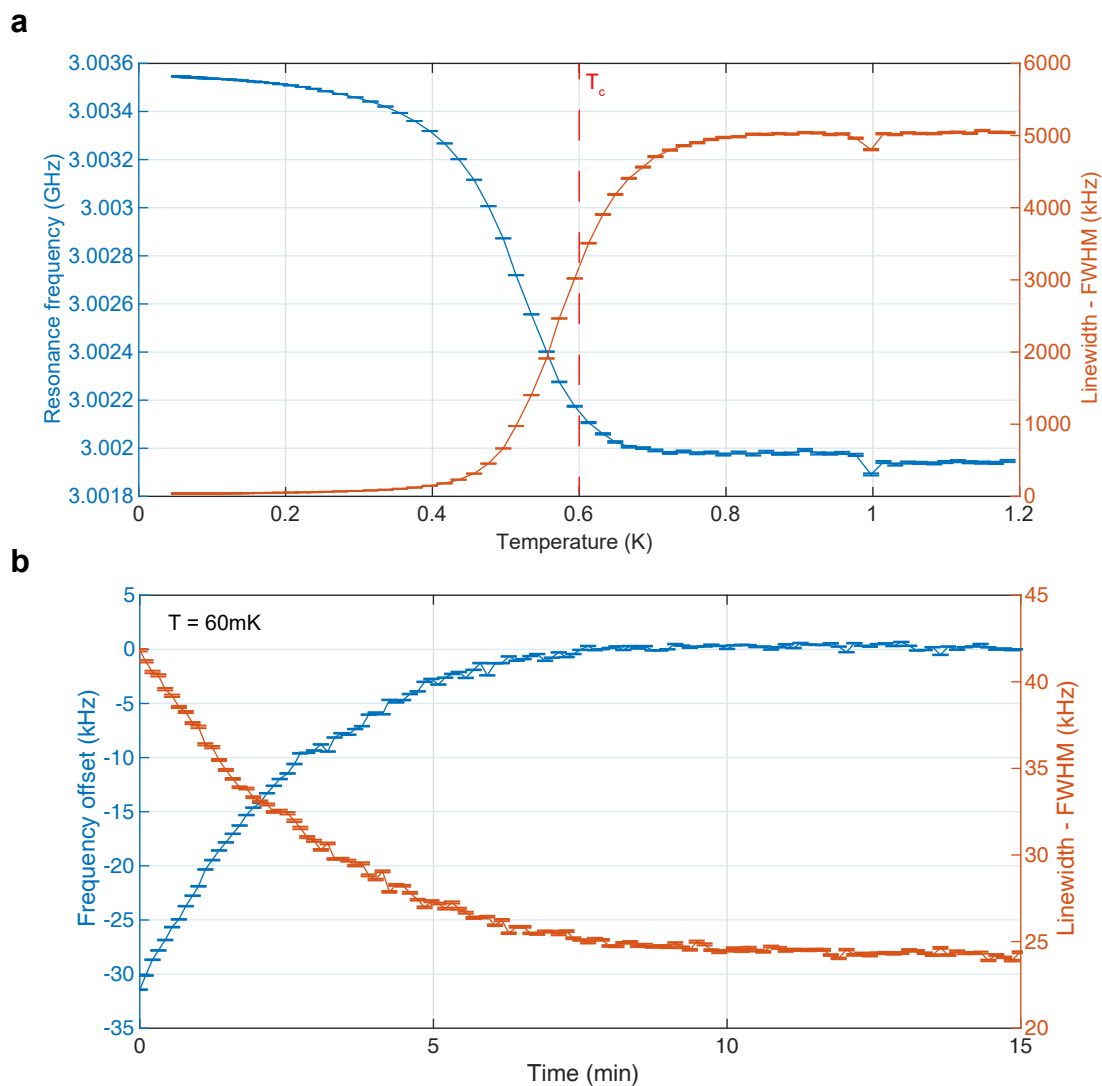


**Figure 4.8.: Bow-tie resonator parameters.** **a**, The plot shows the resonance frequency and the cavity line-width as function of the temperature. In the temperature regime between 1.2 K and 0.4 K the transition to the superconducting phase happens. The initially broad cavity line-width of about 5 MHz is reduced to less than 25 kHz in the superconducting phase. **b**, After stabilizing the resonator to a certain temperature, the line-width and the resonance exhibit a relaxation towards a steady state on a timescale of up to 15 min.

## 5. NV Spins in Diamond - Samples

The research carried out within this work is based on large ensembles of nitrogen vacancy defect centres in diamond. Apart from the natural abundance of this defect in diamond, it is necessary to enhance synthetic diamonds to increase the defect concentration. The starting point are high-pressure, high-temperature (HPHT) diamonds of type Ib. That classifies diamonds with up to 500 ppm dispersed nitrogen impurities throughout the lattice. For the experiments a variety of samples with different properties have been studied:

- **Neutron irradiation - sample N1:**

The HPHT type-Ib raw diamond with an initial nitrogen concentration of  $< 200$  ppm was bought from the company element6. Irradiation with neutrons has been performed with the in-house TRIGA Mark II nuclear reactor of TU Wien. The core provides a broad spectral energy distribution for neutrons above 100 eV with a peak in flux density around 2.5 MeV. With 50 h of irradiation and subsequent annealing for 3 h at 900 °C a NV concentration of  $\approx 40$  ppm was achieved. After enhancement the sample colour changed from its initial yellow, to a deep-black non-transparent tint. It can be assumed that through irradiation with high energy neutrons at high dose, carbon atoms were displaced many lattice sites and lead to extensive crystal damages. Details of this specific sample can be found in ref. [86] (sample BS3-1b).

- **Neutron irradiation - sample D1 and D2:**

The HPHT sample with dimensions 2.9 mm  $\times$  2.9 mm  $\times$  0.5 mm was bought from the company element6 and had a initial nitrogen concentration of  $< 200$  ppm. Similar to the N1, this sample was irradiated with reactor neutrons for 50 h and received a total dose of  $1.4 \times 10^{18}$  cm<sup>-2</sup>. Further details can be found in ref. [86] (sample BS3-2a). The NV density is estimated to be around 30 ppm. The second sample D2 has a size of 3.2 mm  $\times$  3.2 mm  $\times$  0.5 mm, was irradiated for 100 h and received a total irradiation dose of  $1.8 \times 10^{18}$  cm<sup>-2</sup> (sample BS3-3a in ref. [86]). Estimated NV density: 20 ppm.

- **Electron irradiation - sample E3:**

As the previous samples this one was bought at element6 as HPHT type-Ib diamond with a initial nitrogen concentration of  $< 200$  ppm. The enhancement

has been performed with 6.5 MeV electrons while keeping the sample at a temperature between 750 to 900°C. With the total irradiation dose of  $1 \times 10^{18} \text{ cm}^{-2}$  a NV concentration of 10 ppm was achieved. The electrons were generated with a linear accelerator at the Istituto per la Sintesi Organica e la Fotoreattività in Bologna, Italy.

- **Electron irradiation - samples E1 and E2:**

Both samples were provided by Junichi Isoya and his team at the Tsukuba university in Japan. The initial nitrogen concentrations were 100 ppm and 50 ppm respectively. Irradiation was performed with electrons of an energy (2 MeV), generated by a Cockroft-Walton accelerator of the QST, Takasaki. Maintaining a temperature of 800 °C while irradiating and annealing the sample several times at 1000 °C afterwards result in NV densities of 40 ppm (E1) and 13 ppm (E2) respectively. E1 received a total electron dose of  $5.6 \times 10^{18} \text{ cm}^{-2}$  and sample E2 a dose of  $1.1 \times 10^{19} \text{ cm}^{-2}$ .

## 6. Hybrid Quantum System

Up to this point, resonators and NV spin ensembles have been treated as individual entities. In this part they are combined to form a joint, so-called hybrid quantum system - the combination of a solid state spin ensemble and photons in a microwave resonator. Hybrid in this context means the combination of two different entities to form a new joint system. This hybrid architecture is based on the idea of harnessing the individual advantages of the two sub-systems in order to explore new quantum phenomena and quantum technologies [22].

Within this thesis two different resonators are used and so both architectures are briefly introduced as they serve a different purpose:

- **CPW Resonator - NV Hybrid System** for coupling to spatially separated spin ensembles to a common mode. A coplanar waveguide can easily be designed such that the magnetic field exhibits two antinodes. At each antinode a NV ensemble is positioned and can couple to the same bosonic resonator mode.
- **3D Lumped-Element Resonator - NV Hybrid System** for coupling all spins in a diamond ensemble to the resonator mode. This architecture has the advantage that the inversion state of all spins in a macroscopic sample can be determined and is the system of choice for determining the spin lifetime.

### CPW Resonator - NV Hybrid System

As pictured in the photograph in Figure 6.1, the superconducting transmission line resonator is bonded with aluminum wire bonds to a coplanar waveguide transmission line on a surrounding printed circuit board (PCB). The PCB is further equipped with ports for coaxial lines which allow to measure the transmission scattering amplitude of the total system. As pictured in Figure 6.1 the diamond sample is simply placed on top of the superconducting resonator. A spring-loaded pin mounted in the top cover holds the sample securely at its position.

The mode volume of the resonator is only able to fully emerge a small fraction of the spins in the diamond sample. The ratio of coupled volume ( $V_{\text{mode}} \sim 1 \times 10^{-3} \text{ mm}^3$ ) to the diamond volume ( $V_{\text{sample}} \sim 4 \text{ mm}^3$ ) is in the order  $\sim 1 \times 10^{-4}$ .

The diamond-loaded chip together with the PCB is mounted within a gold electroplated copper box - setting boundary conditions for the electromagnetic field. In Figure 6.1 the top is not shown for illustrative purposes.

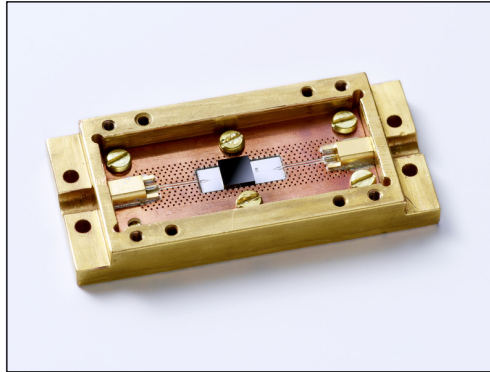


**Figure 6.1.: Diamond backed CPW resonator.** The photograph shows a diamond sample (black cube) positioned on the top of a superconducting CPW resonator. The resonator is connected to the surrounding PCB via aluminum wire bonds. Image taken from ref. [87].

### 3D Lumped-Element - NV Hybrid System

The second hybrid system consists of the same spin ensemble but with a bow-tie resonator. As this cavity possesses a mode volume which has a comparable size to a diamond sample, all spins are fully emerged in the resonator field. In direct comparison to the CPW resonator the big advantage is in the homogeneous single spin Rabi frequency as all spins experience the same field amplitude - making it possible to interface a large ensemble of spins. The drawback of this system is that only by making the mode volume bigger, all spins can be fully emerged in the field and hence the single spin coupling rate becomes smaller.



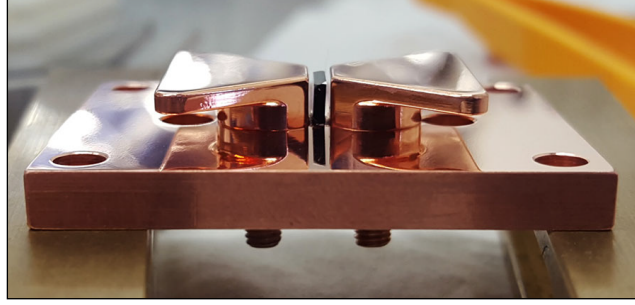


**Figure 6.2.: Diamond loaded bow-tie resonator.** The photograph shows a bow-tie resonator manufactured out of oxygen-free copper, loaded with a diamond sample. A small amount of vacuum grease acts as an adhesive and holds the sample in place. Image taken from [88].

## 6.1. Experimental Set-up

In the experiments carried out here, the spin ensemble can be initialized in its collective ground state  $|G\rangle = |g, \dots, g, \dots, g\rangle$  at low temperatures. As the NV transition at zero magnetic field corresponds to temperatures around 130 mK, a temperature well below that energy gap is necessary (see also Section 1.2) to achieve a high polarization in the collective ground state. Here, a pulse tube pre-cooled adiabatic demagnetization cryostat (ADR) of the company HPD was chosen (Model 103 Rainier) as cryogenic environment. This type of cryostat works after the principle of the magneto caloric effect [89] and, therefore, presents several advantages over a dilution refrigerator:

- A full cool down from room temperature to 2.7 K can be performed within 14 h.
- Minimal base temperature of  $< 50$  mK (heat load dependent)
- Precise temperature regulation for temperatures up to 2.7 K. The system provides 120 mJ cooling energy at 100 mK. Without heat load this temperature can be maintained for  $> 150$  h.

Precise temperature regulation will become important for the experiment of determining the spin lifetime of the NV centre as function of temperature. Therefore, a benchmark of the temperature stabilization capabilities of the ADR fridge was carried out. The corresponding data and analysis are displayed in Figure 6.3. The ADR fridge was stabilized at 80 mK and the temperature consecutively measured for over 9 h with a sampling rate of one data point per second (not all data points are shown in the plot). A naive calculation gives an expectation value  $\langle T \rangle = 80.0016$  mK with a standard deviation  $\sigma = 0.021$  mK. However, this is not a statement of how stable the temperature is in short periods of time. Figure 6.3 b presents the mean and standard

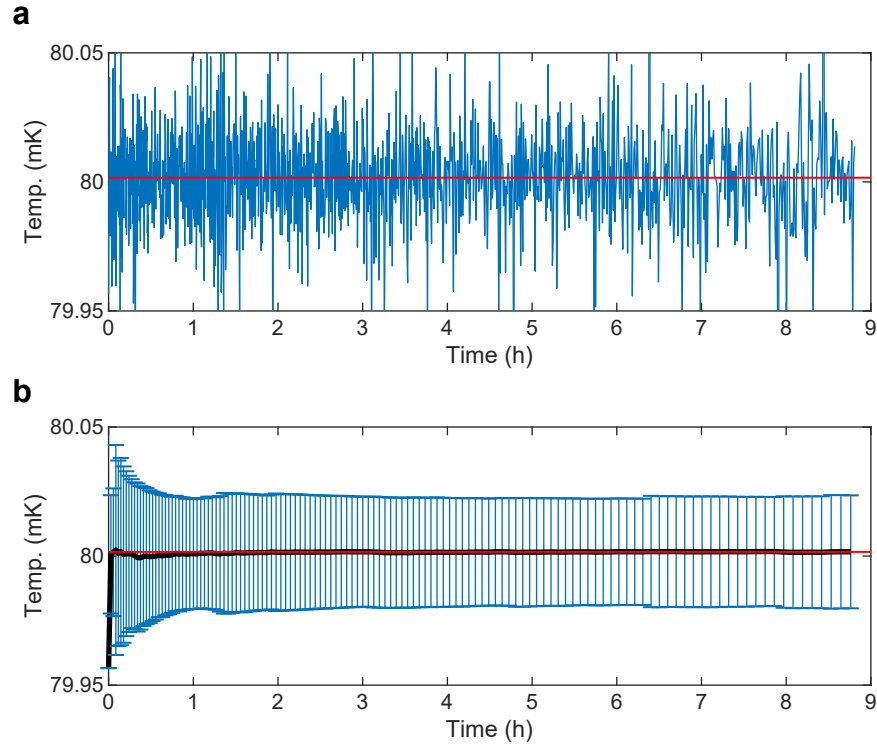


**Figure 6.3.: Temperature stability analysis.** **a**, Measured temperature data over 9 h. The horizontal red line corresponds to the mean value evaluated for the whole data set. **b**, Analysis of the standard deviation and mean over a variety of time scales. The black line corresponds to the local mean value with error bars given the standard deviation. The red line represents the mean value.

deviation of the temperature as function of the averaging period. One can see there that by averaging over longer and longer time periods the short-term stability converges to the long-term stability. From this evaluation it can be concluded that the ADR fridge provides very precise temperature regulation even on short time scales.

A disadvantage of the system is the limited cooling energy, which does not allow to stay at a certain temperature for an indefinite amount of time. The energy provided by a ferric ammonium alum (FAA) salt for cooling and regulating the temperature has to be recharged. This is done by magnetizing the spins in the salt in a strong magnetic field and removing the excess heat by connecting it to a pulse tube cooler (Cryomech model PT407, 0.7 W at 4.2 K). A typical cool down sequence from room temperature with subsequent temperature regulation is plotted in Figure 6.4 with its different phases.

In Figure 6.5 a photograph of the cryostat is presented together with an illustration

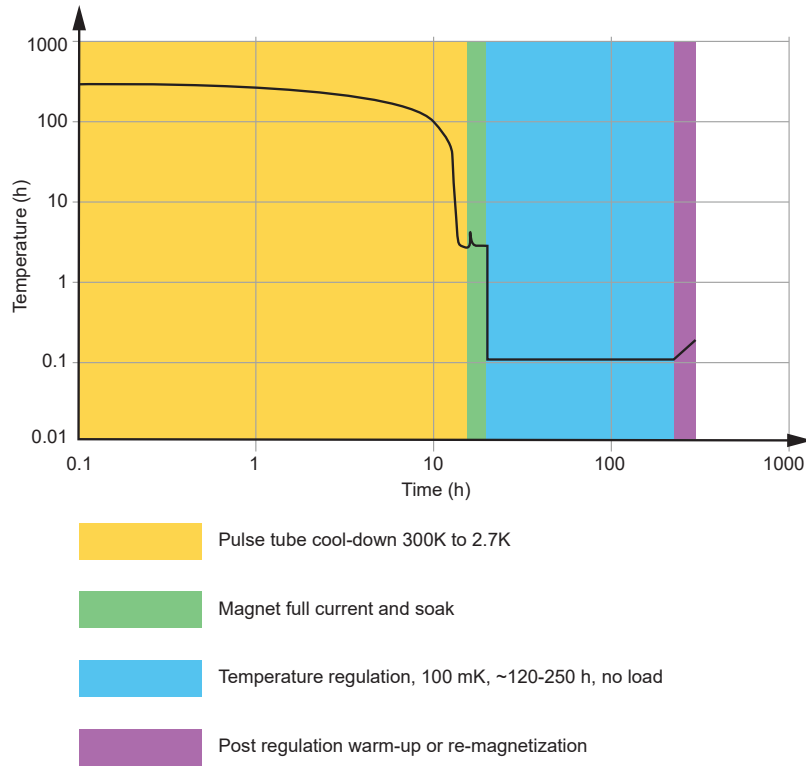


**Figure 6.4.: Cool-down sequence.** With a pulse tube cryo cooler the system is cooled to a base temperature of 2.7 K (orange shaded area). Afterwards the FAA salt is magnetized by a superconducting coil. The excess heat generated during this process is removed by coupling the salt to the pulse tube cooler (green shaded area). In a final step the thermal link between FAA and the pulse tube is disconnected and the magnetic field ramped down. The lowest stage of the cryostat can be temperature stabilized by a controlled demagnetization of the FAA salt (blue shaded area). If the cooling energy is used up, the lowest stage gradually warms up. The heating rate is given by the radiative and conductive heat load of other fridge components (violet shaded area). Illustration similar to [90].

of microwave cable set-up. Starting from the top plate, semi-rigid coaxial cables<sup>1</sup> are installed to interface the resonator that is placed inside a superconducting 3D Helmholtz coil. Stainless steel cables have been used to connect stages of different temperatures. Within one temperature stage copper cables are used to guarantee good thermal heat anchoring. Further measures for decreasing the heat load are inner-outer DC blocks<sup>2</sup> in the coaxial lines. These components electrically isolate the coaxial lines between stages and act as a tiny capacitance. Additionally, several microwave attenuators are installed to avoid thermal photons in the resonator. The total attenuation in the down-line, including  $-10$  dB cable losses, is approximately  $-60$  dB. Additionally, at the lowest stage, a three dimensional Helmholtz coil provides DC magnetic fields up to 100 mT in arbitrary directions. In combination with coplanar waveguide resonators, this is further used to tune the transition energy in resonance with the resonator.

### 6.1.1. Spectroscopy Set-up

In the experiments the system is probed by transmission spectroscopy with low power continuous wave microwave signals. This is done with a vector network analyzer (VNA)<sup>3</sup> that can measure the scattering amplitude ( $|S_{21}|^2$ ) for frequencies up to 8.5 GHz. The signal that exits port 1 of the VNA is attenuated by  $-60$  dB (attenuators and cable losses), passes through the experiment and is subsequently amplified by a high-electron-mobility transistor (HEMT) with a gain of 40 dB<sup>4</sup>. Before entering port 2 of the VNA, the signal is further amplified by 30 dB<sup>5</sup> at room temperature. An illustration of the used microwave set up is given in Figure 6.5, panel b.

An additional microwave power spectrum generator<sup>6</sup> provides continuous wave microwave signals which can be used for spin manipulation.

---

<sup>1</sup>Cryogenic stainless steel outer jacket and centre conductor, UT-085-SS-SS Tek-Stock, LLC

<sup>2</sup>Fairview SD 3258 inner-outer DC block, 0.5 dB insertion loss

<sup>3</sup>Rhode & Schwarz, model RSZNB 8

<sup>4</sup>LNF-LNC1.8-2.8A, Low noise factory,  $T_{\text{noise}} = 5.5$  K

<sup>5</sup>AFS3-02000400-08-CR-4, L3 Narda-MITEQ,  $T_{\text{noise}} = 8$  K

<sup>6</sup>Anritsu, MG3692c

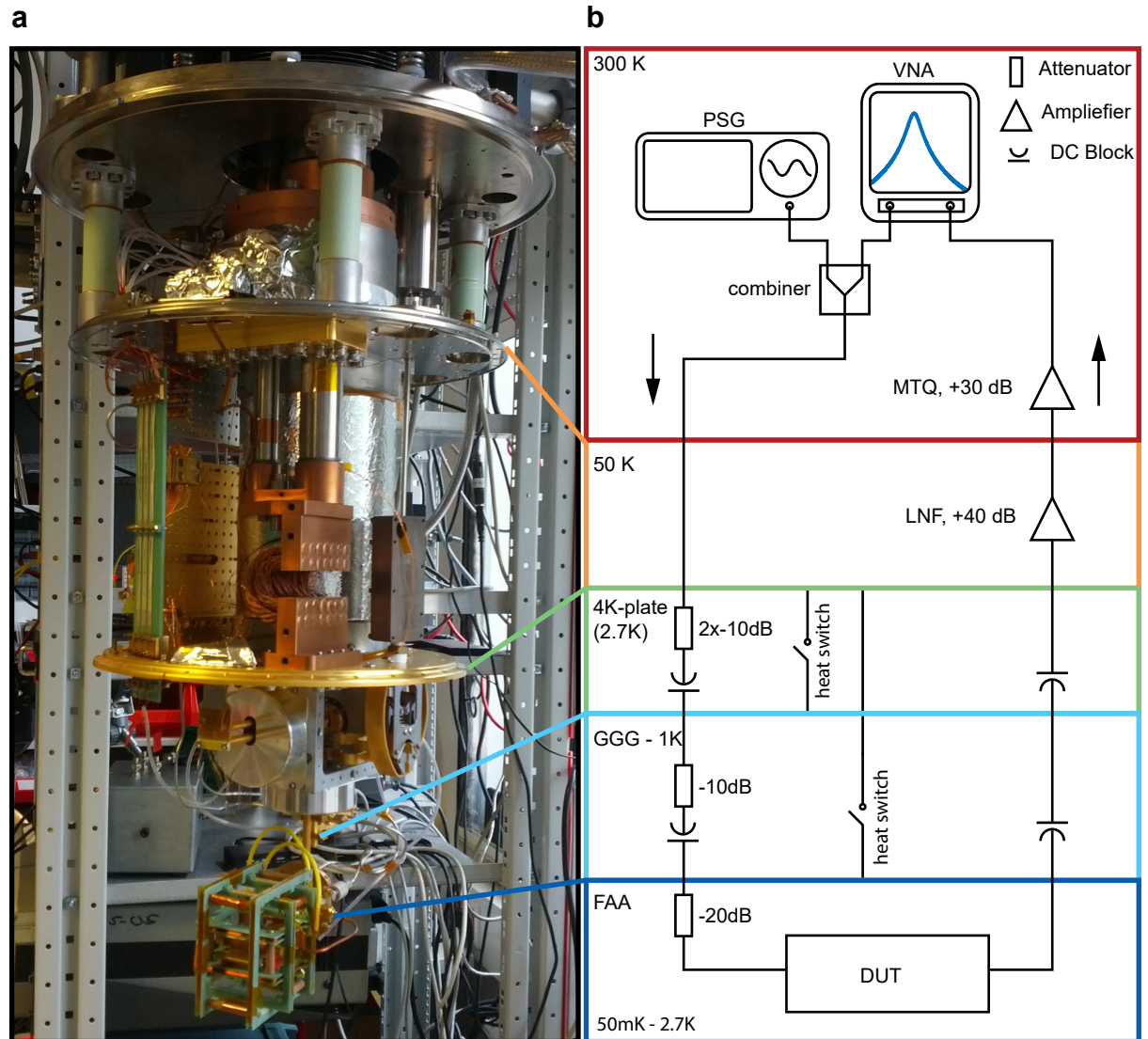


**Figure 6.5.: ADR cryostat set-up.** **a**, Photograph of the cryostat with removed heat shields. The 50 K and 4 K stages are cooled by a pulse tube cryo cooler. Below the 4 K plate (golden) on the right the heat switch is located. It thermally connects the FAA and GGG stage to the 4 K temperature stage. At the bottom a 3D-Helmholtz coil set-up is connected to the FAA rod. **b**, Layout of the microwave set-up in the cryostat. The down-line is equipped with DC blocks and attenuators. In the up-line the low-noise amplifier provides high isolation from photons. The VNA is used to probe the device under test (DUT). A power combiner allows to inject an additional continuous wave signal from a power spectrum generator (PSG).

**Part III.**  
**Scientific Results**

# 7. Strong Coupling: 3D Lumped Element Mode and Spin Ensemble

In this chapter the strong coupling of an ensemble of NV spins with a bow-tie resonator mode will be shown. The fundamental experiments and observations of normal mode splitting have been demonstrated and studied for atoms in optical cavities already in the past [91]. Furthermore, strong coupling of NV spins [19–21, 92, 93] and other solid state systems [82, 94–96] to a resonator mode have been successfully shown.

Strong coupling between a large NV spin ensemble and the lumped element mode is a fundamental necessity for parts of the work within this thesis. Therefore, this chapter addresses this problem and presents strong coupling of a large NV spin ensemble and the 3D lumped element mode. Parts of this chapter are based on the following article:

- **Collective strong coupling with homogeneous Rabi frequencies using a 3D lumped element microwave resonator**  
A. Angerer, **T. Astner**, D. Wirtitsch, H. Sumiya, S. Onoda, J. Isoya, S. Putz, and J. Majer  
*Applied Physics Letters* **109**, 033508 (2016)

The technical details concerning the operation and functionality of this type of resonator has been already introduced in Section 4.2.

In the following experiment the sample E1 with a total number of  $N \approx 3.85 \times 10^{16}$  NV centres in the crystal was chosen. With the given mode volume the vacuum magnetic field oscillations have an amplitude of  $\approx 3$  pT that result in a single spin coupling rate of  $g_0/2\pi = \frac{\gamma_e}{\hbar} |\mathbf{B}_0| \sqrt{\frac{2}{3}} |\mathbf{S}| \approx 70$  mHz (Section 4.2). The used diamond sample was cut along the (001) diamond plane and the defect centres are aligned with the  $\langle 1, 1, 1 \rangle$  crystallographic direction. This justifies the factor  $\sqrt{\frac{2}{3}}$  as it accounts for the projection of the cavity field vector onto the NV principal axis. With this the collective coupling strength can be estimated by  $\Omega_{\text{calc}}/2\pi = \sqrt{N} g_0 \approx 13.7$  MHz.

The diamond loaded cavity exhibits a resonance at  $\omega_c/2\pi = 3.121$  GHz and a Q factor of 1637 - corresponding to a cavity damping rate  $\kappa/2\pi = 1.91$  MHz HWHM (half width at half maximum). With a 3D Helmholtz coil a field of 10 mT is applied in the  $[0, 1, 0]$  direction to tune the spin transition of all four sub-ensembles (see Chapter 1)

in resonance with the cavity mode. Keeping the sample at a temperature of 25 mK ensures a thermal polarization in the  $m_s = 0$  ground state well above 99%.

In the experiment the transmission scattering amplitude  $|S_{21}|^2$  is measured with a VNA. The corresponding transmission spectroscopy data is presented in Figure 7.1 a. At the point where spin transitions and cavity mode are in resonance (Figure 7.1, panel b), an avoided level crossing, corresponding to the vacuum rabi splitting of the coupled system, is observed. An analytical expression for  $|S_{21}|^2$  that is obtained from a Jaynes-Cummings Hamiltonian is fitted to the experimental data [84]:

$$|S_{21}|^2 = \left| \kappa \frac{(\omega - \omega_s - i\gamma^*)}{(\omega - \omega_c - i\kappa)(\omega - \omega_s - i\gamma^*) - \Omega^2} \right|^2, \quad (7.1)$$

the collective coupling strength  $\Omega/2\pi = 12.46$  MHz and the inhomogeneous broadened spin line-width of  $\gamma^*/2\pi \approx 3$  MHz can be extracted. The collective coupling strength is large enough to exceed both loss rates ( $\Omega > \kappa, \gamma^*$ ) and, therefore, satisfies the condition for the strong coupling regime of cavity QED.

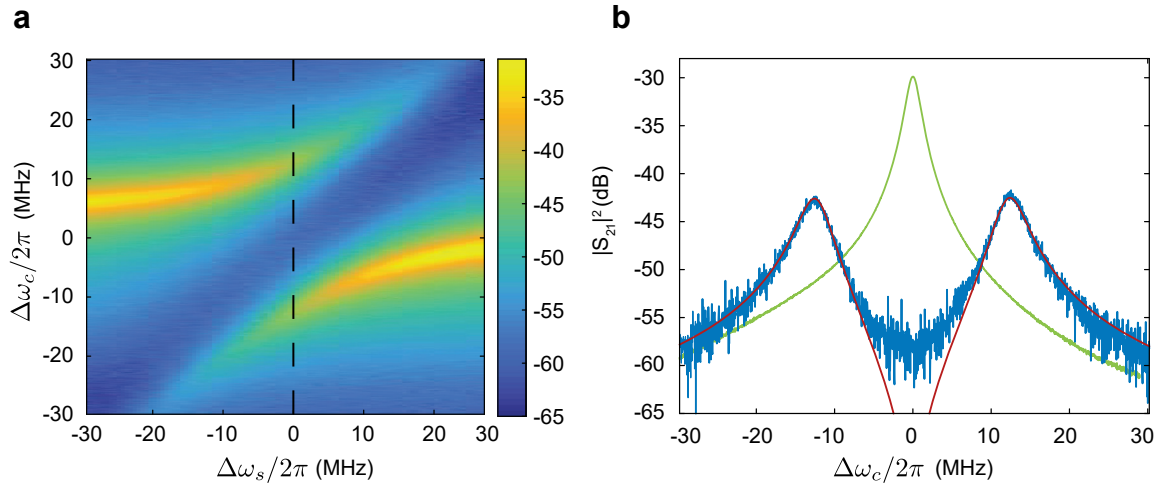


**Figure 7.1.: Strong coupling between a spin ensemble and the bow-tie mode.** **a**, Transmission spectroscopy as function of the detuning. Here  $\Delta\omega_c/2\pi$  is the detuning of the probe signal to the central spin transition frequency and  $\Delta\omega_s/2\pi$  for the detuning of the resonator frequency with respect to the spin transition. **b**, Cut through the transmission data shown in **a** (dashed black line) at the position  $\Delta\omega_s/2\pi = 0$ . The green curve shows the Lorentzian line shape of the cavity with a far detuned spin transition. In the case of resonance the normal mode splitting is observed (data in blue). Fitting the expression in equation Equation (7.1) (red line) to the data yields a collective rabi frequency of  $g_N/2\pi = 12.46$  MHz.

Comparing the measured collective coupling to the previously made estimate based on the number of NV centres in the crystal shows good agreement. Several arguments



that explain the deviation in the numbers can be made: First, the NV density was determined by comparing EPR spectroscopy data to reference samples. The exact density and hence the number of NV centres is not exactly known. Second, the cavity mode volume is determined from finite element simulation data which does not fully resemble the physical system at hand.

Having good agreement between measured coupling strength and the initially calculated value, further enables one to get an estimate on the number of NV centres in an unknown sample.

# 8. Spin Lifetime of a Nitrogen Vacancy Centre

This chapter is based on the following research publications:

- **Solid-state electron spin lifetime limited by phononic vacuum modes**  
T. Astner, J. Gugler, A. Angerer, S. Wald, S. Putz, N. J. Mauser, M. Trupke, H. Sumiya, S. Onoda, J. Isoya, J. Schmiedmayer, P. Mohn, and J. Majer  
*Nature Materials* **17**, 313-317 (2018)
- **Ab initio calculation of the spin lattice relaxation time  $T_1$  for nitrogen-vacancy centers in diamond**  
J. Gugler, T. Astner, A. Angerer, J. Schmiedmayer, J. Majer, and P. Mohn  
*Phys. Rev. B.* **98**, 214442 (2018)

These two publications came out of a joint collaboration with the Computational Material Science (CMS) department of TU Wien. Johannes Gugler and Peter Mohn were responsible for the *ab initio* calculations and a constant exchange of information between them and the experimental team at the Atominstitut of TU Wien made this work possible. Furthermore, diamond samples with outstanding properties have been provided by the team around Junichi Isoya from the University of Tsukuba in Japan.

## 8.1. The Lifetime Problem

Longitudinal relaxation processes of solid state electron spins have been studied experimentally and theoretically for over many decades. The basic definition of the spin lattice relaxation is how the component of the magnetization vector along a principal direction equilibrates with the surrounding lattice. A process that is happening on the characteristic time scale known as  $T_1$ .

The starting point was the work done by Ivar Waller in the early 90's, where he was able to theoretically describe the spin lattice relaxation of a paramagnetic crystal [44]. He took the electron spin-spin interaction and expanded it in terms of the movement of the associated ions. This allowed him to describe a spin-phonon interaction with an

effective Hamiltonian.

Followed by the work done by Kronig [97], van Vleck [98] and Gorter [99], effects of spin-orbit coupling were introduced in the theory of spin lattice relaxation and subsequently refined by Elliott [100] and Yafet [101].

For the NV centre, theoretical calculations and experiments [102–104] revealed a two-phonon Raman [105] and the Orbach [106, 107] process as the dominating effects concerning the spin lattice relaxation of this defect. However, the studies on  $T_1$  done so far were either performed at high magnetic fields using electron paramagnetic resonance techniques or carried out at high temperatures [108, 109]<sup>1</sup>. At temperatures around 2 K,  $T_1$  was measured for two samples and the results differed by more than one order of magnitude [110]. This was then attributed to sample dependent cross relaxation processes that can change the  $T_1$  time tremendously [102]. The (to the authors knowledge) only measurement concerning the temperature regime below the zero-field transition energy of the NV centre was done in Ref. [21]. The authors present a  $T_1$  measurement for a single sample at one specific temperature. Furthermore, they used a  $\lambda/2$  coplanar waveguide resonator with inhomogeneous single spin coupling, making it impossible to read out the state of the whole ensemble. From these measurements, no statement about the underlying process and mechanisms of spin lattice relaxation for the NV centre in the low temperature limit can be made.

Within this part of the thesis, this question is addressed with respect to a new measurement technique and experimental determination of the  $T_1$  time at low temperatures. The theoretical background and a microscopic theory has already been introduced in Section 1.3, whereas details on the *ab initio* calculations are found in the thesis of Johannes Gugler [111].

## 8.2. Experimental Verification

To determine the spin lattice relaxation at low temperatures, the following conditions are desirable:

- The collective state of all spins has to be determined
- A read-out method that does not alter the state of spins
- Initializing the system only once for a full relaxation curve in the time domain

Several issues arise with standard optical detected magnetic resonance (ODMR) schemes. This technique uses a laser pulse to drive the NV centre from the triplet ground state

---

<sup>1</sup>High temperature in this context means at temperatures that are well above the corresponding transition energy of about 3 GHz

to the triplet excited state. Depending on the change of the observed fluorescence intensity, the state of the system can be determined. As the laser used for such a readout scheme usually has a wavelength of 546 nm, it introduces an energy much larger than the transition energy of the defect centre into the system (546 nm corresponds to THz radiation, or a temperature of  $2.6 \times 10^6$  K, whereas the NV transition is in the few GHz range or a corresponding temperature of 130 mK). This energy can excite high energy phonon modes which then can excite NV spins in the ensemble. Additionally, the samples here possess large spin densities and are opaque. This makes it merely impossible to read out the inversion state of all spins in the ensemble by means of ODMR.

Here it is desirable to probe and readout the whole ensemble continuously without disturbing its actual state and evolution in time. This can be achieved by a non-perturbative readout scheme in the framework of cavity QED [61, 112].

### Dispersive Detection Scheme

Figure 8.1 presents a graphical illustration of the system consisting of a spin ensemble dispersively coupled to a resonator mode. The spins are further interacting with the phonons of the diamond crystal. By exchanging energy with the phonons the state of the spin ensemble changes, which produces a detectable feedback on the cavity mode. Therefore, by probing the cavity, information about the state of the spin ensemble can be inferred.

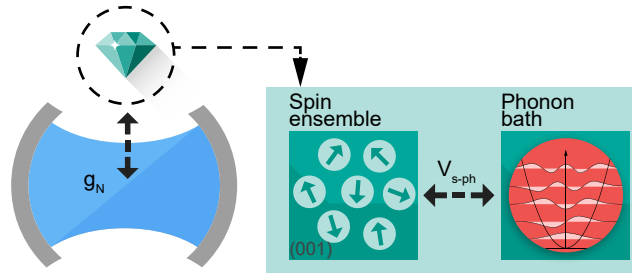


**Figure 8.1.: Experimental set-up.** The NV ensemble is dispersively coupled to the cavity mode. The state of the ensemble can then be inferred by probing the cavity mode. The energy exchange between spin ensemble and phonon bath drives both systems into their thermodynamic equilibrium. This interaction is illustrated by the generic potential  $V_{s-ph}$ . Illustration similar to ref. [113].

In the the experiment the condition for being in the dispersive limit of cavity QED,  $|\omega_c - \omega_s| \gg g_N$ , is always maintained. This is important to avoid any cavity enhanced

relaxation [114]. For the system at hand, the typical Purcell enhancement factor [113] can be calculated by

$$\Gamma_P = \kappa \frac{g_0^2}{\kappa^2/4 + \Delta^2}, \quad (8.1)$$

in which  $\Delta = |\omega_s - \omega_c|$  is the spin-cavity detuning,  $\kappa$  the cavity damping rate (FWHM) and  $g_0$  the single spin coupling rate. Calculating this for typical system parameters leads to a negligible Purcell relaxation rate of  $\Gamma_P \approx 10 \times 10^{-14} \text{ s}^{-1}$ .

Next, equations of motion will be derived with a quantum master equation approach. The system Hamiltonian can be written as a modified driven Tavis-Cummings Hamiltonian for a three-level system with two degenerate excited levels:

$$\frac{\hat{H}_{\text{sys}}}{\hbar} = \omega_c \hat{a}^\dagger \hat{a} + \frac{\omega_s}{2} \hat{S}_z^2 + ig_0 (\hat{a}^\dagger \hat{S}^- - \hat{a} \hat{S}^+) + i\eta (\hat{a}^\dagger e^{-i\omega_p t} - \hat{a} e^{i\omega_p t}), \quad (8.2)$$

where  $a/a^\dagger$  are the usual creation/annihilation operators of the cavity mode with angular frequency  $\omega_c$ . The last part of the Hamiltonian gives a probe field with amplitude  $\eta$  at angular frequency  $\omega_p$ . The collective coupling rate between the cavity and the spin ensemble is given by  $g_N = \sqrt{N} g_0$ , where  $N$  denotes the number of spins and  $g_0$  the single spin coupling rate. The spin inversion, a measure for the population in the  $m_s = \pm 1$  state of an ensemble containing  $N$  spins, is given by the operator

$$\hat{S}_z^2 = \sum_j^N \hat{\sigma}_{z,j}^2. \quad (8.3)$$

For the ensemble of  $N$  spins a collective spin ladder operator has the form

$$\hat{S}^\pm = \sum_j^N \hat{\sigma}_j^\pm. \quad (8.4)$$

The just defined operators use the NV centre basis ( $|1\rangle, |0\rangle, |-1\rangle$ ) and the associated single spin operators<sup>1</sup>

$$\hat{\sigma}_z^2 = |1\rangle \langle 1| + |-1\rangle \langle -1|, \quad (8.5)$$

$$\hat{\sigma}^- = |0\rangle \langle 1| + |0\rangle \langle -1|, \text{ and} \quad (8.6)$$

$$\hat{\sigma}^+ = |1\rangle \langle 0| + |-1\rangle \langle 0|. \quad (8.7)$$

In the experiment the  $T_1$  is determined for different temperatures, thermal excitations

---

<sup>1</sup>These operators must not be confused with the standard Pauli operators which are part of the SU(2) group. Here these operators are part of the U(3) group because of the treatment of the NV system as a V-level.

in the ensemble have to be taken into account. The non-unitary evolution of the density matrix is implemented similarly to ref. [92], as a master equation in Lindblad form:

$$\frac{d}{dt}\hat{\rho} = -i [\hat{H}_{\text{sys}}, \hat{\rho}] + \hat{\mathcal{L}}[\hat{\rho}], \quad (8.8)$$

with the Liouvillian

$$\begin{aligned} \hat{\mathcal{L}}[\hat{\rho}] = & \left( 2\hat{a}\hat{\rho}\hat{a}^\dagger - \hat{a}^\dagger\hat{a}\hat{\rho} - \hat{\rho}\hat{a}^\dagger\hat{a} \right) \\ & + \frac{\Gamma_1}{2} \left( 2\hat{S}_j^- \hat{\rho} \hat{S}_j^+ - \hat{S}_j^+ \hat{S}_j^- \hat{\rho} - \hat{\rho} \hat{S}_j^+ \hat{S}_j^- \right) \\ & + \frac{\gamma_\perp}{2} \left( 2\hat{S}_z^2 \hat{\rho} \hat{S}_z^2 - \hat{S}_z^2 \hat{\rho} - \hat{\rho} \hat{S}_z^2 \right). \end{aligned} \quad (8.9)$$

The first line in Equation (8.9) describes the cavity photon damping with the rate  $\kappa$ . Decay of spin excitations are proportional to the operator  $\hat{S}^-$  and have the rate  $\Gamma_1$ . Processes of decoherence are proportional are energy conserving and have a proportionality to  $\hat{S}_z^2$  with the rate  $\gamma_\perp$ .

The master equation allows to derive the equations of motion for the operators  $\langle \hat{a} \rangle$ ,  $\langle \hat{S}^- \rangle$ ,  $\langle \hat{S}_z^2 \rangle$ ,  $\langle S^+ S^- \rangle$ , and  $\langle a \hat{S}_z^2 \rangle$ . Here the ansatz  $\langle a \hat{S}_z^2 \rangle = \langle \hat{a} \rangle \langle \hat{S}_z^2 \rangle$  can be used to derive the so-called Maxwell-Bloch equation for the system. Details on the derivation of the Maxwell-Bloch equations can be found in Appendix D.

The steady state is of special interest as it describes the feedback of the spin population on the cavity mode. By setting the system of coupled equations to zero yields the steady state solution for the intra cavity intensity

$$\langle \hat{a}^\dagger \hat{a} \rangle = \frac{\eta^2}{\left( \kappa + \frac{8g_N^2(2-3\langle \hat{S}_z^2 \rangle)(2\gamma_\parallel + \gamma_\perp)}{(2\gamma_\parallel + \gamma_\perp)^2 + 16\Delta_s^2} \right)^2 + \left( \Delta_c + 32 \frac{g_N^2 \Delta_s (2-3\langle \hat{S}_z^2 \rangle)}{(2\gamma_\parallel + \gamma_\perp)^2 + 16\Delta_s^2} \right)^2}, \quad (8.10)$$

where  $\Delta_c = \omega_c - \omega_p$ . Equation (8.10) shows that the intra cavity field and its damping rate  $\kappa$  now also acquire parts of the spin dephasing rate  $\gamma_\perp$  and longitudinal relaxation rate  $\gamma_\parallel$ . As the cavity probe field is far detuned with respect to the spin transition,  $\Delta_s$  can be replaced with  $\Delta = |\omega_s - \omega_c| \approx \Delta_s$ . Furthermore, if the parameters  $\gamma_\perp$  and  $\gamma_\parallel$  are much smaller than the cavity-spin transition detuning, they can be neglected. This leads to a simple expression for the intra cavity intensity

$$\langle \hat{a}^\dagger \hat{a} \rangle = \frac{\eta^2}{\kappa^2 + \left( \Delta_c + \frac{g_N^2}{\Delta} (2 - 3 \langle \hat{S}_z^2 \rangle) \right)^2}. \quad (8.11)$$

Equation (8.11) has the form of a Lorentzian line shape. The resonance frequency of the cavity is modified by the dispersive interaction with the spin ensemble. This interaction has a temperature dependence given by the inversion  $\langle \hat{S}_z^2 \rangle$  of the ensemble. Strictly speaking, the degree of inversion  $\langle \hat{S}_z^2 \rangle$  shifts the cavity resonance. Taking the limit of low temperature ( $T \rightarrow 0$ ) the steady inversion reaches its minimum value  $\langle \hat{S}_z^2 \rangle = 0$  and the resonance experiences its maximum shift of  $\frac{2g_N^2}{\Delta}$ . In the limit of high temperatures ( $k_B T \gg \hbar\omega_s$ ), the spin inversion approaches  $\langle \hat{S}_z^2 \rangle \rightarrow \frac{2}{3}$  and the unperturbed cavity resonance frequency is retrieved.

Finally, the relative cavity resonance shift can be expressed as

$$\chi = \omega_c(\hat{S}_z^2) - \omega_c(\hat{S}_z^2 = 2/3) = \frac{g_N^2}{\Delta} (2 - 3\langle \hat{S}_z^2 \rangle) \quad (8.12)$$

The presented expression of the resonance shift is consistent with the theory already introduced in the previous chapters. There, the Hamiltonian was approximately diagonalized by moving to the dispersive regime parameters with a unitary transformation. Here, the resonance shift is additionally modified by the spin inversion  $\langle \hat{S}_z^2 \rangle$ . However, it seems like any time dependence has been removed from the expression of the shift which is essential for measuring the longitudinal relaxation process in the time domain. The time dependence is restored by introducing the time and temperature dependent inversion  $\langle \hat{S}_z^2 \rangle$  in the form

$$\frac{d}{dt} \langle \hat{S}_z^2(t, T) \rangle = -\frac{1}{T_1} (\langle \hat{S}_z^2(t, T) \rangle - \langle \hat{S}_z^2(T) \rangle_{\text{st}}), \quad (8.13)$$

and the temperature dependent steady state of  $\langle \hat{S}_z^2(t, T) \rangle$  as

$$\langle \hat{S}_z^2(T) \rangle_{\text{st}} = \frac{2}{e^{\frac{\hbar\omega_s}{k_B T}} + 2}. \quad (8.14)$$

Here, the solution of the differential equation in Equation (8.13) resembles a pure exponential decay of an arbitrary initial  $\langle \hat{S}_z^2 \rangle$  value towards the thermal equilibrium steady state  $\langle \hat{S}_z^2(T) \rangle_{\text{st}}$ .

The problem of measuring the longitudinal relaxation rate thus has been now mapped onto the problem of determining the spin inversion  $\langle \hat{S}_z^2 \rangle$  as function of time and temperature. Or, in terms of the experiment, measuring the frequency shift of the resonator - a task that is easily achievable in the framework of cavity QED. An advantage of this method is further, that the cavity resonance frequency can be measured continuously. A whole  $\langle \hat{S}_z^2 \rangle$  versus time curve is obtained by initializing the ensemble only once, circumventing the problem of different initial states in a multi-shot

experiment.

### Resonance Shift Detection

For the experiment a superconducting version of the 3D lumped element resonator was used. The resonator was machined out of aluminium<sup>1</sup> and the surface was treated with 0.25  $\mu\text{m}$  grain size polishing paste. Diamond samples are attached to the cavity by using a tiny amount of vacuum grease as adhesive. The main thermal link between the diamond sample and resonator is established via polished surfaces touching each other. Figure 8.2 shows a photograph of the used resonator together with a diamond sample placed in between the bow tie structures.

The resonance frequency  $\omega_c/2\pi = 3.04$  GHz, together with a quality factor of  $Q = 60\,000$  was determined by transmission spectroscopy<sup>2</sup>. With the standard spectroscopy set-up introduced in Chapter 6, the resonator is probed with an input power of  $-110$  dBm, which translates to an average number of  $1 \times 10^{-9}$  photons per spin in the cavity mode.

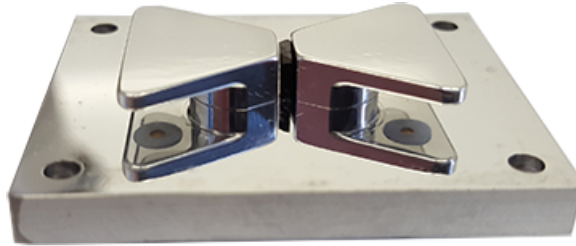


**Figure 8.2.: Superconducting bow-tie resonator.** The photograph shows a bow-tie resonator manufactured out of aluminum. For illustration purposes the middle frame and the top cover of the resonator have been removed. Between the bow-tie structures, the diamond sample is placed (black cuboid). Below the bow tie structures the coupling coaxial pins are visible.

The used resonator has a line-width of 50 kHz (FWHM) and together with the signal-to-noise ratio (SNR) of the detection circuit, the resonance frequency can be determined to a precision of  $\pm 100$  Hz from a Lorentzian fit to the transmission data in a single shot. Typical system parameters suggest that the sample-dependent frequency

<sup>1</sup>Material designation EN AW 6066

<sup>2</sup>Note that this number varies slightly for each diamond sample since they are different in volume. Each diamond introduces a different dielectric loss.



shift  $\chi$  will be in the order of 200 kHz up to 2 MHz, making it easily detectable with the given resolution.

### State Preparation and System Quench

The ensemble is initialized by coupling it to a heat bath<sup>1</sup> at a temperature of 2.7 K. In thermal equilibrium the ensemble is in the state  $\langle \hat{S}_z^2(T = 2.7 \text{ K}) \rangle \approx \frac{2}{3}$ . The next step is to create a non-equilibrium state with respect to the crystal phonon population and the spin excitations. This requires removing the lattice phonons from the system (cooling the crystal) faster than the spin ensemble exchanges energy with phonons. By non-adiabatically ( $\tau_{\text{switch}} \ll T_1$ ) switching to a lower temperature, the spin temperature remains higher compared to the lattice temperature, generating a non-equilibrium state. For target temperatures between 50 - 250 mK the switching time is on the order of 20 - 40 min, which is still fast enough to create a non-equilibrium state.

### Time Evolution of the Spin Inversion

Having created a non-equilibrium state, energy exchange between the spin and the phonon system will drive the whole system towards its thermal equilibrium state. If the spin ensemble is at a higher temperature than the phonons, the process of equilibration will gradually lower the value of inversion  $\langle \hat{S}_z^2 \rangle$  with time. Continuously determining the resonator frequency now allows to follow the decay of the spin inversion into the steady state. A typical measurement run and the time evolution of  $\langle \hat{S}_z^2 \rangle$  are depicted in Figure 8.3 panel a. There, the colour code corresponds to the temperature at which the relaxation was monitored. The data sets can be described with an exponential function, derived from the solution of the differential equation in Equation (8.13). In addition to the decay constant, the steady state inversion  $\langle \hat{S}_z^2 \rangle_{\text{st}}$  can be extracted by fitting an exponential function to the data and taking its  $t \rightarrow \infty$  value. This value is plotted in Figure 8.3 in panel b as function of temperature. Panel c in Figure 8.3 illustrates the state of the lattice photons and the spin ensemble during the experimental procedure.

---

<sup>1</sup>2.7 K here is the heat bath generated by a pulse tube cooler of the ADR fridge. The system has to be cycled through this to regenerate the cooling salt of the fridge.

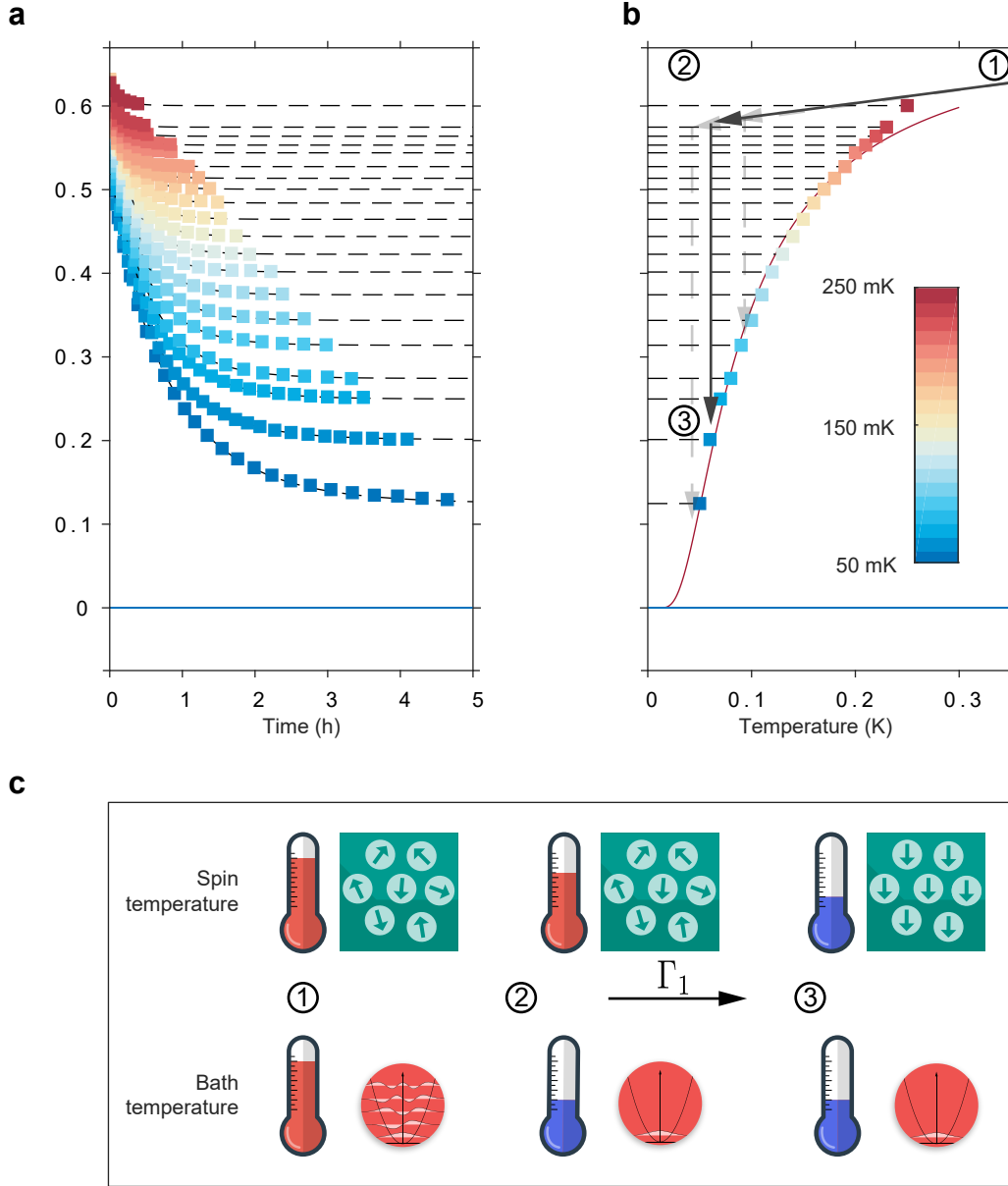


**Figure 8.3.: Time evolution of the spin inversion.** **a**, Measured time dependence of the spin inversion  $\langle \hat{S}_z^2 \rangle$  for different temperatures (indicated by the coloured squares). By fitting the expression  $\langle \hat{S}_z^2(t, T) \rangle - \langle \hat{S}_z^2(T)_{st} \rangle = \left( \langle \hat{S}_z^2(T = 2.7K) \rangle - \langle \hat{S}_z^2(T) \rangle_{st} \right) e^{-\Gamma t}$  to the data the relaxation rate  $\Gamma$  and the steady state of the inversion  $\langle \hat{S}_z^2 \rangle_{st}$  can be extracted. **b-c**, Steady state of the spin inversion  $\langle \hat{S}_z^2 \rangle_{st}$  obtained from the exponential fit. The spin and phonon system is initialized in a thermal equilibrium state at 2.7 K (1). By quenching the system to a lower temperature the spin temperature is higher than the phonon bath temperature, hence a non-equilibrium state is created (2). Next, the spin system exchanges energy with the bath at the rate  $\Gamma$  until the equilibrium state is reached (3). The red line presents a fit of the extracted steady state inversion to Equation (8.14). Note: This figure does not contain error bars since they are smaller than the size of data symbols.

### Collective Coupling Strength and Detuning

In Figure 8.3 the measured frequency shift of the resonator has been presented in  $\langle \hat{S}_z^2(t, T) \rangle$  by rearranging Equation (8.12). This can only be done accurately if the pre-factor  $\frac{g_N^2}{\Delta}$  is known. A problem that arises is that collective coupling strength  $g_N$  and the detuning  $\Delta$  are highly correlated in the resonator shift. To determine both requires to have information on one of the quantities. Several approaches to determine the detuning to the cavity can be pursued:

First, by increasing the temperature (spin and lattice) until an inversion close to  $\frac{2}{3}$  is reached, the spin ensemble decouples from the cavity mode (the dispersive shift  $\chi$  vanishes). This would be easily possible as the pulse tube of the ADR fridge generates a 2.7 K heat bath. Coupling the diamond to it would reduce the dispersive shift to approximately two percent. However, the used aluminum cavity loses its superconductivity already around 0.6 K. This not only reduces the cavity Q value tremendously but also alters its resonance frequency. By manufacturing the cavity out of bulk niobium-titanium one could circumvent this problem and provide a superconducting cavity up to the temperature of the pulse tube heat bath.

Second, by probing the cavity mode with a large number of photons,  $n_{\text{photon}} \gg n_{\text{spins}}$ , the dispersive interaction vanishes and one retrieves the bare cavity resonance frequency. If the bare cavity resonance is known the collective coupling strength  $g_N$  can be determined by fitting Equation (8.12) to the steady state frequency shift and the data can be presented in terms of  $\langle \hat{S}_z^2 \rangle$ . The so found coupling strength is given for each sample in Table 8.1. A cross check by calculating the collective coupling strength by the number of spins in the sample volume and the single spin coupling rate of the mode yields good agreement in comparison to the here presented method.

## 8.3. Temperature Dependence of the Relaxation Rate

By repeating the previous set of measurements for the diamond samples N1, E1, E2 and E3 (see Chapter 5 for details) the temperature dependence of the relaxation rate  $\Gamma_1 = 1/T_1$  can be analysed and compared. Figure 8.4 presents the temperature dependence of the relaxation rate in a double logarithmic plot for all samples.

Looking at the plot, it can be divided into two different regimes: The first for temperatures which are larger than the ground state energy splitting of the NV centre ( $T > \hbar\omega_s/k_B$ ) and the second consequently as the low temperature regime for temperatures below the energy splitting. The line shape of the high temperature regime suggests a linear dependence of the relaxation rate on temperature. This is

a clear signature of a direct single phonon process where either stimulated emission of a phonon via a spin decay or resonant phonon absorption is happening. A linear dependence on temperature comes from a process that needs the presence of phonons. Hence, it is directly proportional to their number which follows the Bose-Einstein distribution.

For the low temperature limit, the data suggests that the relaxation rate becomes independent of temperature and reaches a constant value. This plateau can be identified as the regime where all thermal phonons that match the NV transition energy are frozen out. Hence, the NV spin lattice relaxation here is governed by the spontaneous emission of a phonon into the vacuum state of that mode.

Putting all these processes together leads to same set of rate equations for the level occupations as already discussed in the theoretical treatment of spin lattice relaxation (see Section 1.3). The solution to this yields the following functional dependence of the relaxation rate on temperature. It is further used to fit the data in Figure 8.4 and extract the value for  $\Gamma_0$ :

$$\Gamma(T) = \Gamma_0(1 + 3\bar{n}(T)), \quad (8.15)$$

where  $\bar{n}(T)$  is the number of phonons at the spin transition energy  $\hbar\omega_s$ , following the Bose-Einstein distribution.

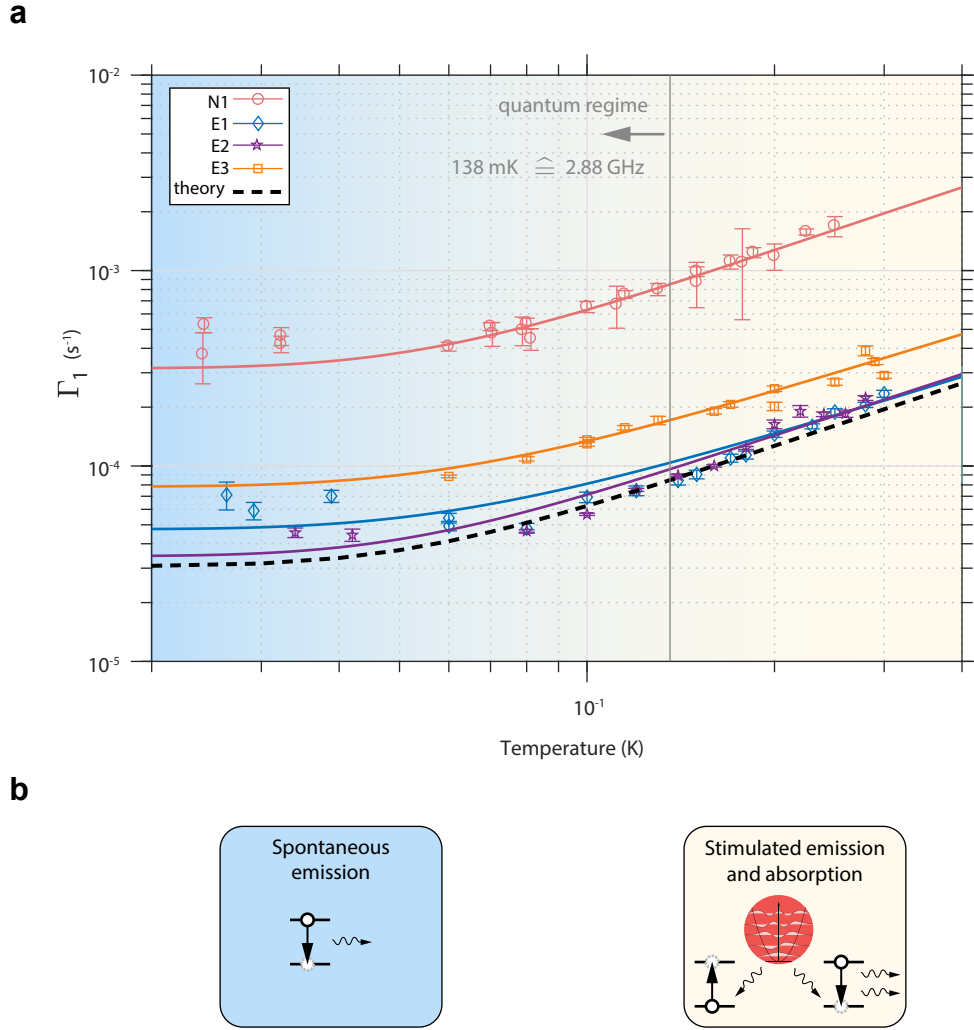


**Figure 8.4.: Temperature dependence of the relaxation rate.** **a**, The symbols and colours identify the different ensembles for which the spin lattice relaxation rate was determined as function of temperature. To each data set the expression  $\Gamma = \Gamma_0(1 + 3\bar{n})$  can be fitted to extract the constant of proportionality  $\Gamma_0$ . The lowest rate is obtained for the electron irradiated sample E2. Despite different initial nitrogen and resulting NV concentrations, E1 and E2 exhibit almost the same relaxation rate. In comparison, the sample N1 (neutron irradiated) has a relaxation rate that differs by more than one order of magnitude. The dashed line indicates the obtained result from the *ab initio* calculations. The low temperature regime where  $k_B T < \hbar\omega_s$  (light blue background) can be identified as the quantum regime where the phonon mode at the NV transition is not populated any more. There the decay is governed by a spontaneous emission of a phonon. In the high temperature limit ( $k_B T > \hbar\omega_s$ ) the relaxation rate shows a linear dependence on temperature which can be associated with a single phonon process - driven by the number of phonons present. This can be understood with the Bose-Einstein distribution, where phonons populate the energy mode corresponding to the NV transition. **b**, The two processes responsible for spin lattice relaxation of the NV centre: Spontaneous emission of phonons in the quantum limit and stimulated emission and absorption for temperatures above the transition energy.

Looking at the data in Figure 8.4, the lowest relaxation rate was measured for the sample E2 with the temperature independent rate  $\Gamma_0 \approx 3.5 \times 10^{-5} \text{ s}^{-1}$ , which corresponds to a remarkable long  $T_1$  time of 8 h. Whereas the shortest time is found for the sample N1 with a lifetime of approximately 1 h. A possible explanation for this large discrepancy in the relaxation time can be found by looking at the properties like NV density and lattice damages of the measured samples.

First, the samples N1 and E2 differ in their density of NV spins of 40 ppm and 13 ppm respectively. This would suggest that the relaxation process also depends on the density and hence on dipole interaction between individual NV spins. Estimating the dipole interaction of two neighbouring NV centres gives values between 100 kHz (E2, E3) and 500 kHz (N1, E1). However, the samples E1, E3 yield a similar relaxation rate within one order of magnitude but have the same difference in spin density as E1 with N1. From that one can conclude that the spin lattice relaxation process in this ensembles is independent of the spin density and solely determined by the relaxation properties of an individual spin.

Second, the main difference in the samples is the irradiation method for the creation of lattice vacancies. This can be divided in two different categories: neutron and electron irradiation. Sample N1 was irradiated with neutrons in the core of the in-house nuclear reactor with a total neutron flux density of approx.  $5 \times 10^{12} \text{ cm}^{-2}\text{s}^{-1}$ . In the relevant energy regime from 1 keV to 1 MeV a primary knock-on collision transfers a kinetic energy of 130 eV to 140 keV to a carbon nucleus. This causes a considerable large recoil of a single carbon atom and displaces further carbon atoms in the vicinity. The resulting damage cascade can have effects on the electronic properties of the diamond by trapping electrons or holes. A high dose neutron irradiation then may generate a region of disordered carbon with a diameter of roughly 45 Å. On the other hand, from the careful electron irradiation accompanied with simultaneous annealing it can be assumed, that less lattice damages are introduced in the crystal structure. The degree of lattice damage is directly linked to the speed of sound, which will be decreased by damages, and results in an increase in the density of states for phonons. Consequently, the coupling of the spin to the phonon vacuum mode is enhanced by an increase of the density of states at this frequency and results in a faster decay constant  $\Gamma_0$ . In this respect, determining  $\Gamma_0$  allows to draw conclusions on the density of states at the NV transition energy. In Table 8.1 the properties of the used samples are summarized, details on the sample preparation methods are given in Chapter 5.

Sample	N1	E1	E2	E3
NV (ppm)	40	40	13	10
N (ppm)	≤200	100	50	≤200
Irradiation type	n	e <sup>-</sup>	e <sup>-</sup>	e <sup>-</sup>
$\Gamma_0$ (s <sup>-1</sup> )	$3.17 \pm 0.10 \times 10^{-4}$	$4.76 \pm 0.26 \times 10^{-5}$	$3.47 \pm 0.16 \times 10^{-5}$	$7.86 \pm 0.60 \times 10^{-5}$
$g_N$ (MHz)	$6.62 \pm 0.20$	$9.11 \pm 0.58$	$5.88 \pm 0.20$	$2.85 \pm 0.19$
Irradiation energy (MeV)	0.1–2.5	2	2	6.5
Annealing temp. (°C)	900	800–1000	800–1000	750–900
Irradiation dose (cm <sup>-2</sup> )	$9.0 \times 10^{17}$	$1.1 \times 10^{19}$	$5.6 \times 10^{18}$	$1.0 \times 10^{18}$
Mass (mg)	19.2	44.6	22.6	10.8

**Table 8.1.: Sample characteristics.** Several samples were chosen with properties like different initial nitrogen and final NV concentration. This also results in a different collective coupling rate  $g_N$  to the resonator mode. An estimate for the residual nitrogen concentration  $[N]_{\text{initial}} - 2[NV]$  can be given with 120, 20, 24 ppm for N1, E2 and E3, respectively. From the data a strong dependence of the spontaneous emission rate  $\Gamma_0$  on the sample preparation can be observed. Details on NV creation of each sample can be found in Chapter 5. Table similar to ref. [42].

## 8.4. *Ab initio* Calculation of $\Gamma_0$

In this section the calculation of the constant of proportionality  $\Gamma_0$  from first principle studies is outlined. As there is a whole thesis written by Johannes Gugler concerning the density functional approach for calculating the relaxation rates, the author refers to this work and only conceptionally introduces the approach, as this thesis here covers the experimental part of determining  $\Gamma_0$ .

To derive a direct spin-phonon coupling the following mechanism is considered: The displacement of the lattice nuclei by phonons shifts the position of the electrons and leads to a change in the dipolar spin-spin interaction<sup>1</sup>:

$$\hat{H}_{\text{ss}} = -\frac{\mu_0 g_e^2 \mu_B^2}{4\pi} \frac{\left(3 \left(\hat{\mathbf{S}}_i \cdot \hat{\mathbf{r}}_{ij}\right) \left(\hat{\mathbf{S}}_j \cdot \hat{\mathbf{r}}_{ij}\right) - \left(\hat{\mathbf{S}}_i \cdot \hat{\mathbf{S}}_j\right)\right)}{|\mathbf{r}_{ij}|^3}, \quad (8.16)$$

with  $\mu_0$  as the vacuum permeability,  $g_e$  the electronic g-factor,  $\mu_B$  the Bohr-magneton,  $\hat{\mathbf{S}}_{i(j)}$  the spin vector and  $\hat{\mathbf{r}}_{ij}$  ( $\{\hat{\mathbf{S}}_n\}$ ) as the electron distance vector as a function of the ion position. In this low energy regime the displacements are small and allow an expansion of the dipole interaction to the first order. From this an interaction potential

<sup>1</sup>Nota bene: Here explicitly the dipolar interaction between two electrons within a single NV centre is considered and must not be confused with dipolar interaction among two distant NV centres.

$V_{s-ph}$  can be derived which can be used in Fermi's golden rule to derive the transition rates between the different spin states. A graphical illustration of the process is given in Figure 8.5.

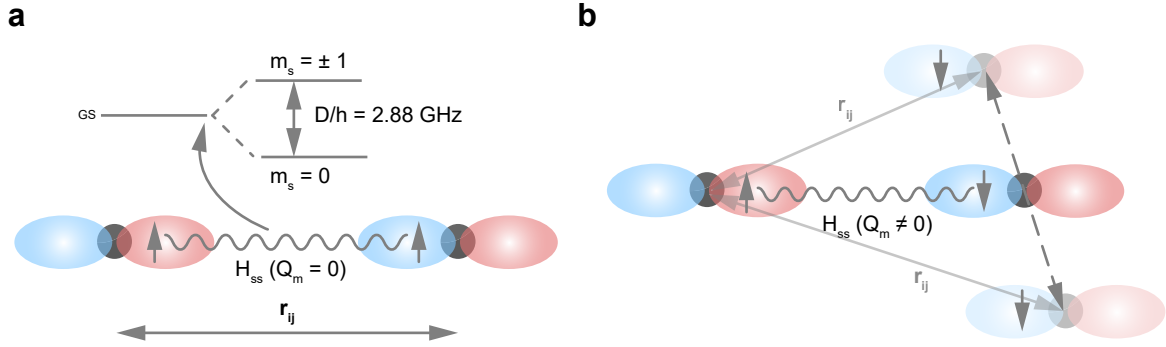


**Figure 8.5.: Spin-spin interaction of the electrons in a single NV centre.** **a**, In the static case without phonons in the system the displacement  $\{\mathbf{Q}_m\}$  of the nuclei is zero and the distance vector  $\mathbf{r}_{ij}$  does not change. However, the static spin-spin interaction (wiggly line) is responsible for the fine structure of the NV ground state. **b**, In the dynamic case the position of the electrons follow the position of the nuclei which is displaced by phonons. This coupling enables energy exchange between lattice phonons and the spin system. Image similar to ref. [115].

The response of the electrons was modelled by taking a Wigner-Seitz cell around the equilibrium position of the ion. In this region the electronic orbitals rigidly follow the movements of the nuclei. This model is used within density functional theory (DFT) calculations on a supercell containing 64, 128, and 512 lattice sites with a single NV centre. All numerical studies were performed with the Vienna Ab Initio Simulation Package (VASP) [116] using projector augmented wave pseudopotentials [117]. The calculation of the ionic equilibrium positions together with the ionic dynamics and the electronic wavefunctions then allows to determine a value for  $\Gamma_0$  from first principles. In Figure 8.4 the dashed black line presents the relaxation rate determined from the calculations with a value  $\Gamma_0 = 3 \times 10^{-5} \text{ s}^{-1}$ .

By comparing the experimental data to the theory the following statements can be inferred: First, the calculation presents the lowest relaxation rate in the plot in Figure 8.4 and sets a lower bound for  $\Gamma_0$  for NV centres in diamond. Furthermore, the calculation was performed with only one single NV centre in the supercell but still yields a value for the rate comparable to the electron irradiated samples E1 to E3. Once more the conclusion can be drawn that the relaxation process in a large ensemble is intrinsic to a single NV centre and not a collective effect. Second, looking at the results of the samples provided by Junichi Isoya (E1, E2), the following conjecture can be made: careful electron irradiation while simultaneously annealing results in



the creation of NV centres in diamond without introducing too many lattice damages that alter the density of states for phonons. A numerical analysis of the density of states, as plotted in Figure 8.6, shows that any alteration of the lattice in terms of a substitutional nitrogen atom or a NV centre shifts the density of states to lower frequencies and, hence, reduces the speed of sound.

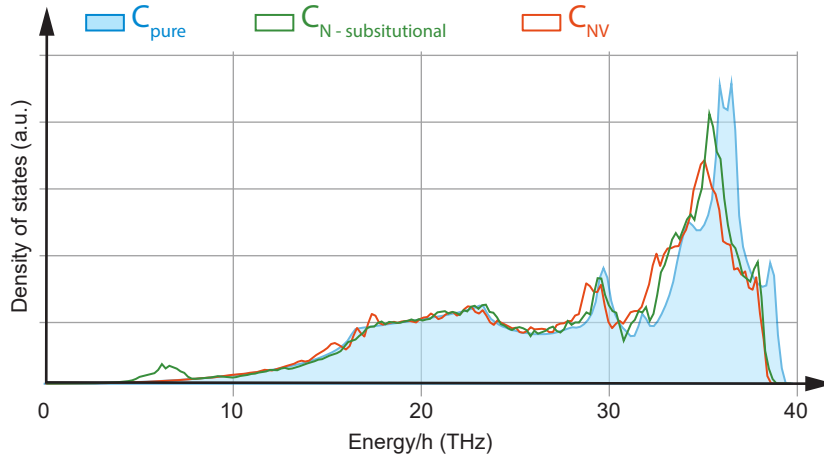


**Figure 8.6.: Phonon density of states.** Numerical calculation of the phonon density of states for different lattice situation: Perfect diamond crystal consisting of only carbon atoms (light blue area). Lattice with a substitutional nitrogen atom (green line). Substitutional nitrogen with adjacent lattice vacancy (red line). From a comparison it can be seen that any alteration of the pure lattice structure results in a shift of the phonon density of states towards lower energies. The calculation was performed on a diamond supercell containing 64 lattice sites. Illustration similar to ref. [115].

## 8.5. Conclusion and Outlook

To conclude, the question of how an excited spin in a solid transfers energy to surrounding lattice environment has been answered in this chapter. As spin lattice relaxation provides the fundamental limit for coherence of a quantum system, understanding these processes is important. This work presents the first low temperature study of the NV relaxation process and the observation of spontaneous emission into the phononic vacuum. Remarkably, the low phononic density of states at the NV transition energy allows the spin inversion to survive over macroscopic time scales of up to 8 h. So far this number was not known and this work presents the first experimental data together with an *ab initio* study based on density functional theory.

Moreover, a technique was presented that allows to measure the spin relaxation over such long time scales with initializing the whole ensemble just once. Compared to

the usual methods of electron spin resonance, here a cavity quantum electrodynamics scheme was utilized, where the spin ensemble is in the strong coupling regime. This allows to read out the inversion of a large spin ensemble and reach sensitivities beyond conventional methods.

Furthermore, effects like amplitude bi-stability in such ensembles [118] are scaled with the longitudinal spin lattice relaxation rate and define the time-scales of such effects. On the other hand, as the relaxation rate is so low, that it plays a negligible role for short time-scales related to the dynamics of coherent interference effects like super radiance [119].

## 9. Coupling of Remote Spin Ensembles

This part is based on the research paper:

- **Coherent Coupling of Remote Spin Ensembles via a Cavity Bus**  
T. Astner, S. Nevlacsil, N. Peterschofsky, A. Angerer, S. Rotter, S. Putz, J. Schmiedmayer, and J. Majer  
*Phys. Rev. Lett.* **118**, 140502 - Published 5 April 2017

The scientific community has invested a great amount of research into the NV centre as possible candidate for quantum information tasks or as transducer between the optical and the microwave domain. Several experiments report entanglement of single nitrogen vacancy centres over macroscopic and microscopic distances. For example the entanglement of two NV spins separated by three meters [120, 121] is achieved via a local spin-photon entanglement and consecutive joint photon measurement. In contrast to that, the dipole-dipole interaction between two single emitters [122] has been used to directly entangle them over a distance of a few nanometres. All these efforts work towards the goal of harnessing solid-state spin qubits and the entanglement between them for the creation of spin based quantum logic gates, quantum registers or general applications in quantum information science. Entanglement between such qubits and across long distances opens the door for large-scale quantum networks to share private information.

In this chapter an experiment is presented that demonstrates the coherent coupling of two large spin ensembles over a macroscopic distance. To do so, each ensemble is coupled to the same mode of a superconducting coplanar waveguide resonator. Via transmission spectroscopy the coherent coupling between the distant ensembles and the cavity mode can be directly observed by bright and dark collective multiensemble states. Furthermore, the coupling to the mode is enhanced as the number of spins is doubled. By moving the system to the dispersive limit of cavity QED a transverse ensemble-ensemble coupling is established by virtual photons in the resonator. The resonator then acts as a quantum bus that mediates the interaction between the distant ensembles - a path towards quantum information transfer and entanglement between remote large scale spin ensembles.

## 9.1. Two Ensembles in a Cavity

In contrast to previous experiments, where a single ensemble had been coupled to the fundamental  $\lambda/2$  resonance of a coplanar waveguide resonator [20, 21, 93], the coupling of two distinct ensembles requires some slight modifications to the set up.

First, in contrast to a  $\lambda/2$  resonator the centre conductor has been adjusted to support a full wave  $\lambda$  resonance around 3 GHz. This is necessary as the resonator must have two antinodes ( $\lambda/4$  and  $3\lambda/4$ ) of the oscillating magnetic field to host the two diamond samples. The resonator shown as photograph and illustration in Figure 9.1 has a meandered centre conductor. This ensures a high overlap of the oscillating magnetic field generated by the resonator with the NV spins. The samples (D1 and D2) are placed with their polished (001) surfaces onto the superconducting chip (for further details see Chapter 5). If magnetic fields are applied only in the (001) diamond plane, each sample has only two magnetically distinguishable NV sub-ensembles. They are further illustrated in Figure 9.2 and Figure 9.3 panel a.

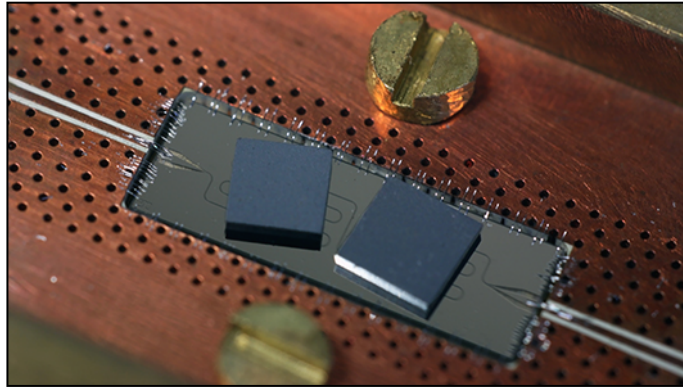


**Figure 9.1.: Photograph of two diamonds on the resonator.** The samples are placed on the resonator with a relative angle between them of  $24.2^\circ$ . The resonator (grey rectangle) has a meandered centre conductor to ensure a high overlap of the oscillating magnetic field with the diamond samples. On the edges the chip is bonded with aluminum bond wires to the surrounding PCB (copper). The whole set-up is mounted inside a gold-plated brass box.

Second, with respect to a global coordinate given by the 3D Helmholtz coils, the samples have a relative angle of  $24.2^\circ$  between them. This arrangement has been chosen to ensure that the NV principal axes of the different NV sub-ensembles do not coincide. The angle between the diamonds does not have to have a precise value, as long as the two principal axes point in a unique direction. Identifying each sub-ensemble of the two diamonds with the colour code in Figure 9.2, the individual directions of the sub-ensembles are:

- Diamond 1:  $60.1^\circ$  (dark blue, no. I) and  $150.1^\circ$  (red),
- Diamond 2:  $35.9^\circ$  (orange, no. II) and  $125.9^\circ$  (light blue).

The different directions are drawn in the global coordinate system shown in Figure 9.2.

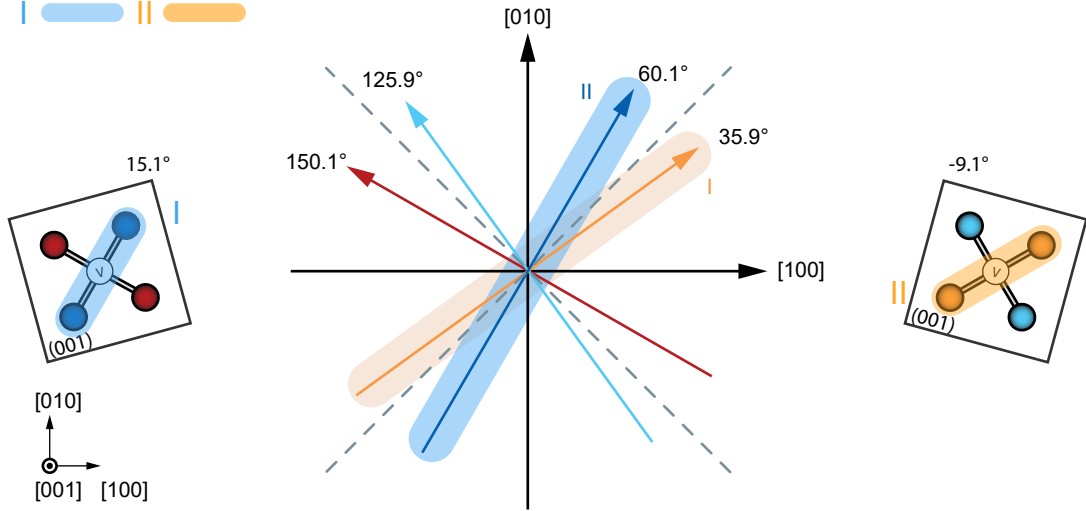


**Figure 9.2.: Diamond sub-ensembles.** Placing the crystals under a different angle onto the resonator chip results in four magnetically distinguishable spin ensembles. The vacancy is marked with the N in a circle whereas the nitrogen next to it is illustrated with the coloured orbs. Depending on where the nitrogen atom sits, four magnetically different sub-ensembles per crystal can be identified. Limiting the external fields to the (001) plane reduces the number of sub-ensembles to two. For the experiment two directions are selected and marked with I and II (blue and orange shaded area).

Next, the spin Hamiltonian in Equation (1.1) can be diagonalized for each sub ensemble by projecting the external magnetic field vector  $\mathbf{B}_{\text{ext}}$  onto the individual axes. In Figure 9.3 the dependence of the  $m_s = 0 \rightarrow m_s = \pm 1$  transition energies on the magnitude and angle of the external magnetic field is plotted.

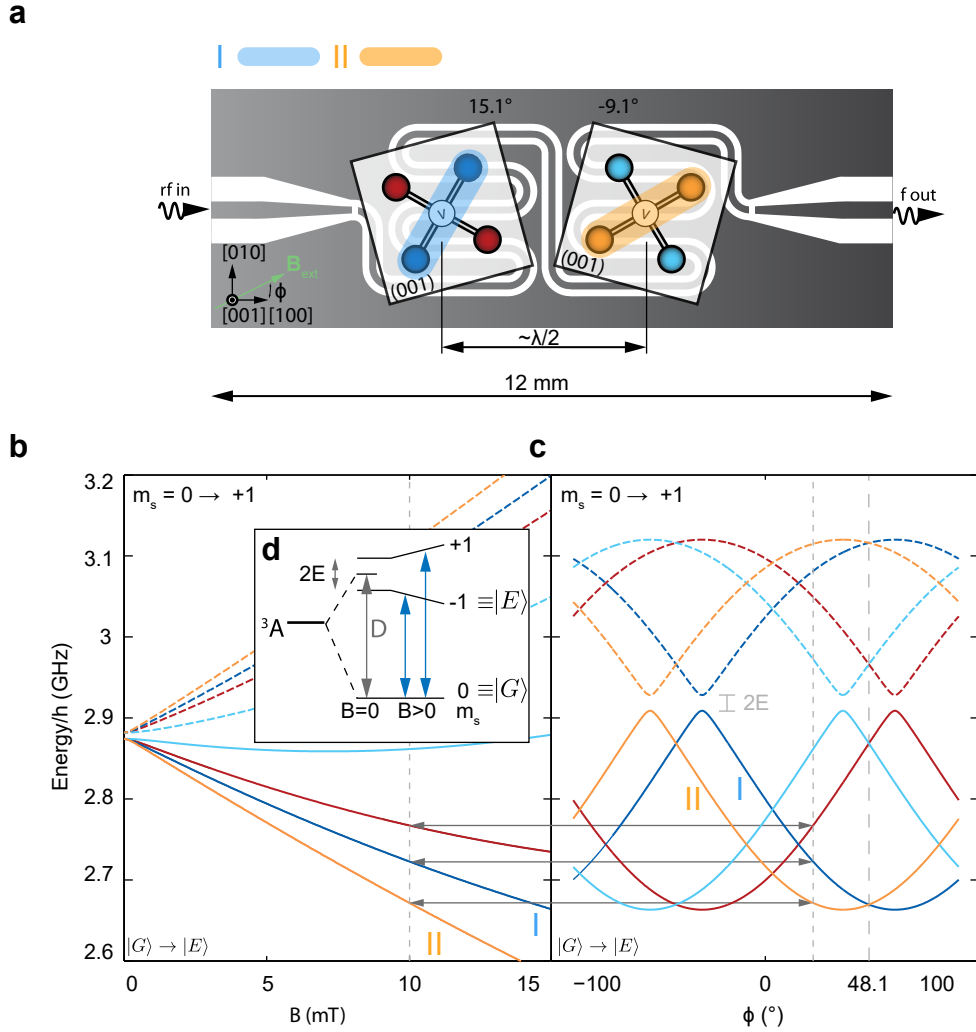


**Figure 9.3.: Tuning of transition energies.** **a**, Illustration of two diamonds bonded onto a superconducting resonator. The samples are placed on the chip with a relative angle of  $24.2^\circ$ . In the experiment the coupling between ensemble I and II is realized via photons in the resonator. **b-c**, Transition energies plotted as function of the external magnetic field amplitude and angle applied in the (001) diamond plane and parallel to the resonator surface. The transition energies can be calculated by diagonalizing the spin Hamiltonian with respect to the direction and amplitude of the external field. At  $48^\circ$  the transition energies of the remote ensembles I and II are degenerate. The anticrossings (dashed and solid coloured lines) corresponds to the strain field parameter  $E$  which mixes the  $m_s = -1$  and the  $m_s = +1$  states. **d**, The inset presents the ground state spin triplet of the NV centre. The relevant  $m_s$  states are labelled with  $|G\rangle$  and  $|E\rangle$ . Illustration similar to [41].

As there is only a single  $m_s = 0 \rightarrow m_s = -1$  transition of each diamond important for the following experiment they are labelled with  $|G^I\rangle \rightarrow |E^I\rangle$  (dark blue) and

$|G^{II}\rangle \rightarrow |E^{II}\rangle$  (orange), respectively. By looking at Figure 9.3 one can see that at a field angle of  $48.1^\circ$ , the transition energies of the individual diamonds are degenerate. By keeping the angle constant, the magnitude of the magnetic field determines the frequency (energy) at which the degeneracy appears.

## 9.2. Two Ensembles Coherently Interacting with a Cavity Mode

The first experiment demonstrates the coherent coupling of two spatially separated ensembles to a single mode of radiation. In a transmission spectroscopy this effect is directly observed as the coupling strength to the mode increases if the distant ensembles are degenerate.

### 9.2.1. System Hamiltonian

The simplification to two single transitions allows to construct an effective model based on a modified Tavis-Cummings Hamiltonian. With the already introduced collective operators (see Section 2.2), the Hamiltonian reads

$$\begin{aligned} \hat{H}_{\text{eff}} = & \hbar\omega_c \hat{a}^\dagger \hat{a} + \hbar\omega_I \hat{S}_I^z + \hbar\omega_{II} \hat{S}_{II}^z + \hbar g_0 \left( \hat{a} \hat{S}_I^+ + \hat{a}^\dagger \hat{S}_I^- \right) \\ & - \hbar g_0 \left( \hat{a} \hat{S}_{II}^+ + \hat{a}^\dagger \hat{S}_{II}^- \right). \end{aligned} \quad (9.1)$$

The collective coupling strength of a sub-ensemble is given by  $g_I = \sqrt{\sum_{j=1}^{N_I} |g_0|^2}$ , which is the typical  $\sqrt{N}$  enhancement [67]. For the second sub-ensembles all operators can be defined similarly. The antinodes of the magnetic field generated by the resonator have inverted signs. This reflects in the Hamiltonian with the negative sign of  $g_{II}$ .

Depending on the magnitude and angle of the external magnetic field, either one or both sub-ensembles can be brought into resonance with the cavity mode. This is further illustrated in Figure 9.4.

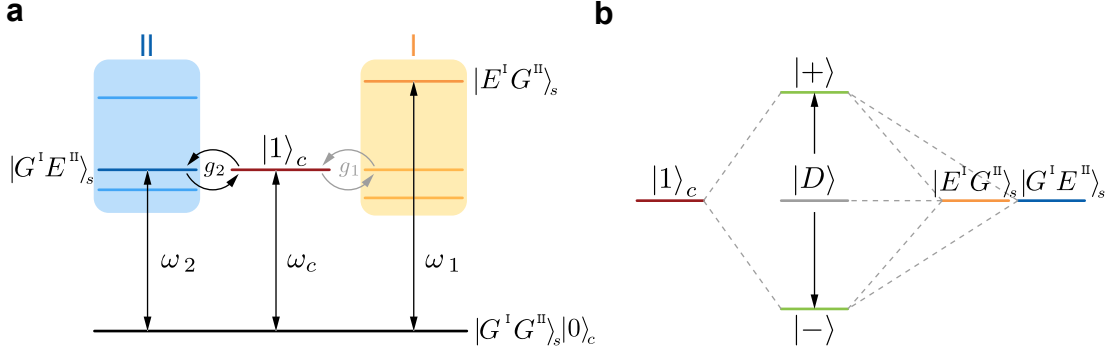


**Figure 9.4.: Resonant coupling scheme.** **a**, With the angle and amplitude of the external magnetic field either one or both ensembles can be tuned through resonance with the cavity. The cavity photon states are given by  $|0\rangle_c$  and  $|1\rangle_c$ . The colour shaded boxes illustrate the range of energy tuning by the magnetic field. On resonance the ensembles are coupled to the cavity mode with  $g_{1,2}$  **b**, If both ensembles are simultaneously in resonance with the cavity the system hybridizes in two normal modes and a dark state.

At the point of the three-fold degeneracy ( $\omega_I = \omega_{II} = \omega_c$ ), the eigenstates in the single excitation manifold have the form

$$|\pm\rangle = \frac{1}{\sqrt{2}g_{\text{col}}} \left[ \pm g_{\text{col}} |G^I G^{II}\rangle_s |1\rangle_c - (g_I |E^I G^{II}\rangle_s - g_{II} |G^I E^{II}\rangle_s) |0\rangle_c \right], \quad (9.2)$$

and

$$|D\rangle = \frac{1}{g_{\text{col}}} (g_{II} |E^I G^{II}\rangle_s + g_I |G^I E^{II}\rangle_s) |0\rangle_c. \quad (9.3)$$

Here the collective excited state of the first ensemble,  $|E^I\rangle = 1/N \sum_{j \in I} |g \dots e_j \dots g\rangle$ , is introduced in the form of a Dicke state and similar for the second ensemble. The state  $|G\rangle = 1/N \sum_{j \in I} |g \dots g_j \dots g\rangle$  refers to the ground state of each ensemble.

From the form of the states it can be seen that the system hybridizes into two polariton modes and a dark state. The polariton modes are the symmetric/antisymmetric superposition of the Dicke states of each ensemble and a photon excitation in the cavity. A single excitation thus is shared between the ensembles and the cavity mode. The third state is a symmetric superposition of an excitation shared just between the ensembles and does not have a cavity mode component. Since  $g_I$  and  $g_{II}$  have opposite signs, the symmetric superposition of the individual Dicke states becomes a dark state.

The corresponding eigenenergies of the are given by

$$E_{\pm} = \hbar\omega_c \pm \hbar\sqrt{g_I^2 + g_{II}^2}, \quad \text{and} \quad (9.4a)$$

$$E_D = \hbar\omega_c, \quad (9.4b)$$



which are similar to the energies of a 3-level Jaynes Cumings model (compare to Equation (2.22)).

### 9.2.2. Transmission Spectroscopy

The first set of measurements consists of transmission spectroscopy as function of the magnitude of the external field, while keeping the angle constant. This allows to tune each individual ensemble in resonance with the cavity mode. At the degeneracy, parameters like the individual coupling rate and the polariton line-width can be deduced from the avoided crossing. Experimentally this is done with a field angle set to  $79^\circ$  ( $23^\circ$ ) and tuning of the central spin line through resonance with the cavity. The angles are chosen such that the other spin transitions and doesn't influence the line-shape at the avoided crossing.

The results of the different spectroscopy measurements are presented in Figure 9.5 with the central spin lines in red and the coupled eigenvalues in dark blue. The vertical dashed line marks the avoided crossing with the corresponding transmission scattering amplitude  $|S_{21}|^2$  shown in panel b. Fitting an expression similar to Equation (7.1) to the measured transmission scattering amplitude  $|S_{21}|^2$ , the collective coupling rates have values of:  $g_I/2\pi = 7.5 \pm 0.1$  and  $g_{II}/2\pi = 5.6 \pm 0.1$  MHz. The polariton line-widths are found to be  $\Gamma_I/2\pi = 2.45 \pm 0.18$  and  $\Gamma_{II}/2\pi = 2.28 \pm 0.16$  MHz (half-width at half-maximum).

Finally, this measurement shows that each individual ensemble fulfils the necessary conditions that the collective coupling rate is larger than the cavity loss rate and spin dephasing rate.

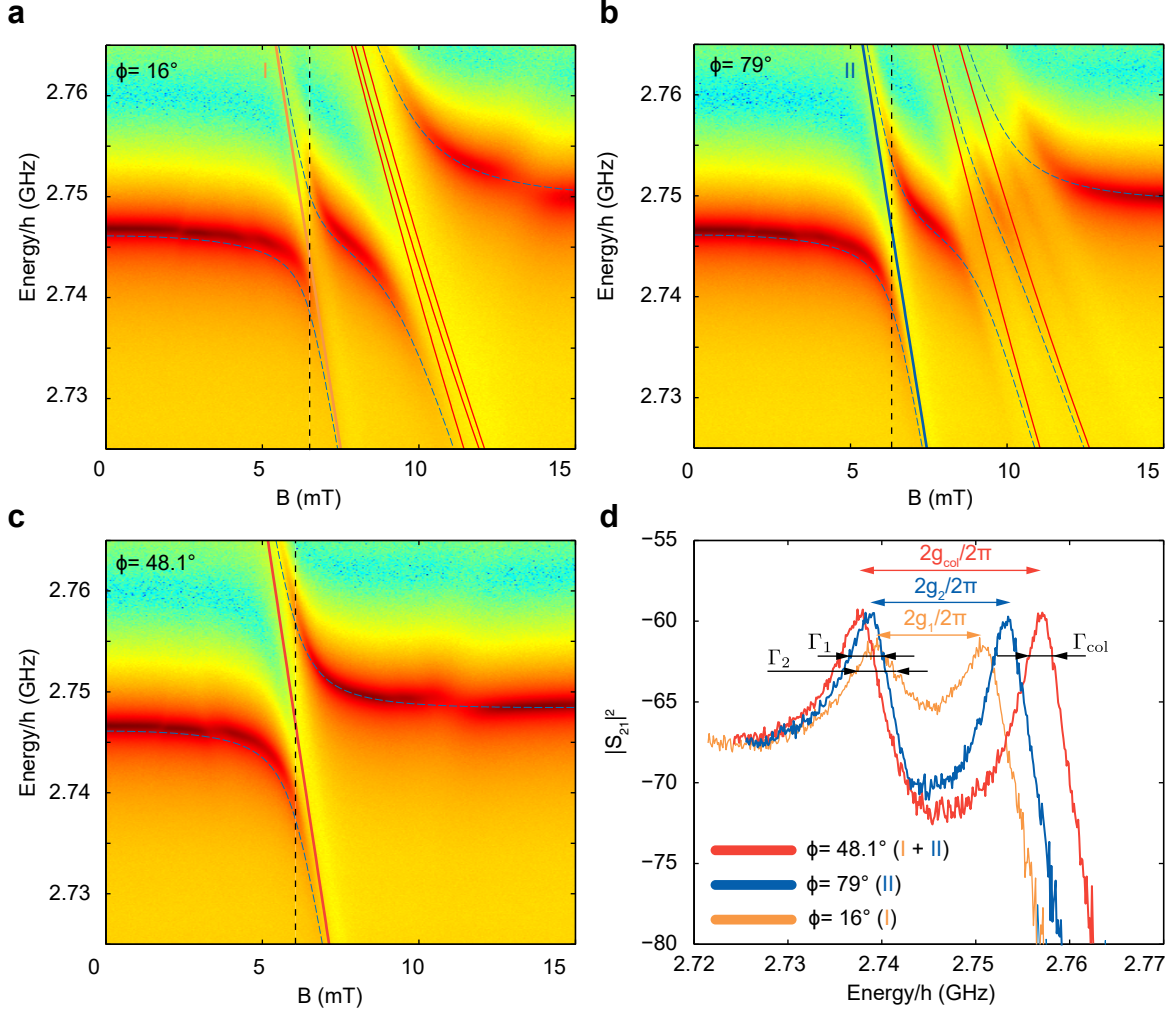


**Figure 9.5.: Transmission spectroscopy.** **a,b,** Applying the magnetic field under an angle of  $16^\circ$  ( $79^\circ$ ) brings ensemble I (II) into resonance with the cavity at a field amplitude of around 6 mT. There the normal mode splitting of a single ensemble spin transition with the cavity is observed. Increasing the field amplitude further results in a second avoided crossing above 10 mT, which is created from other spin transitions in the vicinity. As they are not aligned the avoided crossing is significantly broadened and washed out. **c,** Applying the magnetic field under an angle of  $48.1^\circ$ , the spin transitions of ensemble I and II are perfectly aligned and can be tuned through resonance with the cavity mode. The measured normal mode splitting is larger than in the individual ensemble case. In this surface plot at around 12 mT a weak coupling of the  $^{13}\text{C}$  hyperfine interaction can be observed. **d,** Cavity transmission amplitude measured at the avoided crossing (data corresponds to the dashed vertical lines in **a-c**). From the data the coupling strength of the individual ensembles as well as the collective coupling of both ensembles to the mode can be determined. Additionally, the polariton line-width can be resolved from the measured features.

The second set of measurements deals with an angle resolved transmission spectroscopy with the magnitude of the external field vector set constant to a value of 6.1 mT. This ensures that at an angle of  $48.1^\circ$  both ensembles and the cavity mode are in resonance. The measurement displayed in Figure 9.6 has three different features. At an angle of  $23^\circ$  and  $79^\circ$  the strong coupling of each ensemble to the resonator mode is observed. This confirms the parameters derived from the spectroscopy at constant angle. In addition to that, at the angle of  $48.1^\circ$  both ensembles and the cavity are degenerate. The observed level splitting is much larger than of each individual ensemble and the cavity mode. A fit to the transmission data results in a collective coupling strength of  $g_{\text{col}}/2\pi = 9.6 \pm 0.1\text{MHz}$  and a decay rate of the polariton modes of  $\Gamma_{\text{col}}/2\pi = 1.49 \pm 0.07\text{MHz}$  (HWHM). Comparing the collective polariton line-width to the individual ones shows a significant reduction by almost a factor 1/2 through the cavity protection effect [87, 123, 124].

Furthermore, the measured coupling rate is in good agreement with the prediction  $g_{\text{col}} = \sqrt{g_{\text{I}}^2 + g_{\text{II}}^2}/2\pi \approx 9.36\text{MHz}$ . At this point the two ensembles behave as single giant spin ensemble coherently interacting with the resonator mode.

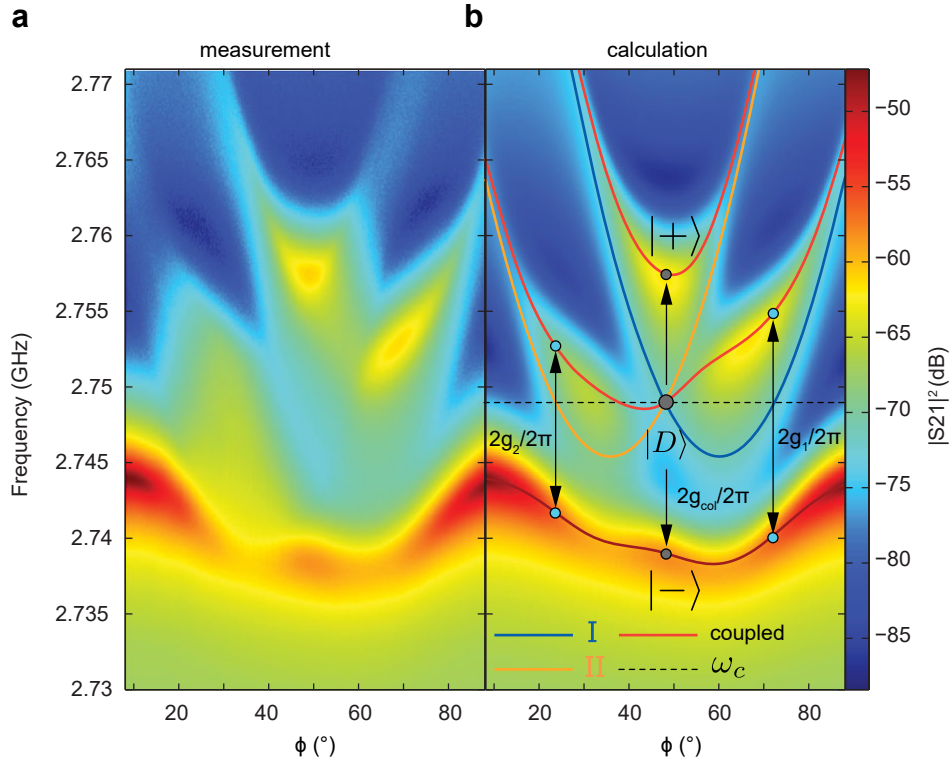


**Figure 9.6.: Angle resolved transmission spectroscopy.** **a**, Measurement data of an angle resolved transmission spectroscopy at a constant field amplitude of 6.1 mT. In the data the system parameters and information obtained by constant angle spectroscopy are confirmed. But in addition to that, the transition from the individual single ensemble polariton modes to the collective polariton mode at  $48.1^\circ$  is observed. In the centre of the normal mode splitting  $|\pm\rangle$  the dark state  $|D\rangle$  emerges. **b**, Using the parameters of the system for a numerical calculation shows that the theoretical model is able to capture all essential features of the measurements. In this plot the uncoupled bare eigenenergies are presented as solid orange and blue lines, whereas the coupled eigenenergies are given in red. At  $48.1^\circ$  the state  $|D\rangle$  has no cavity part in the eigenvector and, hence, is a dark state that does not appear in the spectroscopy. The dashed horizontal line represents the unperturbed cavity resonance. Figure taken from [41]

With the now experimentally determined coupling rates, the Hamiltonian in Equation (9.1) can be numerically diagonalized for all combinations of magnetic field amplitudes and angles. In Figure 9.6 panel b the eigenenergies obtained from a numerical diagonalization of the Hamiltonian are plotted in red. The polariton modes at the degeneracy point are labelled with  $|+\rangle$  and  $|-\rangle$ . The unperturbed energies of the cavity and the spin ensembles are shown as dashed grey lines. At the threefold degeneracy point of the system the emerging state is labelled with  $|D\rangle$ . As this dark state is a fully symmetric state, but  $g_I$  and  $g_{II}$  have opposite sign, the transition to

this state is forbidden because the cavity exhibits an asymmetric system drive. In the experimental data this is observed by a disappearance of the spectroscopy signal at the position of the dark state.

The presented experimental data presents the coherent coupling of two distant ensembles with the cavity. An effect directly observable in the transmission spectrum with the appearance of a dark resonance and the characteristic scaling of the collective coupling. Although the two ensembles differ significantly in their number of spins (collective coupling strength) and line-width the collective cooperative coupling to the common cavity mode is robust.

### Numerical Calculation of the Transmission Spectrum

With the parameters of each ensemble determined from transmission spectroscopy the transmission spectrum in the steady state can be calculated with standard input-output formalism [70, 125]. The dissipation channels like individual line-width of the ensembles are introduced as complex frequency parts in the Hamiltonian. In matrix form this can be expressed as<sup>1</sup>

$$\hat{H} = \hbar \begin{pmatrix} \omega_c + i\kappa & g_{\text{I}} & g_{\text{II}} \\ g_{\text{I}} & \omega_{\text{I}} + i\gamma_{\text{I}} & 0 \\ g_{\text{II}} & 0 & \omega_{\text{II}} + i\gamma_{\text{II}} \end{pmatrix}. \quad (9.5)$$

If in addition a probe term with frequency  $\omega_p$  is introduced, the cavity transmission matrix can be calculated with

$$T = \text{Tr} [(\omega_p 1_3 - \hat{H})^{-1}]. \quad (9.6)$$

In the experiment  $1 \times 10^{-6}$  photons/spin are circulating in the resonator, justifying the limitation of the problem to the single excitation manifold and calculating the transmission matrix with the Hamiltonian in Equation (9.5). Comparing the calculation of the transmission data shown in Figure 9.6 panel b to the measurement shows good qualitative agreement. All important features like polariton modes and the dark state are fully captured in the numerical diagonalization of the Hamiltonian.

---

<sup>1</sup>In the numerical calculation the  $m_s = 0$  to  $m_s = \pm 1$  transitions of of all sub-ensembles (2 diamonds, 4 sub ensembles each, 16 transitions in total) were incorporated in the matrix. Therefore, the models allows to calculate also solutions for magnetic fields out of the (001) crystal plane. An additional global Fano-phase factor was used to reproduce the full spectrum of the transmission.

## 9.3. Transverse Coupling of Two Ensembles

Up to this point the experiment has shown the hybridization of the two ensemble resonator system. It showed that two macroscopic spin ensemble, though spatially separated, can coherently interact with the common resonator mode. In the next experiment presented here, a so called transverse ensemble-ensemble coupling is realized with the exchange of virtual rather than real photons. This coupling is realized in the dispersive limit of cavity QED - spin transitions and cavity mode have a detuning larger than the coupling rate. Hence, cavity induced loss mechanisms can be avoided - allowing for the use of a fast cavity and enables quick probing of the system.<sup>1</sup> In contrast to that, pulses aimed at the ensembles are not in resonance with the cavity and are thus not limited in speed by the resonator's quality factor [72].

### 9.3.1. System Hamiltonian

To achieve the coupling via virtual photons it is necessary to avoid excitations in the resonator. Therefore, both ensembles have to be far detuned from the resonator  $|\Delta_{I,II}| = |\omega_c - \omega_{I,II}| \gg g_{I,II}$ . In the same way as already introduced in Section 2.1, an effective Hamiltonian can be found by adiabatically eliminating the resonant interaction with the transformation

$$\hat{U} = \exp \left[ \frac{g_I}{\Delta_I} (\hat{a}^\dagger \hat{S}_I^- - \hat{a} \hat{S}_I^+) + \frac{g_{II}}{\Delta_{II}} (\hat{a}^\dagger \hat{S}_{II}^- - \hat{a} \hat{S}_{II}^+) \right]. \quad (9.7)$$

Applying the unitary transformation on the Hamiltonian, this yields up to the second order in the small parameters  $g_{I,II}/\Delta_{I,II}$

$$H_U = \hbar \left( \omega_c + \chi_I \hat{S}_I^z + \chi_{II} \hat{S}_{II}^z \right) \hat{a}^\dagger \hat{a} + \frac{\hbar}{2} \left( \tilde{\omega}_I \hat{S}_I^z + \tilde{\omega}_{II} \hat{S}_{II}^z \right) + \hbar U \left( \hat{S}_I^- \hat{S}_{II}^+ + \hat{S}_{II}^- \hat{S}_I^+ \right). \quad (9.8)$$

with  $\tilde{\omega}_I = \omega_I + \chi_I$  and similar for the second ensemble.

Here in this nonresonant case, the cavity mode experiences a frequency shift of  $\chi_{I,II}$ , depending on the state of the ensemble  $S_{I,II}^z$ . The second term in the Hamiltonian denotes the Lamb shifted [126] spin transitions due to the presence of virtual photons [127]. In the last part, an effective transverse ensemble-ensemble coupling is mediated

---

<sup>1</sup>Nota bene: The term 'fast' cavity here refers to a cavity with highly transparent mirrors. A photon leaves the cavity after a few circulations and can be detected. This must not be mistaken with the term 'bad' cavity, which refers to a cavity with high internal losses - an in general unwanted property.

exchange of virtual photons at the rate  $U = (g_I g_{II}/2) (1/\Delta_I + 1/\Delta_{II})$ . This transverse coupling is only effective for,  $\tilde{\omega}_I = \tilde{\omega}_{II}$ , the case if both ensemble transitions are in resonance. On the other hand, the coupling can be effectively turned off by tuning the transitions out of resonance,  $|\tilde{\omega}_I - \tilde{\omega}_{II}| \gg U$ .

At the degeneracy point the resulting eigenstates are a superposition of the single ensemble Dicke states and have the form

$$|A\rangle = \frac{1}{g_{\text{col}}} (g_{II}|G^I E^{II}\rangle_s - g_I|E^I G^{II}\rangle_s), \text{ and} \quad (9.9)$$

$$|S\rangle = \frac{1}{g_{\text{col}}} (g_I|G^I E^{II}\rangle_s + g_{II}|E^I G^{II}\rangle_s). \quad (9.10)$$

This off resonant coupling scheme and the resulting states is further graphical illustrated in Figure 9.7.

Plugging in the system parameters derived in the previous measurements the expected transverse coupling rate is  $U/2\pi = g_I g_{II}/2\pi\Delta \approx 2.2\text{MHz}$ , with  $\Delta$  as the detuning of both ensembles to the cavity mode.

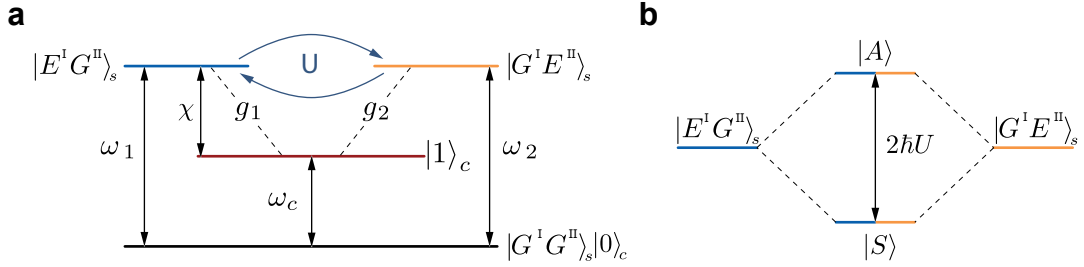


**Figure 9.7.: Dispersive coupling scheme.** **a**, Each ensemble is dispersively coupled to the cavity mode. In this scheme the ensembles (orange and blue) can be tuned through resonance. A coupling between them is established via the exchange of virtual photons in the resonator mode at the rate  $U$ . **b**, On resonance two new states emerge. A symmetric and antisymmetric superposition of coupled individual ensemble states.

### 9.3.2. Dispersive Spectroscopy

This set of measurements deals with a spectroscopy in the dispersive regime to experimentally show the transverse coupling between the remote ensembles via virtual photons in the resonator. Experimentally the dispersive regime can be reached by tuning the magnitude of the external magnetic field such that the spin transitions and the cavity are nonresonant. During the experiment a detuning of  $|\Delta_{I,II}| = |\omega_c - \omega_{I,II}| > g_{\text{col}} \geq 12\text{MHz}$  was maintained.

As illustrated in Figure 9.8, by applying strong drive tone (green line) on a spin transition, a fraction of the ensemble is brought into a statistical mixture. This changes the the expectation value  $\langle S_z \rangle$  and exhibits the frequency change proportional to  $\chi_{\text{I,II}} = g_{\text{II}}^2/\Delta_{\text{I,I}}$ . The resulting cavity shift is monitored by measuring the cavity transmission with a VNA (red line).



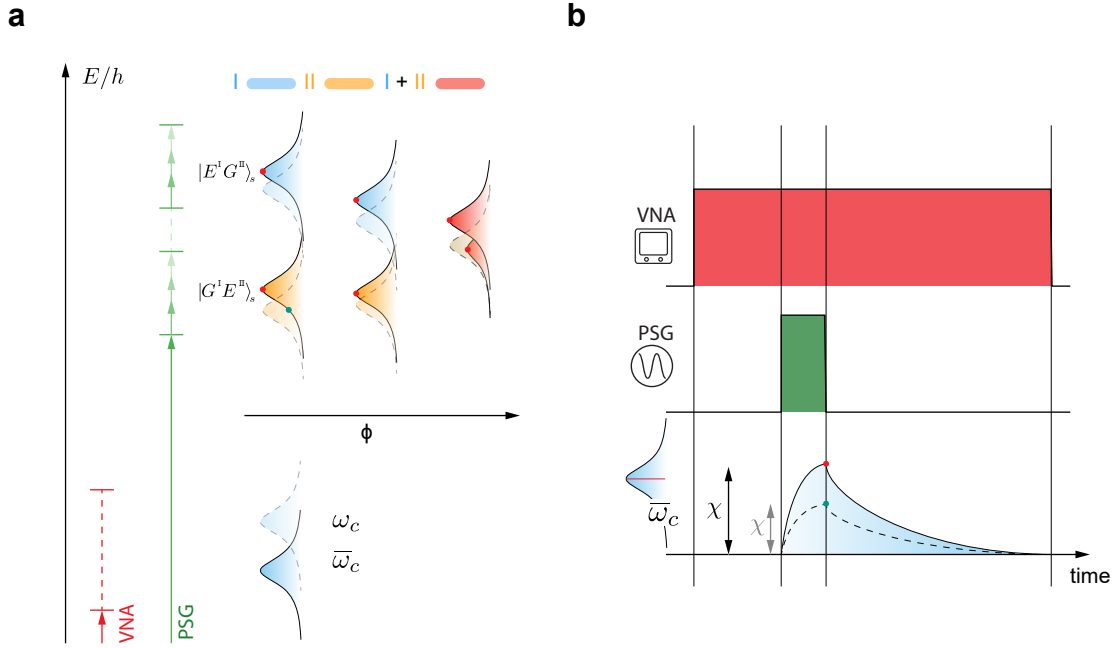


**Figure 9.8.: Dispersive spectroscopy technique.** **a**, The resonator mode and the spin transitions are illustrated in the energy diagram with  $\omega_c$  and  $\omega_{I,II}$ , respectively. Both spin transitions are far detuned from the cavity mode. With a probe signal generated by a VNA the cavity resonance is determined continuously (red arrow) A strong microwave drive injected into the resonator is stepped over the spin transitions (green arrow, label PSG) and brings a fraction of the ensemble in a statistical mixture. A feedback is created on the cavity mode ( $\bar{\omega}_c$ ) by changing the spin population in the ground state and the resonance frequency shifts by  $\chi$  towards  $\omega_c$  and directly resembles the spin feature. Depending on the detuning of the drive to the central spin line, the resonance of the cavity mode experiences a different shift (red and green dots on the orange peak - compare also to **b**) In the initial configuration the spin transitions of ensemble I and II are not in resonance but shifted in energy due to dispersive interaction with the resonator mode (dashed versus solid lines). By changing the direction of the external magnetic field the spin transitions can be tuned into resonance. In resonance the individual spin states vanish and the system couples to two normal modes. One of them as a bright state (red peak with high amplitude) and a dark state (indicated as red peak with low amplitude). **b**, Measurement and timing sequence. By operating the system in the dispersive limit the cavity resonance can be continuously monitored. After applying a strong pump pulse at a certain frequency on the spin transition the change in the cavity resonance is measured. From that data the relative resonance shift is determined with respect to the frequency of the drive.

To retrieve the total spin line-shape via dispersive spectroscopy, the measurement sequence has to be repeated several times with a different pump tone frequency. With this measurement procedure the position of the spin transitions can be tracked with respect to the angle of the external magnetic field. The results are plotted in Figure 9.9

where the resonance of both ensemble occurs under an angle of  $48.1^\circ$ . As the dispersive spectroscopy is rather tedious, the full measurement has been performed only for a certain number of field angle values, where the resonances  $\omega_{I,II}$ , extracted from a fit to the dispersive line-shape, are marked with the red dot and black error bars.

The NV centres in this ensemble have an inhomogeneous frequency distribution. Previous work showed [92] a q-Gaussian line shape with the determined dimensionless parameter  $q = 1.389$ . In the dispersive spectroscopy the following function is fit to the data sets

$$L(\omega) = b + I \left[ 1 - (1 - q) \frac{(\omega - \omega_{I,II})^2}{a} \right]^{\frac{1}{1-q}}, \quad (9.11)$$

where  $L(\omega)$  is related to a Tsallis distribution. The q-parameter is a measure for how fast the tails of the distribution fall off, while the parameter  $a$  is related to the width. In the limit  $q \rightarrow 1$ , a Gaussian distribution is recovered, whereas for  $q = 2$  the line shape is Lorentzian. The relation to the actual spin line-width (FWHM) is given by  $\gamma_q = 2\sqrt{\frac{a(2^q-2)}{2q-2}}$ .

To retrieve the full surface plot the data has been interpolated with an algorithm for smoothing of gridded data with missing values [128]. By comparing the position of the fitted resonances to the predicted by a numerical diagonalization of the Hamiltonian (black solid lines), a good agreement is found. The unperturbed energies are plotted in solid/dashed red lines.

In Figure 9.9 panel b the cavity shift as function of the pump beam energy is plotted for a field angle of  $23^\circ$ . Both spin transitions are distinguishable and can be mapped to the individual ensembles. As the degeneracy point is reached at  $48.1^\circ$ , only the single prominent feature plotted in Figure 9.9 panel d is observed. This bright feature corresponds to the antisymmetric superposition  $|A\rangle$ . Since the ensembles are located on the resonator at the position of the magnetic field antinodes which have opposite sign, the antisymmetric drive forbids a transition to the symmetric state. The appearance of this dark resonance in the vicinity of the degeneracy further underlines the coupling of the two ensembles via virtual photons in the cavity.

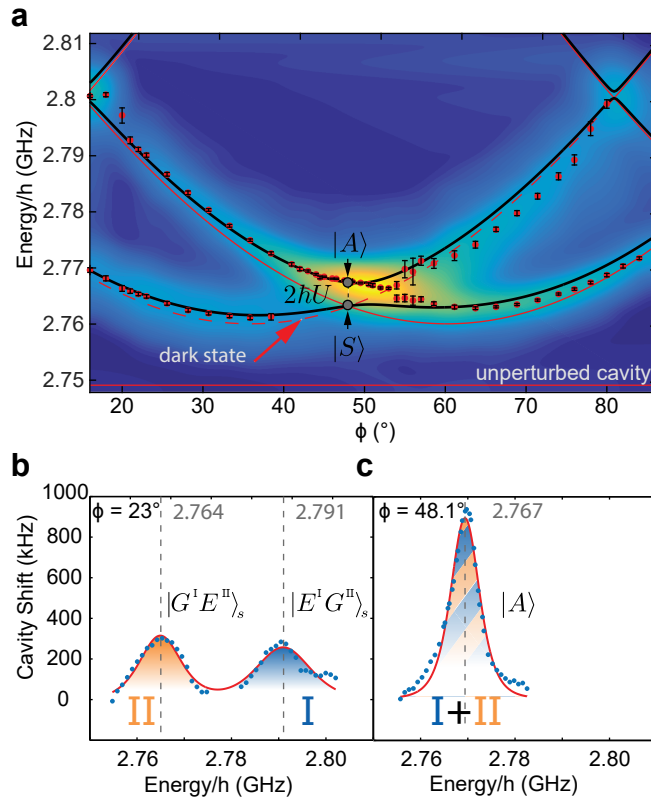


**Figure 9.9.: Dispersive level spectroscopy.** The surface plots presents the results of the dispersive spectroscopy as function of the angle of the external magnetic field. The black solid lines are the eigenenergies calculated by diagonalizing the full system Hamiltonian. Uncoupled eigenenergies for ensemble I and II are shown in solid and dashed red lines, respectively. The data points mark the peak positions of the fitted resonances. In the vicinity only a single bright feature is observed whereas the dark state manifests itself in the disappearance of the spectroscopy signal. **b-c**, Measured dispersive spectrum for  $23^\circ$  where both spin features can be mapped to ensemble I and II. Under an angle of  $48.1^\circ$  only one prominent feature is observed which corresponds to the antisymmetric superposition of excitations in both ensembles. Figure taken from [41].

## 9.4. Conclusion and Outlook

This chapter dealt with the experimental implementation of coherent coupling between two spatially separated spin ensembles via a superconducting transmission line resonator. In angle resolved transmission spectroscopy it was possible to show the strong coupling of each individual ensemble to the mode and the simultaneous coupling of both ensembles to the mode. Therefore, by almost doubling the amount of spins the coupling to the mode was enhanced, which resulted in a more pronounced avoided

crossing. Additionally, the transition to the dark resonance was directly observed in the spectroscopy.

In a set of dispersive measurements, the transverse coupling of the two ensembles was shown via the observation of bright and dark resonances. All these observations were confirmed by a theoretical model and analysis and present a first step towards the goal of quantum information transfer between large ensembles of NV centres.

Despite that the data shows coherent coupling, a fundamental necessity to observe entanglement in the system, the observation of an avoided level crossing does not infer anything on the degree of entanglement. This however, presents an ongoing experimental and theoretical challenge to proof entanglement in a system consisting of two coupled spin ensembles [129, 130].

The experiment at hand presents the coupling two or more distinct systems to the same environment where potentially unusual behaviour and dynamics can be observed. For example the relaxation of two spin ensembles coupled to the same bosonic reservoir can show a steady state which is different of the ground state of the individual systems. If the ensembles differ in size, collective relaxation of the composite systems can drive the smaller ensemble to an excited steady state even if it starts in its ground state - a relaxation towards a negative-temperature steady state [131] and an reservoir-assisted quantum entanglement between the two domains [132].

# Outlook and Prospects

In this thesis two experiments that concern a hybrid quantum system consisting of ensembles of NV centres and microwave resonator have been presented. The first experiment answered the question of the longitudinal spin lattice relaxation of the NV centre. There the main findings were that the low phononic density of states at the NV transition allows a non-equilibrium state of inversion to survive of macroscopic time-scales of up to 8 h. To obtain these results a new resonator geometry was used to coupled to all spins in a large ensemble and determine their collective inversion state as function of time. An advantage of working in the strong dispersive limit of cavity QED is the possibility to determine a full inversion versus time curve by initializing the ensemble only once. Additionally, by making use of this dispersive detection scheme the state of the ensemble can be monitored continuously.

In the second experiment, the coupling of two spatially separated spin ensembles to a common bosonic resonator mode was studied. The main findings where coherent strong coupling of both ensembles to the resonator. In this regime the two spatially separated spin ensembles behave like a single giant ensemble with almost twice as many spins. Additionally, in the dispersive regime a transverse ensemble-ensemble coupling via virtual photons in the resonator was shown. This presents a first step towards the coherent information transfer and the entanglement between to remote spin ensembles.

Both experiments use the strong dispersive limit of cavity QED to either infer the inversion state of a single ensemble or two couple two distant ensembles. Having a  $T_1$  time that is so exceedingly long ( $\approx 8$  h), the following observation can be made: for measuring a dispersive spectroscopy like done in Figure 9.9, after each data point one would have to wait several  $T_1$  times until the system is in its ground state again after driving it. In the experiments, however, it turned out that the time scale of the frequency shift decay after dispersively pumping the spins does not match the timescale of  $T_1$ . Typical signals that are obtained by a dispersive pump-probe spectroscopy are plotted in Figure 1. This time scales are in the order of seconds up to minutes and must be clearly distinguished from any  $T_1$  process.

An analysis of the data in Figure 1 is presented in Figure 2. It further confirms that the decay of this resonance shift does not follow an exponential decay law but rather a

simple power law in the form

$$\chi \propto at^k, \quad (1)$$

with typical values for  $k$  between  $-0.8$  and  $-2$ , depending on the temperature the decay has been measured.

This time scale is short in comparison to  $T_1$  and suggests that other physical phenomena are happening in this system. In the set-up where a single ensemble is placed on a coplanar waveguide resonator, only a fraction of the spins is interacting with the mode. The ratio of spins coupled to the mode to the overall amount of spins can be estimated to be in the order of  $1 \times 10^{-6}$ . One idea is that excitations in the coupled spins diffuse and distribute throughout the whole ensemble because of spin-spin interaction. Depending on the density, the dipole-dipole interaction strength can reach values up to several hundred kilohertz.

In this case the inhomogeneous single spin Rabi frequencies of the coplanar waveguide presents a wanted feature by only coupling to spins in the vicinity of the resonator surface.

The most naive description would be diffusion with the 'point source' initial conditions. At the beginning of the pumping,  $t = 0$ , the energy density is given by a small volume. For  $t > 0$  this energy density diffuses and spreads throughout the large spin ensemble. For an isotropic medium in 3-dimensions the diffusion kernel reads:

$$E(x, y, z) = \frac{E_0}{(4\pi t D)^{3/2}} \exp\left(-\frac{r^2}{4Dt}\right). \quad (2)$$

At  $r = 0$  the decay of the signal is expected to follow  $1/t^{3/2}$ , if the transport is indeed due to conventional diffusion.

In the experiments performed this was clearly not the case since the energy density is released from the boundary of a 3D system (close to the surface). The more relevant geometry is a semi-infinite volume where the energy density is released from its boundary. With the use of the mirror image method, one can guess the solution as

$$E(x, y, z) = \frac{E_0}{(4\pi t D)^{3/2}} \left[ \exp\left(-\frac{x^2 + y^2 + (z + z_0)^2}{4Dt}\right) + \exp\left(-\frac{x^2 + y^2 + (z - z_0)^2}{4Dt}\right) \right], \quad (3)$$

where the boundary with no-flux condition is located at the  $z = 0$  plane and  $z_0 > 0$  is the source position. Here  $D$  presents the diffusion constant. Calculating the log-derivative one again obtains that the power law has an exponent of  $-3/2$  with additional corrections that are suppressed as  $O(1/t)$  with time. Hence, at any finite time the

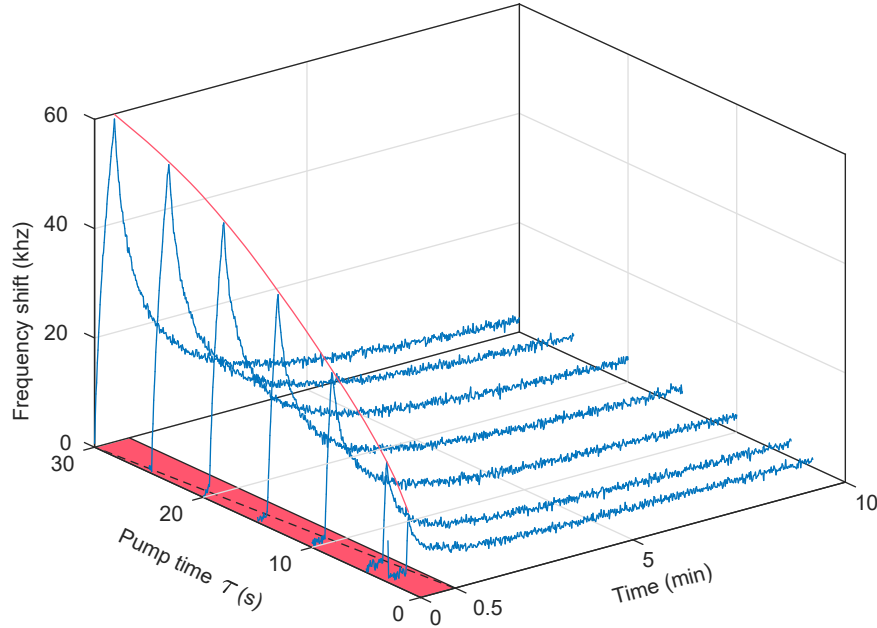


**Figure 1.: Frequency shift decay after dispersive pumping.** In the beginning a strong microwave signal is injected in the cavity, on resonance with spin transition. A fraction of the ensembles is brought in a statistical mixture (the drive is much longer than any coherence in the system) and changes the collective  $\langle \hat{S}_z^2 \rangle$  value depending on the length  $\tau$  of the pulse. Hence, the cavity resonance shifts. After pumping the decay of the resonance shift happens on time-scales of minutes.

exponent of the decay will be smaller than  $3/2$  - the behaviour coming entirely from the finite geometry. This result does not resemble the measured data. Finding an explanation and a proper description for the diffusion in such ensembles is an ongoing research effort.

Finally, this behaviour opens further questions:

1. Is this a signature for diffusion of excitations through the ensemble?
2. What is the energy scale if diffusion comes from dipolar interactions?
3. How exactly does this microscopic flip-flop process look like?

The system at hand has the interesting property that the direct NV-NV dipole interaction can happen on much faster time-scales than the longitudinal relaxation. Excitations in the system are not lost but rather transported and distributed throughout the whole ensemble. This might enable new studies on many body dynamics in large ensembles of NV centres. This experiment is in its very early beginning but presents an interesting problem the should definitely be pursued in the future.

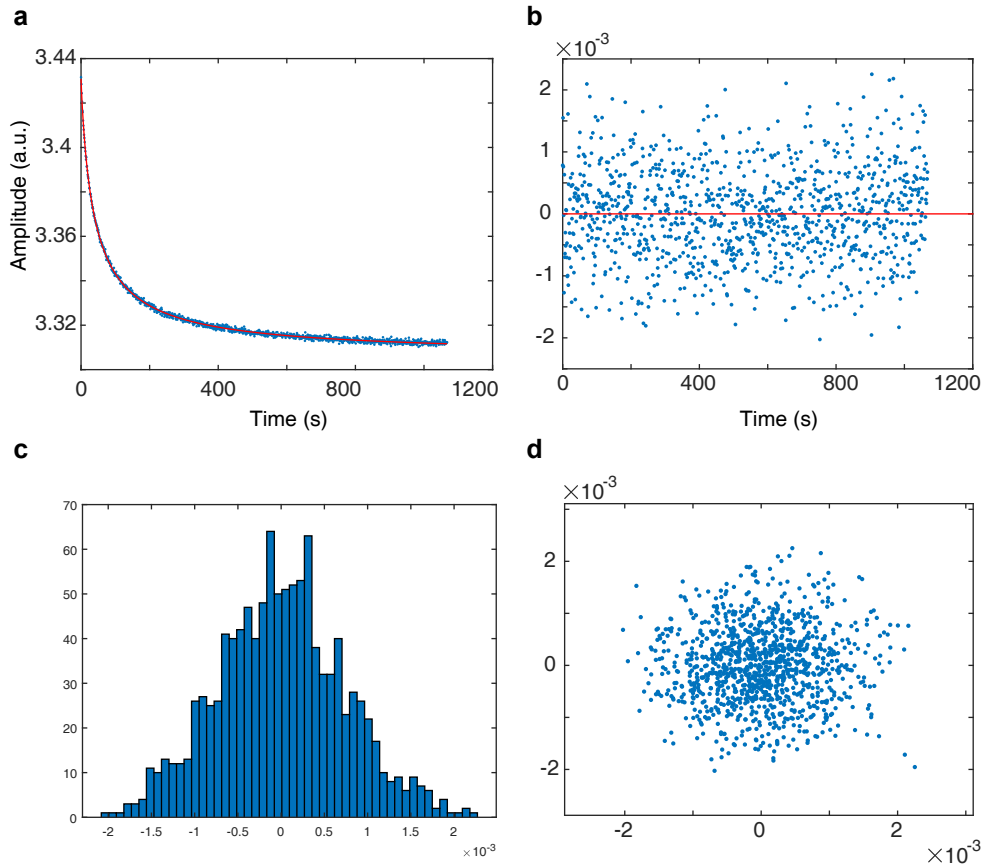


**Figure 2.:** Analysis of the decaying frequency shift. **a-b** Power law fit to the data obtained from a pump-prob experiment. In the second panel the fit residuals are presented. **c-d** Histogram of the residuals. The lag plot in the right panel shows that the data is uncorrelated.



# Appendix

## A. Single Phonon Relaxation Dynamics for Small Magnetic Fields

Introducing a magnetic field, an estimation for the individual relaxation rates in Equation (1.20) is given by

$$A_1 \approx 2\Gamma_0 \left( \frac{2\gamma_s B_0}{D} \right)^3, \quad (1a)$$

$$A_2 \approx \Gamma_0 \left[ \frac{(D + \gamma_s B_0)}{D} \right]^3, \quad (1b)$$

$$A_3 \approx \Gamma_0 \left[ \frac{(D - \gamma_s B_0)}{D} \right]^3. \quad (1c)$$

Considering  $\mu_{\text{NV}}B_0 \ll D$  as the low field limit, the following approximation can be made,  $n(D + \mu_{\text{NV}}B_0) \approx n(D - \mu_{\text{NV}}B_0) \approx \bar{n}$ . The difference to the zero field case is that the degeneracy between the  $|m_s = \pm 1\rangle$  is lifted and, hence,  $\langle \hat{S}_z \rangle$  becomes non-zero. The previous equations then become

$$\frac{d\langle \hat{S}_z^2(t) \rangle}{dt} = -\Gamma_0(1 + 3\bar{n}) \langle \hat{S}_z^2(t) \rangle + 3\epsilon\Gamma_0(1 + \bar{n}) \langle \hat{S}_z(t) \rangle + 2\Gamma_0\bar{n}, \quad (2a)$$

$$\begin{aligned} \frac{d\langle \hat{S}_z(t) \rangle}{dt} = & -[\Gamma_B n_B + 3\epsilon\Gamma_0(1 + 3\bar{n})] \langle \hat{S}_z^2(t) \rangle + 6\epsilon\Gamma_0\bar{n} \\ & - [\Gamma_B(1 + 2n_B) + \Gamma_0(1 + \bar{n})] \langle \hat{S}_z(t) \rangle. \end{aligned} \quad (2b)$$

The dimensionless parameter  $\epsilon = \mu_{\text{NV}}B_0/D$  was introduced to describe the small perturbation. The other used quantities are  $\Gamma_B \approx \Gamma_0(2\mu_{\text{NV}}B_0/D)^3$  and  $n_B = [\exp(2\mu_{\text{NV}}B_0/k_B T) - 1]^{-1}$  as the mean number of phonons resonant with  $\omega_1 = 2\mu_{\text{NV}}B_0$ . The spin lattice relaxation rate for small fields then is given by

$$\frac{1}{T_1} \approx 2\Gamma_0(1 + 2\bar{n}) + \Gamma_B(1 + 2n_B). \quad (3)$$

where the number of phonons  $n_B$  satisfies  $n_B \gg \bar{n}$  in the small field limit. The steady state has the form

$$\frac{\langle \hat{S}_z^2(T) \rangle_{\text{st}}}{\langle \hat{S}_z(T) \rangle_{\text{st}}} = \frac{\Gamma_0(1 + \bar{n}) + \Gamma_B(1 + 2n_B)}{n_B \Gamma_B}. \quad (4)$$

## B. Entropy of a Spin Ensemble

With the Helmholtz free energy ( $F$ ) the entropy ( $S$ ) can be expressed in the following way

$$S = Nk_B \ln Z + E/T \implies F = E - TS = -Nk_B \ln Z, \quad (5a)$$

$$F = N\varepsilon_0 + Nk_B T \ln(1 + 2e^{-\varepsilon/k_B T}), \quad (5b)$$

$$\implies S = -\frac{\partial F}{\partial T} = Nk_B \left[ \ln(1 + 2e^{-\varepsilon/k_B T}) + \frac{2e^{-\varepsilon/k_B T}}{1 + 2e^{-\varepsilon/k_B T}} \frac{\varepsilon}{k_B T} \right]. \quad (5c)$$

## C. Spin operators

An explicit representation with the basis vectors has the following form

$$\hat{F}_x(\mathbf{S}) = \begin{pmatrix} 0 & 0 & 1 \\ 0 & 0 & 0 \\ 1 & 0 & 0 \end{pmatrix}, \quad \hat{F}_{x'}(\mathbf{S}) = \frac{1}{\sqrt{2}} \begin{pmatrix} 0 & 1 & 0 \\ 1 & 0 & -1 \\ 0 & -1 & 0 \end{pmatrix} \quad (6a)$$

$$\hat{F}_y(\mathbf{S}) = \begin{pmatrix} 0 & 0 & -i \\ 0 & 0 & 0 \\ i & 0 & 0 \end{pmatrix}, \quad \hat{F}_{y'}(\mathbf{S}) = \frac{1}{\sqrt{2}} \begin{pmatrix} 0 & -i & 0 \\ i & 0 & i \\ 0 & -i & 0 \end{pmatrix} \quad (6b)$$

$$\hat{F}_z(\mathbf{S}) = \begin{pmatrix} 1 & 0 & 0 \\ 0 & 0 & 0 \\ 0 & 0 & 1 \end{pmatrix}. \quad (6c)$$

## D. Maxwell-Bloch Equations

The NV centre is well approximated as a 3-level system with degenerate excited states. Therefore, a modified Tavis-Cummings Hamiltonian including a drive term can be

the form

$$\frac{\hat{H}}{\hbar} = \omega_c \hat{a}^\dagger \hat{a} + \frac{\omega_s}{2} \hat{S}_z^2 + ig_N (\hat{a}^\dagger \hat{S}^- - \hat{a} \hat{S}^+) + \hat{H}_d. \quad (7)$$

Under the rotating wave approximation a drive term has the form

$$\frac{\hat{H}_d}{\hbar} = i\eta (\hat{a}^\dagger e^{-i\omega_p t} - \hat{a} e^{i\omega_p t}). \quad (8)$$

In order to remove the time dependence, the Hamiltonian can be transformed under the unitary transformation

$$\hat{H}_{\text{sys}} = \hat{U}^\dagger \hat{H} \hat{U} - i\hbar \hat{U} \frac{\partial \hat{U}}{\partial t}. \quad (9)$$

with the operator

$$\hat{U} = e^{-i\omega_p t (\hat{a}^\dagger \hat{a} + \hat{S}_z^2)}. \quad (10)$$

Then the system Hamiltonian can be written in the form

$$\frac{\hat{H}}{\hbar} = \Delta_c \hat{a}^\dagger \hat{a} + \Delta_s \hat{S}_z^2 + g_N (\hat{a}^\dagger \hat{S}^- + \hat{a} \hat{S}^+) + i\eta (\hat{a}^\dagger - \hat{a}) \quad (11)$$

With this the equation of motion for the density matrix is given by

$$\frac{d\hat{\rho}(t)}{dt} = -\frac{i}{\hbar} [\hat{H}(t), \hat{\rho}(t)] + \mathcal{L}[\rho]. \quad (12)$$

The time evolution of the expectation values ( $\langle \dot{\hat{O}} \rangle = \text{Tr}(\dot{\hat{\rho}} \hat{O})$ ) leads to the following system of coupled equations:

$$\langle \dot{\hat{a}} \rangle = -1\Delta_c \langle \hat{a} \rangle - ig \langle \hat{S}^- \rangle + \eta - \kappa \langle a \rangle, \quad (13)$$

$$\langle \dot{\hat{S}}^- \rangle = -i\Delta_s \langle \hat{S}^- \rangle - 2ig \left[ 2I_3 - 3 \langle \hat{S}_z^2 \rangle - \langle \hat{S} \rangle \right] \langle \hat{a} \rangle - (\Gamma_1/2 + \gamma_\perp/4) \langle \hat{S}^- \rangle, \quad (14)$$

$$\langle \dot{\hat{S}}_z^2 \rangle = ig (\langle \hat{S}^- \rangle \langle \hat{a}^\dagger \rangle - \langle \hat{S}^+ \rangle \langle \hat{a} \rangle) - \Gamma_1 \langle \hat{S}_z^2 \rangle, \quad (15)$$

$$\langle \dot{\hat{S}} \rangle = ig (\langle \hat{S}^- \rangle \langle \hat{a}^\dagger \rangle - \langle \hat{S}^+ \rangle \langle \hat{a} \rangle) - (\Gamma_1 + \gamma_\perp/2) \langle \hat{S} \rangle. \quad (16)$$

Here,  $\hat{S}$  can be built from the primitive operators of the  $U(3)$  symmetry group,  $\hat{S} = \hat{S}_3 + \hat{S}_7$ . The steady state is obtained when the time derivative on the left hand side vanishes for each equation. Furthermore, in a thermal state the expectation value of  $\langle \hat{S} \rangle = 0$  as this operator moves population between the  $|-1\rangle$  and  $|+1\rangle$  states. The

system reduces to two coupled equations and the expectation value  $\langle \hat{a}^\dagger \hat{a} \rangle$  can easily be computed.

## E. Lorentzian Line Fit

In Figure 1 a standard fit to the Lorentzian line shape is presented. To obtain the resonance frequency and width of the cavity, the following complex fit function is used

$$T(\omega) = Ae^{-i\varphi} e^{i\omega dt} \frac{-i\frac{\kappa}{2}}{\omega - \omega_c - i\frac{\kappa}{2}}. \quad (17)$$

In this equation,  $\kappa$  denotes the full width at half maximum (FWHM) of the resonance. Furthermore,  $A$  is the amplitude,  $\varphi$  a global phase factor,  $\omega$  the VNA probe frequency and  $dt$  a frequency dependent phase.

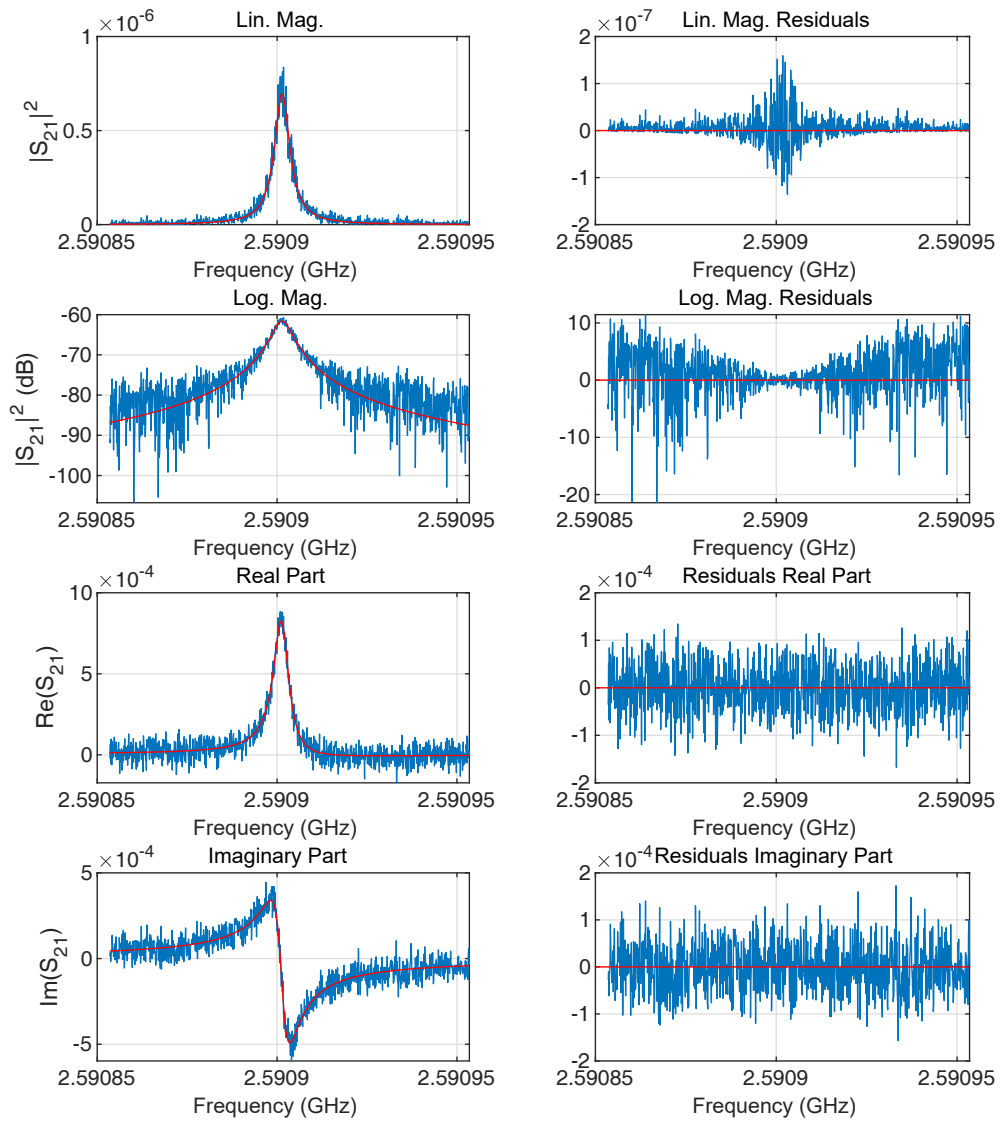


**Figure 1.: Lorentzian line shape fit.** The panels show a typical fit to a lorentzian line shape profile obtained from a transmission meausurement with the vector network analyser.

## F. Loop-Gap Resonator

Another resonator design that exhibits homogeneous single spin coupling is the so called Loop-Gap resonator which is also uses 3D lumped elements. Coupling rates of up to 200 mHz were reported for this type of 3D lumped element resonator [133] - larger than the introduced bow-tie design.

To exploit this feature the design presented in the original publication has been adapted to generate resonance around 3 GHz. The eigenmodes of the geometry and transmission spectra can be simulated with the software COMSOL Multiphysics ©.

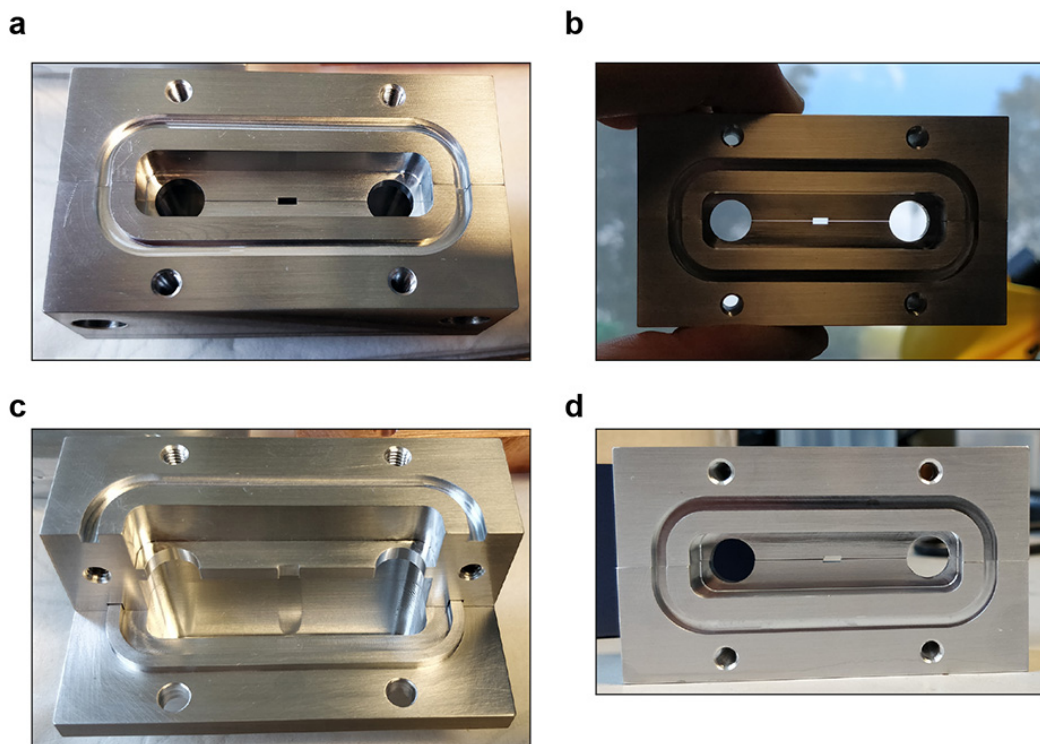


**Figure 2.:** Photograph of the manufacture loop-gap resonator. a-d, Loop-gap resonator with enclose manufactured out of standard machine grade aluminum. The slit between the capacitor plates has a width of 80  $\mu\text{m}$ .

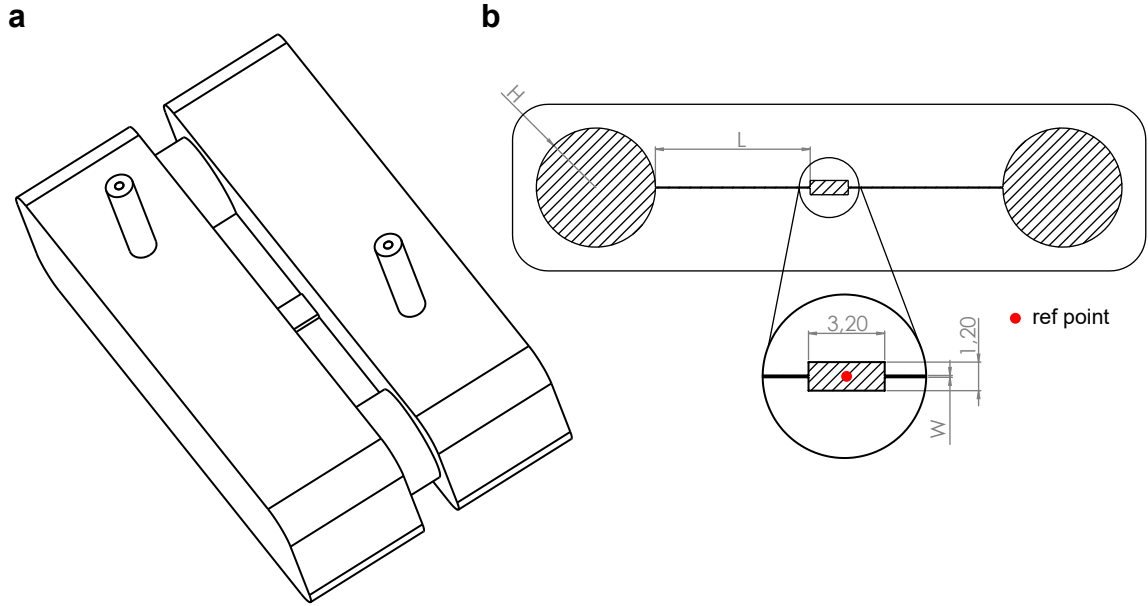


**Figure 3.:** Loop-Gap Simulation Model **a**, CAD model of the loop gap resonator design with two coaxial probes for coupling the resonator to external circuitry. **b**, Cross-section through the resonator showing the resonance defining parameters like the hole radius and the capacitor length (the width of the resonator is kept constant). The magnetic field is evaluated in the centre of the sample volume.

In Figure 2 the photograph shows the manufactured loop gap resonator with a centre sample volume of  $3.2\text{ mm} \times 1.2\text{ mm} \times 4\text{ mm}$ . Two gap slits on each side act as plate capacitors and the inductance is given by the current path around the sample volume. As in the bow-tie resonator, this resonator supports two modes. The first loop-gap mode focuses the magnetic field into the sample region. The second loop gap mode generates no magnetic field there and is lower in frequency. Additionally, as the coupling into the mode is done via coaxial pins in a surrounding box, the box itself exhibits a resonance. When designing it is important that this resonance is detuned from the main loop gap mode. To analyse the system the simplified circuit is presented in Figure 4, together with its Norton equivalent.

### Single Spin Coupling Rate

In comparison to the bow-tie design, the loop-gap resonator geometry has higher symmetry in the sample region and reduces the mode volume significantly. 90% of the magnetic field is within a volume of  $\sim 20\text{ mm}^3$ , which computes to a vacuum magnetic field amplitude of  $B_0 \approx 8\text{ pT}$  and a single electron spin Rabi frequency of  $g_0/2\pi \approx 120\text{ mHz}$ .

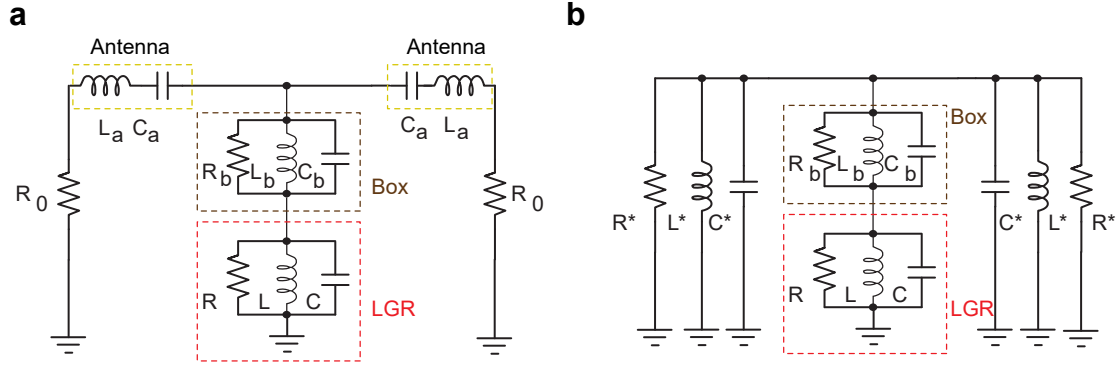


**Figure 4.: Loop-gap resonator circuit model.** **a**, The system consists of a box and the loop-gap resonator, both modelled as parallel RLC circuit. Coupling to the external circuitry is done via two antenna pins (modelled as LC) and a load impedance  $R_0$ . **b**, Norton equivalent circuit of **a**. Circuit models taken from [133] (supplementary material).

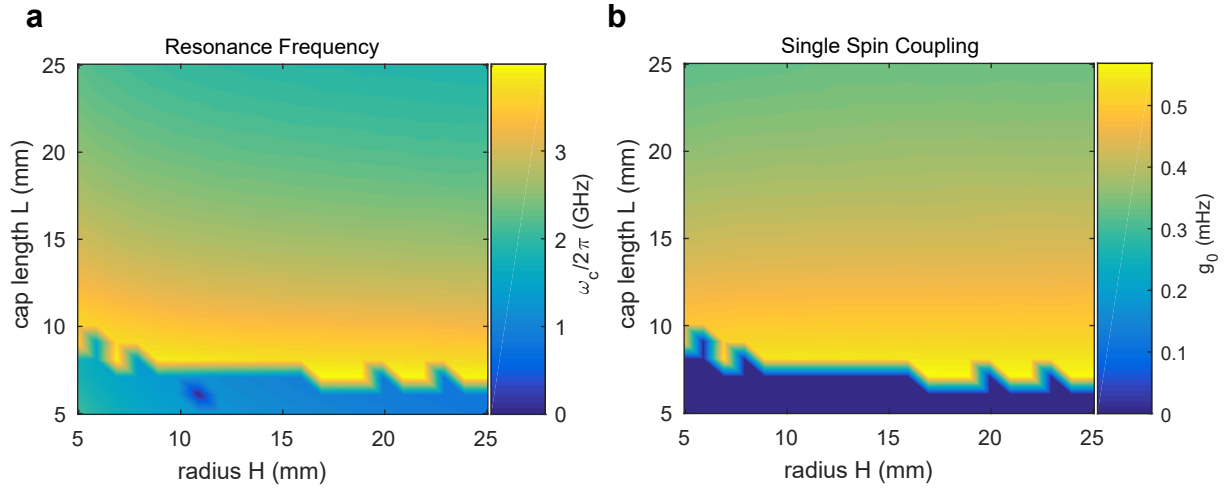


**Figure 5.: Eigenfrequency and single spin coupling rate of the loop-gap resonator.** **a**, Eigenfrequency of the resonator as function of the hole radius and the length of a capacitor plate. In the parameter regime where the capacitor length is below 10 mm has a mode jump and is unstable. **b**, Single spin coupling rate in the sample region. This parameter is proportional to  $\sqrt{\hbar\omega_c}$  and the mode volume. By changing the hole and capacitor geometry the mode confinement changes. A less confined mode results in a low single spin coupling rate.



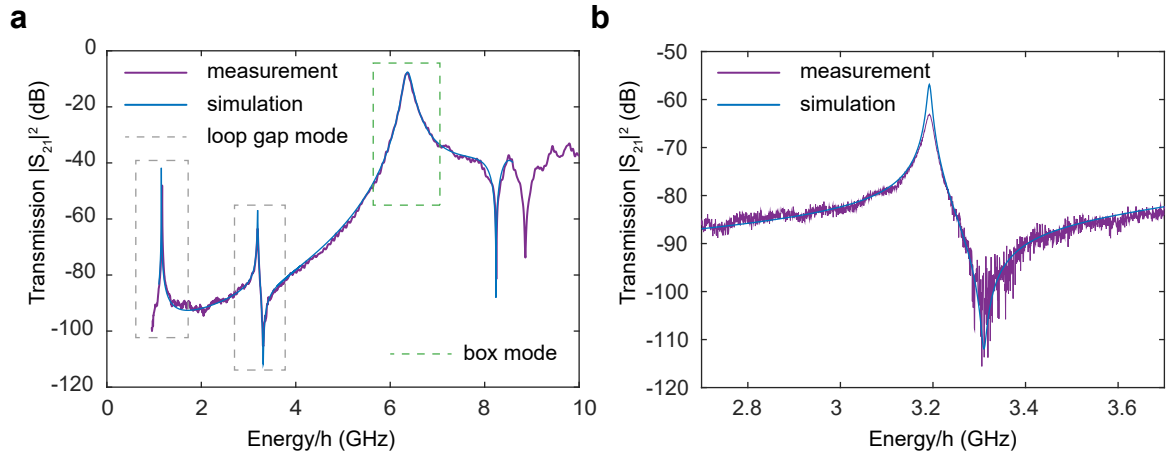


**Figure 6.: Loop-gap resonator transmission spectroscopy.** **a**, Broadband microwave transmission spectroscopy of the full loop-gap assembly (resonator and enclosure). The first two resonances are loop-gap modes whereas the resonance at around 6 GHz corresponds to a box mode of the enclosure structure. A finite element model shows good agreement of measurement and the simulation. **b**, Magnified resonance of the loop gap mode at 3.2 GHz.

### Transmission Spectrum

In Figure 6 the simulated and measured broadband transmission spectrum of the designed loop-gap resonator is presented. The simulation is able to capture all important features of the measurement and shows excellent qualitative and quantitative agreement.

# List of Figures

1.1. NV level structure . . . . .	4
1.2. Temperature-dependent level occupation. . . . .	6
1.3. Schottky anomaly of the heat capacity . . . . .	7
1.4. Relaxation rates between the spin states . . . . .	10
1.5. Relaxation processes mediated by a single phonon . . . . .	15
2.1. Jaynes-Cummings system . . . . .	19
2.2. Energy level diagram . . . . .	20
2.3. Energy level diagram of a generalized 3 level JC system . . . . .	22
3.1. Schematic representation of the cavity fields . . . . .	29
3.2. LC resonant circuit . . . . .	31
3.3. Parallel RLC resonant circuit . . . . .	32
4.1. Coplanar waveguide resonator . . . . .	36
4.2. Circuit diagrams of a coplanar waveguide resonator . . . . .	37
4.3. Spatial dependence of the magnetic field generated by a CPW resonator . . . . .	39
4.4. 3D-LER resonator . . . . .	42
4.5. Magnetic field simulation . . . . .	43
4.6. Broadband transmission spectrum . . . . .	44
4.7. Superconducting bow-tie resonator phase transition . . . . .	45
4.8. Superconducting bow-tie resonator parameters . . . . .	46
6.1. Diamond backed CPW resonator . . . . .	50
6.2. Diamond loaded bow-tie resonator . . . . .	51
6.3. Temperature stability analysis . . . . .	52
6.4. Cool-down sequence . . . . .	53
6.5. ADR cryostat set-up . . . . .	55
7.1. Strong coupling between a spin ensemble and the bow-tie mode . . . . .	58
8.1. Experimental set-up . . . . .	62
8.2. Superconducting bow-tie resonator . . . . .	66
8.3. Time evolution of the spin inversion . . . . .	68

## List of Figures

---

8.4.	Temperature dependence of the relaxation rate . . . . .	71
8.5.	Spin-spin interaction of the electrons in a single NV centre . . . . .	74
8.6.	Phonon density of states . . . . .	75
9.1.	Photograph of two diamonds on the resonator . . . . .	78
9.2.	Diamond sub-ensembles . . . . .	79
9.3.	Tuning of transition energies . . . . .	80
9.4.	Resonant coupling scheme . . . . .	82
9.5.	Transmission spectroscopy . . . . .	84
9.6.	Angle resolved transmission spectroscopy . . . . .	86
9.7.	Dispersive coupling scheme . . . . .	89
9.8.	Dispersive spectroscopy technique . . . . .	91
9.9.	Dispersive level spectroscopy . . . . .	93
1.	Pump probe in the time domain . . . . .	97
2.	Decay signal analysis . . . . .	98
1.	Cavity resonance fit . . . . .	103
2.	Photograph of the manufacture loop-gap resonator . . . . .	104
3.	Loop-Gap Simulation Model . . . . .	105
4.	Loop-gap resonator circuit model . . . . .	106
5.	Eigenfrequency and single spin coupling rate of the loop-gap resonator	106
6.	Loop-gap resonator transmission spectroscopy . . . . .	107

# List of Tables

8.1. Sample characteristics . . . . .	73
---------------------------------------	----

## References

- [1] F. Jelezko and J. Wrachtrup. “Single defect centres in diamond: A review”. In: *Physica Status Solidi (a)* 203.13 (Oct. 2006), pp. 3207–3225. DOI: [10.1002/pssa.200671403](https://doi.org/10.1002/pssa.200671403).
- [2] Romana Schirhagl, Kevin Chang, Michael Loretz, and Christian L. Degen. “Nitrogen-Vacancy Centers in Diamond: Nanoscale Sensors for Physics and Biology”. In: *Annual Review of Physical Chemistry* 65.1 (Apr. 2014), pp. 83–105. DOI: [10.1146/annurev-physchem-040513-103659](https://doi.org/10.1146/annurev-physchem-040513-103659).
- [3] L. T. Hall, G. C.G. Beart, E. A. Thomas, et al. “High spatial and temporal resolution wide-field imaging of neuron activity using quantum NV-diamond”. In: *Scientific Reports* 2.1 (Dec. 2012), p. 401. DOI: [10.1038/srep00401](https://doi.org/10.1038/srep00401).
- [4] M. W. Doherty, F. Dolde, H. Fedder, et al. “Theory of the ground state spin of the NV- center in diamond: II. Spin solutions, time-evolution, relaxation and inhomogeneous dephasing”. In: *Physical Review B* 85.20 (May 2011), p. 205203. DOI: [10.1103/PhysRevB.85.205203](https://doi.org/10.1103/PhysRevB.85.205203).
- [5] Marcus W. Doherty, Neil B. Manson, Paul Delaney, et al. *The nitrogen-vacancy colour centre in diamond*. July 2013. DOI: [10.1016/j.physrep.2013.02.001](https://doi.org/10.1016/j.physrep.2013.02.001).
- [6] Jörg Wrachtrup and Fedor Jelezko. “Processing quantum information in diamond”. In: *Journal of Physics Condensed Matter* 18.21 (May 2006), S807–S824. DOI: [10.1088/0953-8984/18/21/S08](https://doi.org/10.1088/0953-8984/18/21/S08).
- [7] C. Simon, M. Afzelius, J. Appel, et al. “Quantum memories”. In: *The European Physical Journal D* 58.1 (May 2010), pp. 1–22. DOI: [10.1140/epjd/e2010-00103-y](https://doi.org/10.1140/epjd/e2010-00103-y).
- [8] Jianming Cai, Alex Retzker, Fedor Jelezko, and Martin B. Plenio. “A large-scale quantum simulator on a diamond surface at room temperature”. In: *Nature Physics* 9.3 (Mar. 2013), pp. 168–173. DOI: [10.1038/nphys2519](https://doi.org/10.1038/nphys2519).
- [9] P. Neumann, I. Jakobi, F. Dolde, et al. “High-precision nanoscale temperature sensing using single defects in diamond”. In: *Nano Letters* 13.6 (June 2013), pp. 2738–2742. DOI: [10.1021/nl401216y](https://doi.org/10.1021/nl401216y).
- [10] Boris Naydenov and Fedor Jelezko. “Single-Color Centers in Diamond as Single-Photon Sources and Quantum Sensors”. In: *Springer Series on Fluorescence*. Springer, Cham, 2014, pp. 303–318. DOI: [10.1007/4243\\_2014\\_78](https://doi.org/10.1007/4243_2014_78).
- [11] Michael S.J. Barson, Phani Peddibhotla, Preeti Ovarthaiyapong, et al. “Nanomechanical Sensing Using Spins in Diamond”. In: *Nano Letters* 17.3 (2017), pp. 1496–1503. DOI: [10.1021/acs.nanolett.6b04544](https://doi.org/10.1021/acs.nanolett.6b04544).

- 
- [12] J. M. Taylor, P. Cappellaro, L. Childress, et al. “High-sensitivity diamond magnetometer with nanoscale resolution”. In: *Nature Physics* 4.10 (Oct. 2008), pp. 810–816. DOI: [10.1038/nphys1075](https://doi.org/10.1038/nphys1075).
- [13] Gopalakrishnan Balasubramanian, I. Y. Chan, Roman Kolesov, et al. “Nanoscale imaging magnetometry with diamond spins under ambient conditions”. In: *Nature* 455.7213 (Oct. 2008), pp. 648–651. DOI: [10.1038/nature07278](https://doi.org/10.1038/nature07278).
- [14] V. M. Acosta, E. Bauch, M. P. Ledbetter, et al. “Diamonds with a high density of nitrogen-vacancy centers for magnetometry applications”. In: *Physical Review B - Condensed Matter and Materials Physics* 80.11 (Sept. 2009), p. 115202. DOI: [10.1103/PhysRevB.80.115202](https://doi.org/10.1103/PhysRevB.80.115202).
- [15] G. Waldherr, J. Beck, P. Neumann, et al. “High-dynamic-range magnetometry with a single nuclear spin in diamond”. In: *Nature Nanotechnology* 7.2 (Feb. 2012), pp. 105–108. DOI: [10.1038/nnano.2011.224](https://doi.org/10.1038/nnano.2011.224).
- [16] David J. Wineland. *Superposition, entanglement, and raising Schrödinger’s cat (Nobel lecture)*. July 2013. DOI: [10.1002/anie.201303404](https://doi.org/10.1002/anie.201303404).
- [17] Serge Haroche. *Controlling photons in a box and exploring the quantum to classical boundary*. July 2013. DOI: [10.1002/andp.201300737](https://doi.org/10.1002/andp.201300737).
- [18] Atac Imamoğlu. “Cavity QED based on collective magnetic dipole coupling: Spin ensembles as hybrid two-level systems”. In: *Physical Review Letters* 102.8 (Feb. 2009), p. 083602. DOI: [10.1103/PhysRevLett.102.083602](https://doi.org/10.1103/PhysRevLett.102.083602).
- [19] Xiaobo Zhu, Shiro Saito, Alexander Kemp, et al. “Coherent coupling of a superconducting flux qubit to an electron spin ensemble in diamond”. In: *Nature* 478.7368 (Oct. 2011), pp. 221–224. DOI: [10.1038/nature10462](https://doi.org/10.1038/nature10462).
- [20] Y. Kubo, F. R. Ong, P. Bertet, et al. “Strong coupling of a spin ensemble to a superconducting resonator”. In: *Physical Review Letters* 105.14 (Sept. 2010), p. 140502. DOI: [10.1103/PhysRevLett.105.140502](https://doi.org/10.1103/PhysRevLett.105.140502).
- [21] R. Amsüss, Ch. Koller, T. Nöbauer, et al. “Cavity QED with Magnetically Coupled Collective Spin States”. In: *Physical Review Letters* 107.6 (Aug. 2011), p. 060502. DOI: [10.1103/PhysRevLett.107.060502](https://doi.org/10.1103/PhysRevLett.107.060502).
- [22] Ze-Liang Xiang, Sahel Ashhab, J. Q. You, and Franco Nori. “Hybrid quantum circuits: Superconducting circuits interacting with other quantum systems”. In: *Reviews of Modern Physics* 85.2 (Apr. 2013), pp. 623–653. DOI: [10.1103/RevModPhys.85.623](https://doi.org/10.1103/RevModPhys.85.623).
- [23] Gershon Kurizki, Patrice Bertet, Yuimaru Kubo, et al. “Quantum technologies with hybrid systems”. In: *Proceedings of the National Academy of Sciences* 112.13 (2015), pp. 3866–3873. DOI: [10.1073/pnas.1419326112](https://doi.org/10.1073/pnas.1419326112).
- [24] Alan T. Collins. *Synthetic diamond: Emerging CVD science and technology*. Edited by Karl E. Spear and John P. Dismukes, Wiley, Chichester, UK 1994, XV, 663 pp., hardcover, £74.00, ISBN 0-471- 53589-3. Vol. 1. 1. July 1995, pp. 33–33. DOI: [10.1002/cvde.19950010109](https://doi.org/10.1002/cvde.19950010109).

- 
- [25] David D. Awschalom, Ryan Epstein, and Ronald Hanson. “The Diamond Age Diamond Age of Spintronics”. In: *Scientific American* 297.4 (Oct. 2007), pp. 84–91. DOI: [10.1038/scientificamerican1007-84](https://doi.org/10.1038/scientificamerican1007-84).
- [26] Gordon Davies, Simon C. Lawson, Alan T. Collins, Alison Mainwood, and Sarah J. Sharp. “Vacancy-related centers in diamond”. In: *Physical Review B* 46.20 (Nov. 1992), pp. 13157–13170. DOI: [10.1103/PhysRevB.46.13157](https://doi.org/10.1103/PhysRevB.46.13157).
- [27] Alan T. Collins and G. Davis. “Properties and growth of Diamond”. In: *London, UK: Inspec* (1994), p. 261.
- [28] J. R. Maze, P. L. Stanwix, J. S. Hodges, et al. “Nanoscale magnetic sensing with an individual electronic spin in diamond”. In: *Nature* 455.7213 (Oct. 2008), pp. 644–647. DOI: [10.1038/nature07279](https://doi.org/10.1038/nature07279).
- [29] A. Ajoy, U. Bissbort, M. D. Lukin, R. L. Walsworth, and P. Cappellaro. “Atomic-Scale Nuclear Spin Imaging Using Quantum-Assisted Sensors in Diamond”. In: *Physical Review X* 5.1 (Jan. 2015), p. 011001. DOI: [10.1103/PhysRevX.5.011001](https://doi.org/10.1103/PhysRevX.5.011001).
- [30] Chi-Cheng Fu, Hsu-Yang Lee, Kowa Chen, et al. “Characterization and application of single fluorescent nanodiamonds as cellular biomarkers”. In: *Proceedings of the National Academy of Sciences* 104.3 (Jan. 2007), 727 LP –732.
- [31] G. D. Fuchs, G. Burkard, P. V. Klimov, and D. D. Awschalom. “A quantum memory intrinsic to single nitrogen-vacancy centres in diamond”. In: *Nature Physics* 7.10 (Oct. 2011), pp. 789–793. DOI: [10.1038/nphys2026](https://doi.org/10.1038/nphys2026).
- [32] G. Davies and M. F. Hamer. “Optical Studies of the 1.945 eV Vibronic Band in Diamond”. In: *Proceedings of the Royal Society A: Mathematical, Physical and Engineering Sciences* 348.1653 (Feb. 1976), pp. 285–298. DOI: [10.1098/rspa.1976.0039](https://doi.org/10.1098/rspa.1976.0039).
- [33] A T Collins, M F Thomaz, and M. I.B. Jorge. “Luminescence decay time of the 1.945 eV centre in type Ib diamond”. In: *Journal of Physics C: Solid State Physics* 16.11 (Apr. 1983), pp. 2177–2181. DOI: [10.1088/0022-3719/16/11/020](https://doi.org/10.1088/0022-3719/16/11/020).
- [34] Jan Jeske, Desmond W.M. Lau, Xavier Vidal, et al. “Stimulated emission from nitrogen-vacancy centres in diamond”. In: *Nature Communications* 8 (Jan. 2017), p. 14000. DOI: [10.1038/ncomms14000](https://doi.org/10.1038/ncomms14000).
- [35] F. Jelezko, T. Gaebel, I. Popa, et al. “Observation of coherent oscillation of a single nuclear spin and realization of a two-qubit conditional quantum gate”. In: *Physical Review Letters* 93.13 (Sept. 2004), p. 130501. DOI: [10.1103/PhysRevLett.93.130501](https://doi.org/10.1103/PhysRevLett.93.130501).
- [36] R. J. Epstein, F. M. Mendoza, Y. K. Kato, and D. D. Awschalom. *Anisotropic interactions of a single spin and dark-spin spectroscopy in diamond*. Nov. 2005. DOI: [10.1038/nphys141](https://doi.org/10.1038/nphys141).
- [37] L. Childress, M. V. Gurudev Dutt, J. M. Taylor, et al. “Coherent dynamics of coupled electron and nuclear spin qubits in diamond”. In: *Science* 314.5797 (Oct. 2006), pp. 281–285. DOI: [10.1126/science.1131871](https://doi.org/10.1126/science.1131871).

- 
- [38] J. Berezovsky, M. H. Mikkelsen, N. G. Stoltz, L. A. Coldren, and D. D. Awschalom. “Picosecond coherent optical manipulation of a single electron spin in a quantum dot”. In: *Science* 320.5874 (Nov. 2008), pp. 349–352. DOI: [10.1126/science.1154798](https://doi.org/10.1126/science.1154798).
- [39] J. Harrison, M.J Sellars, and N.B Manson. “Optical spin polarisation of the N-V centre in diamond”. In: *Journal of Luminescence* 107.1-4 (May 2004), pp. 245–248. DOI: [10.1016/j.jlumin.2003.12.020](https://doi.org/10.1016/j.jlumin.2003.12.020).
- [40] S. Felton, A. M. Edmonds, M. E. Newton, et al. “Hyperfine interaction in the ground state of the negatively charged nitrogen vacancy center in diamond”. In: *Physical Review B - Condensed Matter and Materials Physics* 79.7 (Feb. 2009), p. 075203. DOI: [10.1103/PhysRevB.79.075203](https://doi.org/10.1103/PhysRevB.79.075203).
- [41] T Astner, S Nevlacsil, N Peterschofsky, et al. “Coherent Coupling of Remote Spin Ensembles via a Cavity Bus”. In: *Physical Review Letters* 118.14 (Apr. 2017), p. 140502. DOI: [10.1103/PhysRevLett.118.140502](https://doi.org/10.1103/PhysRevLett.118.140502).
- [42] T. Astner, J. Gugler, A. Angerer, et al. “Solid-state electron spin lifetime limited by phononic vacuum modes”. In: *Nature Materials* 17.4 (Apr. 2018), pp. 313–317. DOI: [10.1038/s41563-017-0008-y](https://doi.org/10.1038/s41563-017-0008-y).
- [43] Florian Scheck. *Theoretische Physik 5*. Springer Berlin Heidelberg, 2008, p. 192.
- [44] I. Waller. “Über die Magnetisierung von paramagnetischen Kristallen in Wechselfeldern”. In: *Zeitschrift für Physik* 79.5-6 (May 1932), pp. 370–388. DOI: [10.1007/BF01349398](https://doi.org/10.1007/BF01349398).
- [45] E. M. Purcell. “Spontaneous Emission Probabilities at Radio Frequencies”. In: *Physical Review* (1946). DOI: [10.1103/PhysRev.69.674.2](https://doi.org/10.1103/PhysRev.69.674.2).
- [46] Albert W. Overhauser. “Paramagnetic relaxation in metals”. In: *Physical Review* 89.4 (Feb. 1953), pp. 689–700. DOI: [10.1103/PhysRev.89.689](https://doi.org/10.1103/PhysRev.89.689).
- [47] M. W. Wu, J. H. Jiang, and M. Q. Weng. *Spin dynamics in semiconductors*. Aug. 2010. DOI: [10.1016/j.physrep.2010.04.002](https://doi.org/10.1016/j.physrep.2010.04.002).
- [48] Audrius Alkauskas, Bob B Buckley, David D Awschalom, and Chris G. Van De Walle. “First-principles theory of the luminescence lineshape for the triplet transition in diamond NV centres”. In: *New Journal of Physics* 16.7 (July 2014), p. 073026. DOI: [10.1088/1367-2630/16/7/073026](https://doi.org/10.1088/1367-2630/16/7/073026).
- [49] Ariel Norambuena, Sebastián A. Reyes, José Mejía-López, Adam Gali, and Jerónimo R. Maze. “Microscopic modeling of the effect of phonons on the optical properties of solid-state emitters”. In: *Physical Review B* 94.13 (Oct. 2016), p. 134305. DOI: [10.1103/PhysRevB.94.134305](https://doi.org/10.1103/PhysRevB.94.134305).
- [50] Elisa Londero, Gergo Thiering, Lukas Razinkovas, Adam Gali, and Audrius Alkauskas. “Vibrational modes of negatively charged silicon-vacancy centers in diamond from ab initio calculations”. In: *Physical Review B* 98.3 (July 2018), p. 035306. DOI: [10.1103/PhysRevB.98.035306](https://doi.org/10.1103/PhysRevB.98.035306).
- [51] A. Norambuena, E. Muñoz, H. T. Dinani, et al. “Spin-lattice relaxation of individual solid-state spins”. In: *Physical Review B* 97.9 (Mar. 2018), p. 094304. DOI: [10.1103/PhysRevB.97.094304](https://doi.org/10.1103/PhysRevB.97.094304).



- 
- [52] Ulrich Weiss. *Quantum Dissipative Systems*. WORLD SCIENTIFIC, Mar. 2012. DOI: [10.1142/8334](https://doi.org/10.1142/8334).
- [53] J E Avron, O Kenneth, A Retzker, and M Shalyt. “Lindbladians for controlled stochastic Hamiltonians”. In: *New Journal of Physics* 17.4 (Apr. 2015), p. 043009. DOI: [10.1088/1367-2630/17/4/043009](https://doi.org/10.1088/1367-2630/17/4/043009).
- [54] B. A. Myers, A. Ariyaratne, and A. C. Bleszynski Jayich. “Double-Quantum Spin-Relaxation Limits to Coherence of Near-Surface Nitrogen-Vacancy Centers”. In: *Physical Review Letters* 118.19 (May 2017), p. 197201. DOI: [10.1103/PhysRevLett.118.197201](https://doi.org/10.1103/PhysRevLett.118.197201).
- [55] I. I. Rabi. “Space quantization in a gyrating magnetic field”. In: *Physical Review* 51.8 (Apr. 1937), pp. 652–654. DOI: [10.1103/PhysRev.51.652](https://doi.org/10.1103/PhysRev.51.652).
- [56] E.T. Jaynes and F.W. Cummings. “Comparison of quantum and semiclassical radiation theories with application to the beam maser”. In: *Proceedings of the IEEE* 51.1 (1963), pp. 89–109. DOI: [10.1109/PROC.1963.1664](https://doi.org/10.1109/PROC.1963.1664).
- [57] Marlan O. (Marlan Orvil) Scully and Muhammad Suhail Zubairy. *Quantum optics*. Cambridge University Press, 1997, p. 630.
- [58] V B Braginsky, Y I Vorontsov, and K S Thorne. “Quantum Nondemolition Measurements”. In: *Science* 209.4456 (Aug. 1980), pp. 547–557. DOI: [10.1126/science.209.4456.547](https://doi.org/10.1126/science.209.4456.547).
- [59] A. Wallraff, D. I. Schuster, A. Blais, et al. “Strong coupling of a single photon to a superconducting qubit using circuit quantum electrodynamics”. In: *Nature* 431.7005 (Sept. 2004), pp. 162–167. DOI: [10.1038/nature02851](https://doi.org/10.1038/nature02851).
- [60] A. Wallraff, D. I. Schuster, A. Blais, et al. “Approaching unit visibility for control of a superconducting qubit with dispersive readout”. In: *Physical Review Letters* 95.6 (Aug. 2005), p. 060501. DOI: [10.1103/PhysRevLett.95.060501](https://doi.org/10.1103/PhysRevLett.95.060501).
- [61] D I Schuster, a a Houck, J a Schreier, et al. “Resolving photon number states in a superconducting circuit.” In: *Nature* 445.7127 (2007), pp. 515–518. DOI: [10.1038/nature05461](https://doi.org/10.1038/nature05461).
- [62] Xiaodong Qi, Ben Q. Baragiola, Poul S. Jessen, and Ivan H. Deutsch. “Dispersive response of atoms trapped near the surface of an optical nanofiber with applications to quantum nondemolition measurement and spin squeezing”. In: *Physical Review A* 93.2 (Feb. 2016), p. 023817. DOI: [10.1103/PhysRevA.93.023817](https://doi.org/10.1103/PhysRevA.93.023817).
- [63] Alexandre Blais, Ren Shou Huang, Andreas Wallraff, S. M. Girvin, and R. J. Schoelkopf. “Cavity quantum electrodynamics for superconducting electrical circuits: An architecture for quantum computation”. In: *Physical Review A - Atomic, Molecular, and Optical Physics* 69.6 (2004), pp. 062320–1. DOI: [10.1103/PhysRevA.69.062320](https://doi.org/10.1103/PhysRevA.69.062320).
- [64] A. Lupaşcu, E. F. C. Driessen, L. Roschier, C. J. P. M. Harmans, and J. E. Mooij. “High-Contrast Dispersive Readout of a Superconducting Flux Qubit Using a Nonlinear Resonator”. In: *Physical Review Letters* 96.12 (Mar. 2006), p. 127003. DOI: [10.1103/PhysRevLett.96.127003](https://doi.org/10.1103/PhysRevLett.96.127003).

- 
- [65] David Zueco, Georg M. Reuther, Sigmund Kohler, and Peter Hänggi. “Qubit-oscillator dynamics in the dispersive regime: Analytical theory beyond the rotating-wave approximation”. In: *Physical Review A - Atomic, Molecular, and Optical Physics* 80.3 (Sept. 2009), p. 033846. DOI: [10.1103/PhysRevA.80.033846](https://doi.org/10.1103/PhysRevA.80.033846).
- [66] Xiao-shen Li and Nian-yu Bei. “A generalized three-level Jaynes-Cummings model”. In: *Physics Letters A* 101.3 (Mar. 1984), pp. 169–174. DOI: [10.1016/0375-9601\(84\)90517-6](https://doi.org/10.1016/0375-9601(84)90517-6).
- [67] RH Dicke. “Coherence in spontaneous radiation processes”. In: *Physical Review* 24.1 (1954).
- [68] Michael Tavis and Frederick W. Cummings. “Exact Solution for an N-Molecule-Radiation-Field Hamiltonian”. In: *Physical Review* 170.2 (June 1968), pp. 379–384. DOI: [10.1103/PhysRev.170.379](https://doi.org/10.1103/PhysRev.170.379).
- [69] Michael Travis and Frederick W. Cummings. “Approximate solutions for an N-molecule-radiation-field Hamiltonian”. In: *Physical Review* 188.2 (Dec. 1969), pp. 692–695. DOI: [10.1103/PhysRev.188.692](https://doi.org/10.1103/PhysRev.188.692).
- [70] D. F. Walls and Gerald J. Milburn. *Quantum Optics*. Springer, 2008, p. 508. DOI: [10.1017/CBO9781107415324.004](https://doi.org/10.1017/CBO9781107415324.004).
- [71] M. David Pozar. *Microwave Engineering*. 4th. John Wiley & Sons, 2011, p. 720.
- [72] Alexandre Blais, Jay Gambetta, A Wallraff, et al. “Quantum-information processing with circuit quantum electrodynamics”. In: *Physical Review A - Atomic, Molecular, and Optical Physics* 75.3 (Mar. 2007), p. 032329. DOI: [10.1103/PhysRevA.75.032329](https://doi.org/10.1103/PhysRevA.75.032329).
- [73] Sharan Prakash Sharma and Lewis M. Attas. “Metastatic appendiceal carcinoma diagnosed in an asymptomatic patient with incidental thyroid mass on routine examination”. In: *Gastrointestinal Cancer Research* 6.2 (Mar. 2013), pp. 64–67. DOI: [10.1063/1.3693409](https://doi.org/10.1063/1.3693409).
- [74] M. Göppl, A. Fragner, M. Baur, et al. “Coplanar waveguide resonators for circuit quantum electrodynamics”. In: *Journal of Applied Physics* 104.11 (Dec. 2008), p. 113904. DOI: [10.1063/1.3010859](https://doi.org/10.1063/1.3010859).
- [75] Koki Watanabe, Keiji Yoshida, and Takeshi Aoki. “Kinetic inductance of superconducting coplanar waveguides”. In: *Japanese Journal of Applied Physics* 33.10R (Oct. 1994), pp. 570–572. DOI: [10.1143/JJAP.33.5708](https://doi.org/10.1143/JJAP.33.5708).
- [76] Christian Koller. *Towards the experimental realization of hybrid quantum systems*. 2012.
- [77] Michel Devoret, Steven Girvin, and Robert Schoelkopf. “Circuit-QED: How strong can the coupling between a Josephson junction atom and a transmission line resonator be?” In: *Annalen der Physik (Leipzig)* 16.10-11 (Oct. 2007), pp. 767–779. DOI: [10.1002/andp.200710261](https://doi.org/10.1002/andp.200710261).
- [78] R J Schoelkopf and S M Girvin. “Wiring up quantum systems”. In: *Nature* 451.7179 (2008), pp. 664–669. DOI: [10.1038/451664a](https://doi.org/10.1038/451664a).

- 
- [79] Matthew Gillick, Ian D. Robertson, and Jai S. Joshi. “Direct analytical solution for the electric field distribution at the conductor surfaces of coplanar waveguides”. In: *IEEE Transactions on Microwave Theory and Techniques* 41.1 (1993), pp. 129–135. DOI: [10.1109/22.210239](https://doi.org/10.1109/22.210239).
- [80] Stefan Putz. *Circuit cavity QED with macroscopic solid-State spin ensembles*. Wien, 2016.
- [81] I. Chiorescu, N. Groll, S. Bertaina, T. Mori, and S. Miyashita. “Magnetic strong coupling in a spin-photon system and transition to classical regime”. In: *Physical Review B - Condensed Matter and Materials Physics* 82.2 (July 2010), p. 024413. DOI: [10.1103/PhysRevB.82.024413](https://doi.org/10.1103/PhysRevB.82.024413).
- [82] D. I. Schuster, A. P. Sears, E. Ginossar, et al. “High-cooperativity coupling of electron-spin ensembles to superconducting cavities”. In: *Physical Review Letters* 105.14 (Sept. 2010), p. 140501. DOI: [10.1103/PhysRevLett.105.140501](https://doi.org/10.1103/PhysRevLett.105.140501).
- [83] P. Bushev, A. K. Feofanov, H. Rotzinger, et al. “Rare earth spin ensemble magnetically coupled to a superconducting resonator”. In: *Physical Review B* 84.6 (Aug. 2011), p. 060501. DOI: [10.1103/PhysRevB.84.060501](https://doi.org/10.1103/PhysRevB.84.060501).
- [84] Andreas Angerer, Thomas Astner, Daniel Wirtitsch, et al. “Collective strong coupling with homogeneous Rabi frequencies using a 3D lumped element microwave resonator”. In: *Applied Physics Letters* 109.3 (2016), p. 33508. DOI: [10.1063/1.4959095](https://doi.org/10.1063/1.4959095).
- [85] John F. Cochran and D. E. Mapother. “Superconducting Transition in Aluminum”. In: *Physical Review* 111.1 (July 1958), pp. 132–142. DOI: [10.1103/PhysRev.111.132](https://doi.org/10.1103/PhysRev.111.132).
- [86] Tobias Nöbauer, Kathrin Buczak, Andreas Angerer, et al. “Creation of ensembles of nitrogen-vacancy centers in diamond by neutron and electron irradiation”. In: (Sept. 2013).
- [87] Stefan Putz, D. O. Krimer, Robert Amsüss, et al. “Protecting a spin ensemble against decoherence in the strong-coupling regime of cavity QED”. In: *Nature Physics* 10.10 (Oct. 2014), pp. 720–724. DOI: [10.1038/nphys3050](https://doi.org/10.1038/nphys3050).
- [88] Andreas Angerer, Thomas Astner, Daniel Wirtitsch, et al. “Collective strong coupling with homogeneous Rabi frequencies using a 3D lumped element microwave resonator”. In: *Applied Physics Letters* 109.3 (2016). DOI: [10.1063/1.4959095](https://doi.org/10.1063/1.4959095).
- [89] E. Warburg. “Magnetische Untersuchungen”. In: *Annalen der Physik* 249.5 (Jan. 1881), pp. 141–164. DOI: [10.1002/andp.18812490510](https://doi.org/10.1002/andp.18812490510).
- [90] High Precision Devices. “Cryostat Model 103 Rainier”. In: (), pp. 1–5.
- [91] R. J. Thompson, G. Rempe, and H. J. Kimble. “Observation of normal-mode splitting for an atom in an optical cavity”. In: *Physical Review Letters* 68.8 (Feb. 1992), pp. 1132–1135. DOI: [10.1103/PhysRevLett.68.1132](https://doi.org/10.1103/PhysRevLett.68.1132).
- [92] K. Sandner, H. Ritsch, R. Amsüss, et al. “Strong magnetic coupling of an inhomogeneous nitrogen-vacancy ensemble to a cavity”. In: *Physical Review A - Atomic, Molecular, and Optical Physics* 85.5 (May 2012), p. 053806. DOI: [10.1103/PhysRevA.85.053806](https://doi.org/10.1103/PhysRevA.85.053806).

- 
- [93] Robert Amsüss. *Strong coupling of an  $NV^-$  spin ensemble to a superconducting resonator*.
- [94] S. Probst, H. Rotzinger, S. Wünsch, et al. “Anisotropic rare-earth spin ensemble strongly coupled to a superconducting resonator”. In: *Physical Review Letters* 110.15 (Apr. 2013), p. 157001. DOI: [10.1103/PhysRevLett.110.157001](https://doi.org/10.1103/PhysRevLett.110.157001).
- [95] Christoph W. Zollitsch, Kai Mueller, David P. Franke, et al. “High cooperativity coupling between a phosphorus donor spin ensemble and a superconducting microwave resonator”. In: *Applied Physics Letters* 107.14 (Oct. 2015), p. 142105. DOI: [10.1063/1.4932658](https://doi.org/10.1063/1.4932658).
- [96] Yutaka Tabuchi, Seiichiro Ishino, Atsushi Noguchi, et al. “Coherent coupling between a ferromagnetic magnon and a superconducting qubit”. In: *Science* 349.6246 (2015), pp. 405–408. DOI: [10.1126/science.aaa3693](https://doi.org/10.1126/science.aaa3693).
- [97] R. de L. Kronig. “On the mechanism of paramagnetic relaxation”. In: *Physica* 6.1 (Jan. 1939), pp. 33–43. DOI: [10.1016/S0031-8914\(39\)90282-X](https://doi.org/10.1016/S0031-8914(39)90282-X).
- [98] J. H. Van Vleck. “Paramagnetic Relaxation and the Equilibrium of Lattice Oscillators”. In: *Physical Review* 59.9 (May 1941), pp. 724–729. DOI: [10.1103/PhysRev.59.724](https://doi.org/10.1103/PhysRev.59.724).
- [99] C. J. Gorter. “Paramagnetic relaxation”. In: *Il Nuovo Cimento* 6.3 Supplement (June 1957), pp. 887–894. DOI: [10.1007/BF02834702](https://doi.org/10.1007/BF02834702).
- [100] R. J. Elliott. “Theory of the effect of spin-Orbit coupling on magnetic resonance in some semiconductors”. In: *Physical Review* 96.2 (Oct. 1954), pp. 266–279. DOI: [10.1103/PhysRev.96.266](https://doi.org/10.1103/PhysRev.96.266).
- [101] Y. Yafet. “g Factors and Spin-Lattice Relaxation of Conduction Electrons”. In: *Solid State Physics - Advances in Research and Applications* 14.C (Jan. 1963), pp. 1–98. DOI: [10.1016/S0081-1947\(08\)60259-3](https://doi.org/10.1016/S0081-1947(08)60259-3).
- [102] A. Jarmola, V. M. Acosta, K. Jensen, S. Chemerisov, and D. Budker. “Temperature- and magnetic-field-dependent longitudinal spin relaxation in nitrogen-vacancy ensembles in diamond”. In: *Physical Review Letters* 108.19 (May 2012), p. 197601. DOI: [10.1103/PhysRevLett.108.197601](https://doi.org/10.1103/PhysRevLett.108.197601).
- [103] A Jarmola, A Berzins, J. Smits, et al. “Longitudinal spin-relaxation in nitrogen-vacancy centers in electron irradiated diamond”. In: *Applied Physics Letters* 107.24 (2015), p. 242403. DOI: [10.1063/1.4937489](https://doi.org/10.1063/1.4937489).
- [104] Mariusz Mrózek, Daniel Rudnicki, Pauli Kehayias, et al. “Longitudinal spin relaxation in nitrogen-vacancy ensembles in diamond”. In: *EPJ Quantum Technology* 2.1 (Dec. 2015), p. 22. DOI: [10.1140/epjqt/s40507-015-0035-z](https://doi.org/10.1140/epjqt/s40507-015-0035-z).
- [105] M. B. Walker. “A T 5 spin-lattice relaxation rate for non-Kramers ions”. In: *Canadian Journal of Physics* 46.11 (June 1968), pp. 1347–1353. DOI: [10.1139/p68-455](https://doi.org/10.1139/p68-455).
- [106] R. Orbach. “Spin-lattice relaxation in rare-earth salts”. In: *Proceedings of the Royal Society of London. Series A. Mathematical and Physical Sciences* 264.1319 (Dec. 1961), pp. 458–484. DOI: [10.1098/rspa.1961.0211](https://doi.org/10.1098/rspa.1961.0211).

- 
- [107] D. A. Redman, S. Brown, R. H. Sands, and S. C. Rand. “Spin dynamics and electronic states of N-V centers in diamond by EPR and four-wave-mixing spectroscopy”. In: *Physical Review Letters* 67.24 (Dec. 1991), pp. 3420–3423. DOI: [10.1103/PhysRevLett.67.3420](https://doi.org/10.1103/PhysRevLett.67.3420).
- [108] D. A. Redman, S. Brown, R. H. Sands, and S. C. Rand. “Spin dynamics and electronic states of N-V centers in diamond by EPR and four-wave-mixing spectroscopy”. In: *Physical Review Letters* 67.24 (Dec. 1991), pp. 3420–3423. DOI: [10.1103/PhysRevLett.67.3420](https://doi.org/10.1103/PhysRevLett.67.3420).
- [109] Susumu Takahashi, Ronald Hanson, Johan Van Tol, Mark S. Sherwin, and David D. Awschalom. “Quenching spin decoherence in diamond through spin bath polarization”. In: *Physical Review Letters* 101.4 (July 2008), p. 047601. DOI: [10.1103/PhysRevLett.101.047601](https://doi.org/10.1103/PhysRevLett.101.047601).
- [110] J. Harrison, M. J. Sellars, and N. B. Manson. “Measurement of the optically induced spin polarisation of N-V centres in diamond”. In: *Diamond and Related Materials* 15.4-8 (Apr. 2006), pp. 586–588. DOI: [10.1016/j.diamond.2005.12.027](https://doi.org/10.1016/j.diamond.2005.12.027).
- [111] Johannes Gugler. *Ab initio calculation of the spin-lattice relaxation time T1 in the negatively charged nitrogen vacancy center in diamond*. Wien.
- [112] B. R. Johnson, M. D. Reed, A. A. Houck, et al. “Quantum non-demolition detection of single microwave photons in a circuit”. In: *Nature Physics* 6.9 (Sept. 2010), pp. 663–667. DOI: [10.1038/nphys1710](https://doi.org/10.1038/nphys1710).
- [113] E. M. Purcell, H. C. Torrey, and R. V. Pound. *Resonance absorption by nuclear magnetic moments in a solid*. Jan. 1946. DOI: [10.1103/PhysRev.69.37](https://doi.org/10.1103/PhysRev.69.37).
- [114] A. Bienfait, J. J. Pla, Y. Kubo, et al. “Controlling spin relaxation with a cavity”. In: *Nature* 531.7592 (Mar. 2016), pp. 74–77. DOI: [10.1038/nature16944](https://doi.org/10.1038/nature16944).
- [115] J. Gugler, T. Astner, A. Angerer, et al. “Ab initio calculation of the spin lattice relaxation time T1 for nitrogen-vacancy centers in diamond”. In: *Physical Review B* 98.21 (Dec. 2018), p. 214442. DOI: [10.1103/PhysRevB.98.214442](https://doi.org/10.1103/PhysRevB.98.214442).
- [116] G. Kresse and J. Furthmüller. “Efficient iterative schemes for ab initio total-energy calculations using a plane-wave basis set”. In: *Physical Review B - Condensed Matter and Materials Physics* 54.16 (Oct. 1996), pp. 11169–11186. DOI: [10.1103/PhysRevB.54.11169](https://doi.org/10.1103/PhysRevB.54.11169).
- [117] D. Joubert. “From ultrasoft pseudopotentials to the projector augmented-wave method”. In: *Physical Review B - Condensed Matter and Materials Physics* 59.3 (Jan. 1999), pp. 1758–1775. DOI: [10.1103/PhysRevB.59.1758](https://doi.org/10.1103/PhysRevB.59.1758).
- [118] Andreas Angerer, Stefan Putz, Dmitry O. Krimer, et al. “Ultralong relaxation times in bistable hybrid quantum systems”. In: *Science Advances* 3.12 (Dec. 2017), e1701626. DOI: [10.1126/sciadv.1701626](https://doi.org/10.1126/sciadv.1701626).
- [119] Andreas Angerer, Kirill Streltsov, Thomas Astner, et al. *Superradiant emission from colour centres in diamond*. Dec. 2018. DOI: [10.1038/s41567-018-0269-7](https://doi.org/10.1038/s41567-018-0269-7).
- [120] H. Bernien, B. Hensen, W. Pfaff, et al. “Heralded entanglement between solid-state qubits separated by three metres”. In: *Nature* 497.7447 (Apr. 2013), pp. 86–90. DOI: [10.1038/nature12016](https://doi.org/10.1038/nature12016).

- 
- [121] B. Hensen, H. Bernien, A. E. Dréau, et al. “Loophole-free Bell inequality violation using electron spins separated by 1.3 kilometres”. In: *Nature* 526.7575 (Oct. 2015), pp. 682–686. DOI: [10.1038/nature15759](https://doi.org/10.1038/nature15759).
- [122] F. Dolde, I. Jakobi, B. Naydenov, et al. “Room-temperature entanglement between single defect spins in diamond”. In: *Nature Physics* 9.3 (Mar. 2013), pp. 139–143. DOI: [10.1038/nphys2545](https://doi.org/10.1038/nphys2545).
- [123] I. Diniz, S. Portolan, R. Ferreira, et al. “Strongly coupling a cavity to inhomogeneous ensembles of emitters: Potential for long-lived solid-state quantum memories”. In: *Physical Review A - Atomic, Molecular, and Optical Physics* 84.6 (Dec. 2011), p. 063810. DOI: [10.1103/PhysRevA.84.063810](https://doi.org/10.1103/PhysRevA.84.063810).
- [124] Z. Kurucz, J. H. Wesenberg, and K. Mølmer. “Spectroscopic properties of inhomogeneously broadened spin ensembles in a cavity”. In: *Physical Review A - Atomic, Molecular, and Optical Physics* 83.5 (May 2011), p. 053852. DOI: [10.1103/PhysRevA.83.053852](https://doi.org/10.1103/PhysRevA.83.053852).
- [125] C W Gardiner and P Zoller. “Quantum Noise: A Handbook of Markovian and Non-Markovian Quantum Stochastic ... - Crispin Gardiner, Peter Zoller - Google Books”. In: (2004), p. 449.
- [126] M Brune, P Nussenzveig, F Schmidt-Kaler, et al. “From Lamb shift to light shifts: Vacuum and subphoton cavity fields measured by atomic phase sensitive detection”. In: *Physical Review Letters* 72.21 (1994), pp. 3339–3342. DOI: [10.1103/PhysRevLett.72.3339](https://doi.org/10.1103/PhysRevLett.72.3339).
- [127] A. Fregner, M. Goppl, J. M. Fink, et al. “Resolving Vacuum Fluctuations in an Electrical Circuit by Measuring the Lamb Shift”. In: *Science* 322.5906 (Nov. 2008), pp. 1357–1360. DOI: [10.1126/science.1164482](https://doi.org/10.1126/science.1164482).
- [128] Damien Garcia. “Robust smoothing of gridded data in one and higher dimensions with missing values”. In: *Computational Statistics & Data Analysis* 54.4 (Apr. 2010), pp. 1167–1178. DOI: [10.1016/j.csda.2009.09.020](https://doi.org/10.1016/j.csda.2009.09.020).
- [129] Yimin Liu, Jiabin You, and Qizhe Hou. “Entanglement dynamics of Nitrogen-vacancy centers spin ensembles coupled to a superconducting resonator”. In: *Scientific Reports* 6.1 (Apr. 2016), p. 21775. DOI: [10.1038/srep21775](https://doi.org/10.1038/srep21775).
- [130] Yusef Maleki and Aleksei M. Zheltikov. “Witnessing quantum entanglement in ensembles of nitrogen–vacancy centers coupled to a superconducting resonator”. In: *Optics Express* 26.14 (July 2018), p. 17849. DOI: [10.1364/oe.26.017849](https://doi.org/10.1364/oe.26.017849).
- [131] Yusuke Hama, William J Munro, and Kae Nemoto. “Relaxation to Negative Temperatures in Double Domain Systems”. In: *Physical Review Letters* 120.6 (2018). DOI: [10.1103/PhysRevLett.120.060403](https://doi.org/10.1103/PhysRevLett.120.060403).
- [132] Yusuke Hama, Emi Yukawa, William J Munro, and Kae Nemoto. “Negative-temperature-state relaxation and reservoir-assisted quantum entanglement in double-spin-domain systems”. In: *Physical Review A* 98.5 (2018), p. 52133. DOI: [10.1103/PhysRevA.98.052133](https://doi.org/10.1103/PhysRevA.98.052133).

## References

---

- [133] Jason R. Ball, Yu Yamashiro, Hitoshi Sumiya, et al. “Loop-gap microwave resonator for hybrid quantum systems”. In: *Applied Physics Letters* 112.20 (May 2018), p. 204102. DOI: [10.1063/1.5025744](https://doi.org/10.1063/1.5025744).

## Acknowledgements

So it seems I reached the last page of this thesis. A project like doing a PhD involves more than a single person - without collaborations and help of others this would have been impossible. That is why this page is dedicated to the people who carried me along this journey.

Johannes Majer, you gave me an environment of total freedom and allowed me to pursue my ideas and ways of doing things while being supportive and helpful in all matters. I thank you for all the good advices you gave and the knowledge I acquired from you over the years.

Jörg Schmiedmayer, in this lively group environment you created here at the Atom-institut you give us so many inspirations for the work we are doing. Your curiosity and ideas are spreading throughout the group and motivate us all.

I further thank the whole cryolab team: Stefan Putz for endless constructive critiques and sharp discussions. Christian Koller, Robert Amsüß, and Stefan Nevlacsil: You are the people I learned a lot from and you significantly contributed to the research in here. Andreas Angerer, I thank you for sharing the last couple years in the lab. We had many stimulating discussions that lasted beyond physics. Without your help and support in all matters - this would have not been possible. Wenzel, you will produce so many new thrilling results in the future, I am looking forward to it. I also thank the students for helping me along this journey: Sebastian W. and P., Maja, Dominik, Marie-Therese, Ricarda and Noomi.

One project relied on the wonderful collaboration we had with the institute for computational material science. I thank Peter Mohn and Johannes Gugler for their fruitful discussions and all the work they put in our joint project. Additionally, I want to thank Michael Trupke for all his advices and help throughout this work.

The Chef's table cooking group, thank you Mira and Filippo, for sharing many great lunch dishes. I enjoy cooking and eating with you so much, you are such amazing people. Mira, thank you for sitting outside at the stairs, enjoying coffee together with some nice extensive 'sudern' about the overall situation. Filippo, thank you for bringing so much colour and joy that makes everyone happy.

The people of the 'Alleestüberl': Bernhard, Federica (life is ridicoloso), Filippo and



## References

---

Pradyumna. Thank you for sharing the office the last years and all the extraordinary discussions we had here. Big thank you to the atomchip crowd: Marine for your comprehension, Andrew for barbecue enthusiasm, Joao for being a great portuguese :P, Amin for helping out whenever you can, Camille for good yard discussions, Thomas S. for sharp comments, Frederic for sharing tea, Fritz D. for reading my thesis, Tian Tian, Qi, Chen and RuGway for bringing in your wisdom and culture! And yes, there are too many of you I owe so much gratitude, I thank you for all the help throughout the years.

Isi, Sarah and Bernji, we shared so many good moments over the last years. Without you I could not have finished this huge project. You helped me going through all this, you were there and gave me strength and support, I thank you from the bottom of my heart for more than a friendship.

Florian, thank you for your friendship that already lasts since secondary school! Anna, for your great friendship and just being who you are.

Christian, Roland, and Kristl, for listening to my sorrows and complaints, for sharing evenings with refreshing drinks, for brewing beer together, for hanging out and for your friendship. It feels good to have such people around. Waldi and Hila for the endless geeky discussions about physics and math related stuff. Your optimism and enthusiasm is very motivating and catching.

My family, for being there and supporting me along this journey. My nephews, watching how you discover this world is one of the most satisfying things for me.

## Curriculum Vitae

Name: Thomas Astner

Place of birth: Kufstein

Citizenship: Austria

Email: thomas.astner@gmail.com

- 2003-2008 / School for higher technical education (HTL) - Jenbach, Austria
- 2008-2009 / Civil services
- 2009-2012 / BSc studies of Technical Physics, TU Wien, Austria
- 2012-2015 / MSc studies of Technical Physics, TU Wien, Austria
- 2015-2019 / PhD studies of Technical Physics, TU Wien, Austria